Seismic Cross-Hole Method and Assessment of the Small-Strain Stiffness, G_{max}.

Marcus Hagen

Trondheim, July 2019

Master Thesis: TBA4900

Main supervisor: Steinar Nordal

Department of Civil and Transport Engineering

Norwegian University of Science and Technology (NTNU)

NTNU – Trondheim
Norwegian University of
Science and Technology

Preface

This study was performed as a Master's Thesis in the specialization course TBA4900 in Geotechnics. The study is a part of the MSc in civil and environmental engineering with specialisation in geotechnics. The study is written under the division for geotechnics at the Norwegian University of Science and Technology (NTNU).

This thesis is the continuation of the project thesis on cross-hole testing at the NGTS test site on Flotten, Trondheim. This study is performed and written during the spring of 2019, with a duration of 20 weeks.

The main supervisor for the thesis was Steinar Nordal.

The idea for this master's thesis was proposed by supervisor Steinar Nordal, with input from Arnfinn Emdal.

Trondheim, 2019-15-07

Marcus Hagen

Acknowledgment

I would like to thank the following persons for their help and support during this thesis:

Steinar Nordal, for being helpful in finding this topic, and giving valuable insight into what needs to be done.

Jean-Sebastien L'Heureux, for providing relevant literature

Per Asbjørn Østensen for setting up the software for cross-hole testing and for taking the time to help and guide me during field testing.

Karl Ivar Volden Kvisvik and Espen Andersen for conducting the field tests.

A special thank you to Mathilde Hanssen for showing great support and patience, always keeping me happy and motivated.

M.H.

Abstract

The small strain shear modulus, G_{max} is is an important engineering property for many geotechnical and geodynamic problems, and is also used for advanced finite element modelling. The G_{max} is characteristic property of the soil, and can be used for identification of soil. The small strain modulus is affected by many different parameters, with the most important being strain amplitude, confining stress, void ratio and interparticle bonding. The G_{max} can be determined from laboratory testing, or from in situ field tests. This thesis is mainly focused seismic cross-hole field testing, as well as seismic dilatometer testing. values from multichannel analysis of surface waves are also mentioned.

Cross-hole testing was conducted on the NGTS quick clay test site on Flotten, in the outskirts of Trondheim, Norway. Cross-hole surveying was done at 5 meters depth using vertical impact on the source, as well as four different horizontal impact directions. The cross-hole test yielded values in the range 128 m/s $\leq v_s \leq$ 156 m/s. Results from seismic dilatometer testing (SDMT) at the same depth gave an average value of v_s around 129 m/s. The cross-hole tests with signals produced by vertical impact and horizontal impact directions parallel to receiver configuration gave values that agreed very well to the findings from SDMT testing. However, large scatter in the SDMT results from this depth, give high uncertainty in the accuracy of the test data. Results from multichannel analysis of surface waves give significantly higher shear wave velocity at 5 meters depth.

Both the cross-hole setup and shear wave velocity determination process has many sources of error attached to it. Most importantly, no protective casing around the source rod, result in disturbed responses at the receiver. receivers embedded inside plastic tubes, can lead to attenuation of seismic waves, before the signals are recorded. A setup with possibility to separate the receiver tip from the rest of the pipe is adviced for future testing.

$G_{max]}$ values for the Flotten clay at 5 meters depth are in the order of 31-40 MPa based on cross-hole results, 29 MPa based on SDMT, and about 50 MPa based on the MASW method. All of which correspond to typical characteristic values for Trondheim clays.

Contents

Chapter 1

Introduction

This chapter serves as a description of the topic to be investigated. In the following, the background for the thesis and task description will be given followed by information regarding the conducted study.

1.1 Background

Due to the inherent variability in characteristics of soil masses, many methods and analyses has been developed to measure and produce information about the subsurface. Anisotropy, nonhomogeneity, compaction and other effects contribute to uncertainty in deciding the characteristics of geological material. Due to this, soil can not be idealized as one bulk of mass with constant attributes, but instead the soil can gradually change behaviour in different directions.

As requirements for safety and precision for estimates increase, it becomes more important to better evaluate what the subsurface is comprised of. Methods using dynamic loading has long shown great potential for finding valuable information about soil. The governing properties for soil subjected to dynamic loading are called *Dynamic soil properties*, and give key information about the stress-strain behaviour.

Characterisation of the stress-strain behaviour is an integral part of many geotechnical design applications, including earthquake hazard analyses, site response analyse and characterisation of the site material. Problems related to cyclic loads such as earthquakes are dominated by effects of wave propagation where the strains induced are low. The seismic waves propagating through the soil medium is damped as a function of the soils stiffness. The small-strain shear modulus, G_{max} is related to shear strains in the order of $\gamma \leq 10^{-3}$, and are an appropriate measure for soil behaviour subjected to seismic loads.

The G_{max} can be found from laboratory tests and measured using in situ methods. Laboratory testing requires high quality, undisturbed samples, which can be a great challenge, particularly for soft and sensitive clays. Testing in laboratory only yields results from the sampled section, and may not be representative for the whole site (L'Heureux, 2017). In situ methods require no careful handling and transport of material and allows for average estimates across larger distances. The *Cross-hole seismic method* is an increasingly important method for determining G_{max}, and are widely considered one of the easiest and most accurate methods of determining the small-strain shear modulus (Hall Bodare, 2000).

The topic of cross-hole seismic is of interest, in regards to the NGTS test site at Flotten, in the outskirts of Trondheim. The work of this thesis aims to quantify the small-strain stiffness using seismic cross-hole testing at the NGTS test site at Flotten, Norway. The findings will be evaluated against already existing data on the small strain stiffness from other field methods.

1.2 Task Description

The topic of this Master thesis was worked out as an agreement between Steinar Nordal, Arnfinn Emdal and myself, and this topic did not have a predetermined task description. It was suggested to conduct new cross-hole tests for determination of the small strain shear stiffness G_{max} at the NGTS test site on Flotten, Norway.

The task requires a literature study, to find out what parameters affect G_{max}, and how they affect it. The literature study will also cover methods of acquiring the G_{max} of soils.

1.2.1 Objectives

The main objectives of this thesis are:

1. Presentation of theory regarding the determination of G_{max}, and parameters affecting it.
2. Evaluation of the cross-hole seismic method.
3. Compare the results from cross-hole testing to the results from previous investigations on site.

1.3 Literature Survey

The main sources of information in this study is Steven L. Kramer's *Geotechnical Earthquake Engineering* (1996) and Studies published in connection with the NGTS test sites. NTNU's library search engine Oria, and Google Scholar are the primary search engines used to find academic studies to back this study. By using reference lists of relevant articles, more essential information was gathered. Throughout, the sources reliability have been evaluated by their publishers and peer-reviews.

1.4 Approach

Before starting this thesis, a project report was written in autumn 2018. The project report served as a preliminary background study on seismic waves, small strain stiffness and cross-hole testing in general. The first phase of this thesis is a continuation of the previous literature study, supplementing existing data, gathered knowledge and acquiring new information.

Due to missing equipment the initially planned cross-hole testing was postponed, which lead to important analyses having to be conducted in a late stage of this thesis. During field testing, some of the initial results proved difficult to evaluate, raising questions to whether there was problems with setup or equipment.

Interpretation of the results turned out to be challenging, having to evaluate wave arrival times in response plots with heavy noise. After analysing the cross-hole receiver response, the results were compared to previously conducted field tests on G_{max}.

1.5 Structure of the Report

The thesis consists of nine chapters, where the remaining chapters are:

- Chapter 2 presents necessary theory needed to back up the later chapters, including cyclic loads, stress-strain behaviour of cyclically loaded soils, properties of seismic waves, and how waves are attenuated as they propagate through a medium.
- Chapter 3 presents the small strain shear stiffness G_{max}, and the parameters that affect it. The chapter will also cover methods for determination of G_{max}.
- Chapter 4 give a brief overview of digital signal analysis, and how it is used to record signals and convert the response from analog to digital data.
- Chapter 5 presents the NGTS clay test site on Flotten, describing its location and material properties.
- Chapter 6 describes the cross-hole testing that was conducted on site, giving setup and procedure for creation of dynamic load, and recording of seismic response.
- Chapter 7 presents the v_s and G_{max} results from cross-hole testing, as well as values determined from other methods on site.
- Chapter 8 gives a discussion of the cross-hole tests. Challenges and sources of error are covered. A discussion on its viability compared to the seismic dilatometer test are given.
- Chapter 9 gives a conclusion on the assessments done in this thesis. Proposals for further work is presented.

Chapter 2

Theory

This chapter will present the theory behind cyclically loaded soils and seismic wave propagation through soils. The theory will serve as the basis for understanding soil dynamics with a focus on parameters influencing stress-strain relationship and wave propagation velocities.

2.1 Stress-Strain Behaviour of Cyclically Loaded Soils

An element subjected to static loading conditions is under a constant load which does not change over time. On the other hand dynamic loads, such as wave propagation effects have cyclically varying load distributions. While static loads tend to be better defined, the dynamic loads generally have a higher degree of uncertainty associated (Reynolds, 2011). The mechanical properties and response of soils are complex under dynamic loading. The behaviour of soils subjected to cyclic loading is governed by the dynamic soil properties (Kramer, 1996). This section will address the soil response under cyclic loading and the how the dynamic soil properties affect the induced response

2.1.1 Stress-Strain Behaviour

Assessment of stress-strain behaviour is an important aspect of many geotechnical design applications, such as Earthquake analysis, settlement analysis, site characterisation and soil-structure interaction (L'Heureux & Long, 2017).

If an external force F is applied over a surface area A, forces inside the soil body are established in response to the external force. The ratio of force to area is known as stress (σ) (Reynolds, 2011), given from equation 2.1.

$$\sigma = \frac{F}{A} \tag{2.1}$$

A body subjected to stress undergoes strain, which is expressed as the ratio of change in length (δL) or volume (δV) to the original length (L_0) or volume (V_0) (Reynolds, 2011) . The equations for strain and volumetric strain are given respectively from equation 2.2 and 2.3.

$$\epsilon = \frac{\delta L}{L_0} \tag{2.2}$$

$$\epsilon_V = \frac{\delta V}{V_0} \tag{2.3}$$

From theory of linear elasticity, Hooke's law states that stress and strain are linearly dependent. The element behaves elastically before the yield point with all deformation being reversible. After yielding, plastic and non reversible deformation occurs. However problems dominated by wave propagation effects only produce small strains, and are well within the elastic domain of natural materials such as soil (Reynolds, 2011).

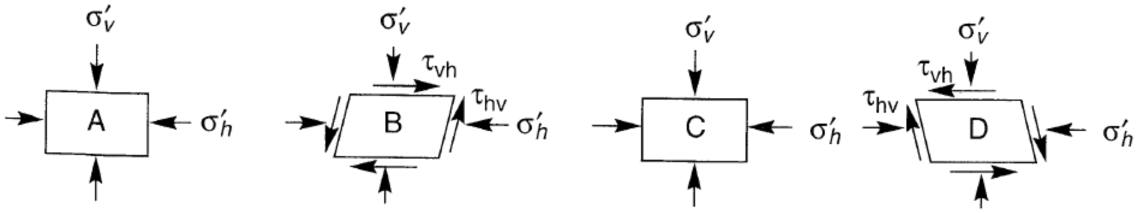

Figure 2.1: Shear strain γ expressing the distortion of an element with height h and width B (Kramer, 1996)

To illustrate how soils behave under dynamic loading consider an element of soil beneath the surface subjected to vertically propagating S-waves, given in figure 2.8 (Kramer, 1996). Stage A defines the initial at rest condition, with no load applied to the element. Here the element is in equilibrium and is subjected to a vertical and horizontal stress, defined by the coefficient of at rest pressure, K_0, given by equation 2.4.

$$K_0 = \frac{\sigma'_3}{\sigma'_1} \tag{2.4}$$

Most realistic loading situations cause a change in both vertical and horizontal stresses with resulting shear stresses on the vertical and horizontal planes. In stage B, a vertically propagating S-wave travels through the element and shear stresses, τ are produced on the horizontal faces of the soil element. This results in shear stress on the vertical sides to counteract rotation and to maintain equilibrium. as a result of the S-waves inducing shear stresses the element will have distorted and undergone a shear strain, given by equation 2.5, and illustrated by figure 2.2 (Pecker, 2007).

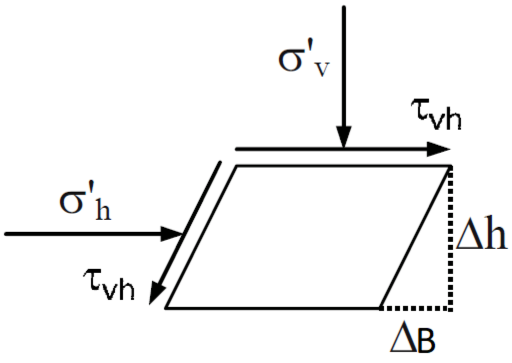

Figure 2.2: Shear strain γ expressing the distortion of an element with height h and width B (Pecker, 2007)

$$\gamma = \frac{\Delta B}{\Delta h} \tag{2.5}$$

Since the shear stresses increase while the horizontal and vertical stresses are kept constant, the center of the Mohr circle is also kept constant. when only the shear stresses increase, the radius of the Mohr circle increases and the stress path moves vertically. This indicates that the principal stress axes are rotated from their original positions. Since the applied dynamic load is cyclic the horizontal shear stresses are cyclic as well, reverting its direction back through the τ_{hv}=τ_{vh}=0. The reverting of the directions back to initial state and zero shear stresses is illustrated by stage C. At stage D, the S-wave produces shear stresses and principal stress axis rotation in the opposite direction as stage B. Figure 2.3 show how the Mohr circle expand as dynamic load is applied, and the resulting change in major principle stress axis direction. Research has shown that even if stress points do not move, the rotation of the principal stress axis alone can cause shear and volumetric strain. This means that a portion of the strain caused by propagating shear waves are due to principal stress rotation (Kramer, 1996).

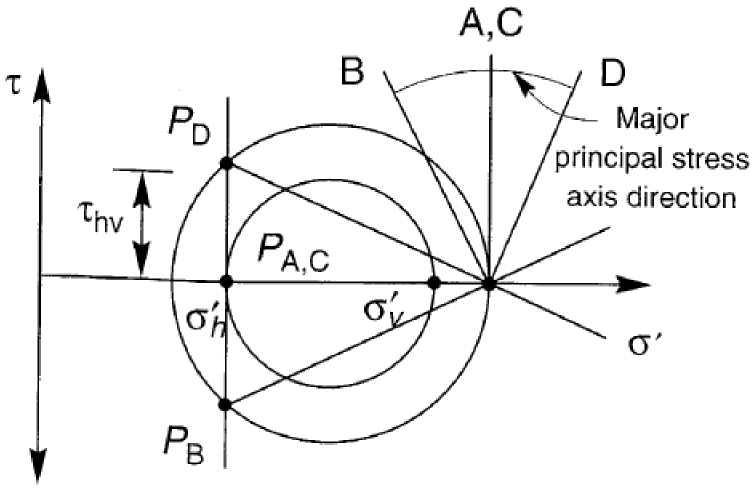

Figure 2.3: Mohr circles for all stages, location of poles and direction of the principle stress axis

2.1.2 Attenuation of Wave Energy

When considering wave propagation in homogeneous linear elastic materials, stress waves travel with constant amplitude with no loss of flux. Linear elasticity is an idealisation, and real materials does not behave linearly elastic. For natural materials such as soil, the wave amplitude will attenuate with distance from the source. Attenuation of stress waves are due to two factors; Material damping and radiation damping (Kramer, 1996).

Material Damping

As soil is subjected to dynamic load cycles of constant amplitude, energy dissipates as a result of material damping, or hysteretic damping. By plotting the shear stress-shear strain curves from laboratory testing on soil samples with constant amplitude, a hysteresis loop is obtained. Such a hysteresis loop is given in figure 2.4. Cyclic loading under constant amplitude creates a loop where all loading and unloading curves follow the shape of the first loading curve (Backbone curve). The inclination and surface are dependent on the strain amplitude. For larger shear strain, γ the hysteresis loop will be wide, and flatter on the horizontal γ axis (Pecker, 2007).

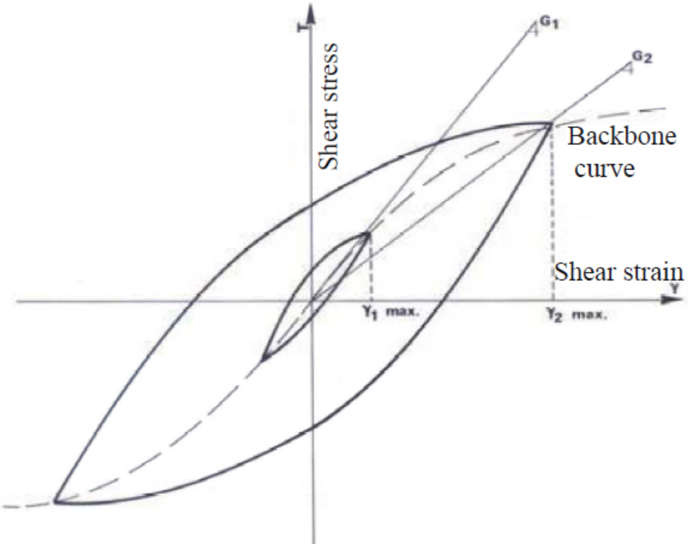

Figure 2.4: τ-γ curve giving a hysteresis loop for constant amplitude cyclic loading (Pecker, 2007)

However, in real materials the waves are damped and part of the elastic energy of the travelling waves are converted to heat. In soils the elastic energy is dissipated as a result of of grain slippage, and loss of grain to grain contact. A reduction in specific energy causes the amplitude of the stress wave to decrease with distance. More energy is dissipated as the shear strain amplitude is increased, which results in an increased damping ratio ζ (Kramer, 1996). When the loading cycles no longer have constant amplitude, the stress-strain behaviour changes. An example of a sample cyclically loaded under cycles with non-constant amplitude is given in figure 2.5 (Pecker, 2007).

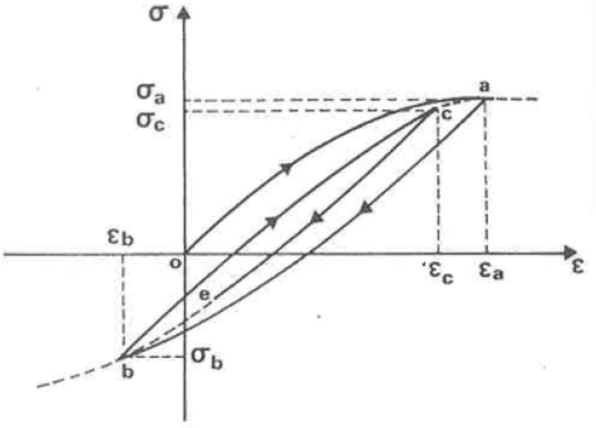

Figure 2.5: τ-γ curve giving a hysteresis loop for non-constant amplitude cyclic loading (Pecker, 2007)

From such an arbitrary cyclic loading given in figure 2.5 the stress-strain curve will follow the backbone curve from point a to point b, but due to damping effects the unloading curve from point b to point c will no longer be symmetric to the backbone curve. The stress-strain behaviour depicted in figure 2.5 is accompanied by volumetric strains which further proves that the behaviour is no longer elastic. It is worth noting that dry materials will induce hardening behaviour, which will cause different hysteresis loops even for symmetric constant amplitude cycles (Pecker, 2007).

Kramer (1996) modelled the dissipation of elastic energy using the behaviour of Kelvin-Voigt solids. A Kelvin-Voigt solid is a material whose resistance to shearing deformation is a sum of an elastic part and a viscous part. The relationship between shear stress and shear strain for a Kelvin-Voigt solid can be formulated by equation 2.6.

$$\tau = G\gamma + \eta \frac{\partial \gamma}{\partial t} \tag{2.6}$$

Where τ and γ is the shear stress and shear strain, respectively. The η is material viscosity and G is the shear modulus. The first part of equation 2.6 therefore describes the elastic behaviour being proportional to strain, while the second part second part is the viscous part, being proportional to rate of strain with time. The equation for harmonic shear strain, given by equation 2.7 can be inserted into equation 2.6 yielding a new term for the shear stress exerted to harmonic shear strain, given by equation 2.8, where ω is the angular frequency.

$$\gamma = \gamma_0 \sin \omega t \tag{2.7}$$

$$\tau = G\gamma_0 \sin \omega t + \omega \eta \gamma_0 \cos \omega t \tag{2.8}$$

Equation2.8 prove that for shear strain of constant amplitude, gives an elliptical stress-strain loop, as can be seen from figure 2.6. The attenuation of elastic energy from one cycle is defined from the area of the ellipse, which means the dissipated energy from such a system is proportional to the frequency of loading. As mentioned above, real soils dissipate energy by hysteretic damping, with reduction in shear strain amplitude. Therefore real soils are insensitive to the frequency. The Kelvin-Voigt solid is therefore useful for giving a relation to maximum strain energy dissipating during one cycle, i.e the backbone curve in the hysteresis loop from figure 2.5. After integrating over the area of the ellipse the maximum strain energy attenuated from one cycle can be expressed by equation 2.9. The expression for peak energy, W is expressed by equation 2.10.

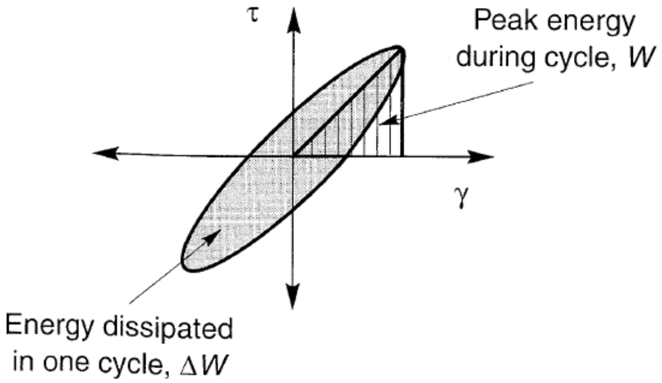

Figure 2.6: τ-γ curve giving an elliptical stress strain curve

$$\Delta W = \int_{t_o}^{t_0+\frac{2\pi}{\omega}} \tau \frac{\partial \gamma}{\partial t} dt = \pi \eta \omega \gamma_0^2 \tag{2.9}$$

$$W = \frac{1}{2} G \gamma_0^2 \tag{2.10}$$

To quantify the attenuation of stress waves due to material damping, the damping ratio is introduced. The damping ratio is a measure of how much energy attenuates from an oscillatory system (Benz, 2007). For the frequency dependent Kelvin-Voigt system from figure 2.6, the damping ratio can be expressed by equation 2.11

$$\zeta = \frac{\Delta W}{4\pi W} \tag{2.11}$$

By inserting for equations 2.9 and 2.10, the relation in equation 2.12 is achieved.

$$\zeta = \frac{1}{4\pi} \frac{\pi \eta \omega \gamma_0^2}{\frac{1}{2} G \gamma_0^2} = \frac{\eta \omega}{2G} \tag{2.12}$$

By rearranging equation 2.12, with focus on viscosity, η one achieve what is called the equivalent viscosity, given by equation 2.13. The equivalent viscosity is inversely proportional to the frequency, ω. This formulation produces an expression for the damping ratio which is independent of frequency, and therefore more suited to describe material damping in real soils (Kramer, 1996).

$$\eta = \frac{2G\zeta}{\omega} \tag{2.13}$$

2.2 Seismic Waves

Seismic waves can be considered as small loads of elastic strain energy, that travel from any seismic source through a medium at speeds determined mainly by stiffness and density of the penetrated body. The principle of seismic exploration is for a signal to be generated at a known time, and for the resulting seismic waves to travel through the subsurface and response of direct, reflected or refracted signal is measured. The elapsed time between source signal being triggered and arrival of the different waves is used to characterise the attributes and behaviour of the penetrated medium (Reynolds, 2011). This section will give an introduction to the different seismic waves and seismic wave propagation.

2.2.1 Types of Seismic Waves

There are two main categories of seismic waves, body waves which pass through the bulk of a medium, and surface waves which are confined to interfaces between media of different properties. A third category exist called guided waves that are exclusive to very thin bands in the confined in between two layers with higher seismic velocities than the band (Reynolds, 2011). Guided waves will not be covered any further in this paper. Most relevant for soils are the body waves, particularly compressional waves (P-waves) and shear waves (S-waves).

P-waves

The first type of body wave is the P-wave, often called compressional, primary or longitudinal waves. The P-wave is characterised by successive compressional and dilational strain in the affected soil body. This is caused by material particles oscillating about fixed points in the same direction as the direction of wave propagation. A P-wave therefore induce volumetric deformations, and no shearing deformations (Reynolds, 2011). Elastic deformation and particle movement is given by figure 2.7

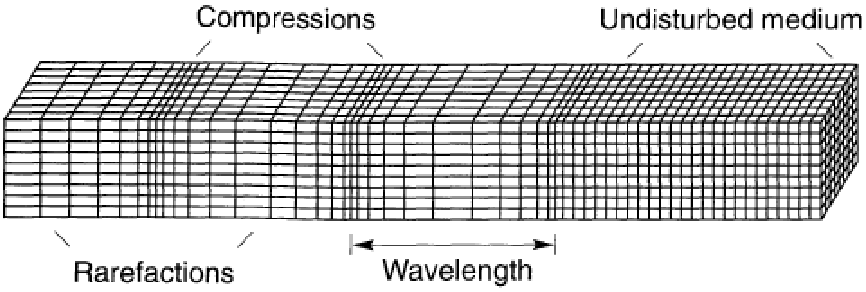

Figure 2.7: A P-wave cause successive compression and rarefaction parallel to the direction of wave propagation (KRAMER, 1996)

The travelling speed of seismic waves are dependant on the stiffness of the material which it is travelling through. For geological material such as soil P-waves will travel faster than other wave types, due to rock having higher stiffness in compression than in dilation (Kramer,1996). This generally means that P-waves are the first wave type to reach a given receiver after a seismic signal is initiated.

By differentiating the three-dimensional differential equations of motion for an isotropic linear elastic medium, an equation for P-wave motion is gained. The differential equation for a P-wave is given by equation 2.14

$$\frac{\partial^2 \epsilon_v}{\partial t^2} = \frac{\lambda + 2\mu}{\rho} \nabla^2 \epsilon_v = v_p^2 \nabla^2 \epsilon_v \tag{2.14}$$

Where ϵ_v is volumetric strain, t is time, ρ is density and λ and μ are Lamé constants.

equation 2.14 is a function of the volumetric strain, which indicates a dilational wave with no shearing deformation or rotation. The equation can therefore be used to describe how P-waves propagate through an affected body. it follows from the equation that a S-wave propagating through a solid medium will travel at a velocity given by equation 2.15 (Kramer, 1996).

$$v_p = \sqrt{\frac{\lambda + 2\mu}{\rho}} \tag{2.15}$$

By inserting for the lamé constants in equation 2.15, an expression for P-wave velocity as a function of shear modulus G and Poisson's ratio ν is achieved. Equation 2.16 is often a more useful expression for P-wave velocity.

$$v_p = \sqrt{\frac{G(2-2\nu)}{\rho}} \tag{2.16}$$

S-waves

The second type of body waves are the S-wave, often also referred to as shear, secondary or transverse waves. The S-waves induce shear strain on the affected medium and cause particle motion at right angles to the direction of wave propagation (Reynolds, 2011). S-waves only induce shear deformations and no volumetric deformations (Kramer, 1996) . The direction of particle movement can be used to separate shear waves in to two components, Vertical plane (SV) and horizontal plane (SH) movement. Hence, shear waves have the capability of polarization, which allows for testing of the material in two directions. This yields shear wave signals that are 180 degrees out of phase.

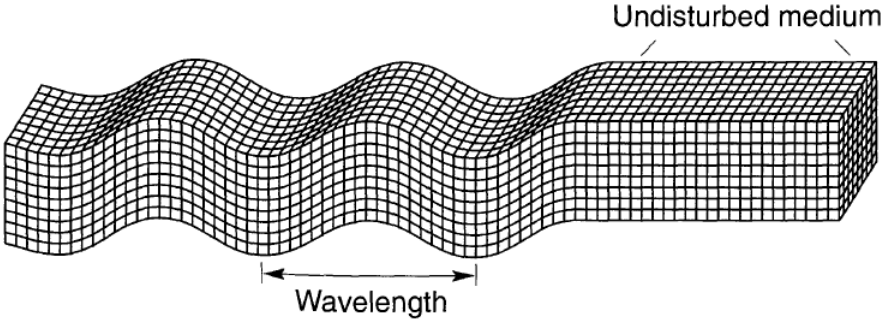

Figure 2.8: A S-wave generate shearing deformation with particle movement perpendicular to the direction of wave propagation (Kramer, 1996).

By differentiating the the three-dimensional differential equations of motion for an isotropic linear elastic medium to to eliminate the volumetric strain, one achieve the differential equation for a distortional wave. such a wave describe a rotation about the direction of wave propagation is equivalent to how S-waves behave (Kramer, 1996). The differential equation of the S-wave is given by equation 2.17.

$$\frac{\partial^2\Omega_x}{\partial t^2} = \frac{\mu}{\rho}\nabla^2\Omega_x = v_s^2\nabla^2\omega_x \tag{2.17}$$

Where Ω_x is rotations around the x-axis, t is time, ρ is density and μ is one of the Lamé constants. From Equation 2.17 one get an expression for the velocity of S-waves. Since the Lamé constant μ is equal to the shear modulus, one get S-wave velocity as a function of shear modulus G, as seen in equation 2.18.

$$v_s = \sqrt{\frac{\mu}{\rho}} = \sqrt{\frac{G}{\rho}} \tag{2.18}$$

The body waves are the only waves that can propagate through an unbounded elastic solid. The relationship between P-waves and S-waves are given from equation 2.19.

$$\frac{v_p}{v_s} = \sqrt{\frac{2(1-\nu)}{1-2\nu}} \tag{2.19}$$

The ratio shows that v_p always will be greater than v_s, with the magnitude being a factor of the Poisson's ratio, ν. for unconsolidated and undrained materials the P-wave velocity will be much greater than that of the S-wave, as the ν approaches 0.5. This velocity relationship is illustrated in figure 2.9 (Kramer, 1996).

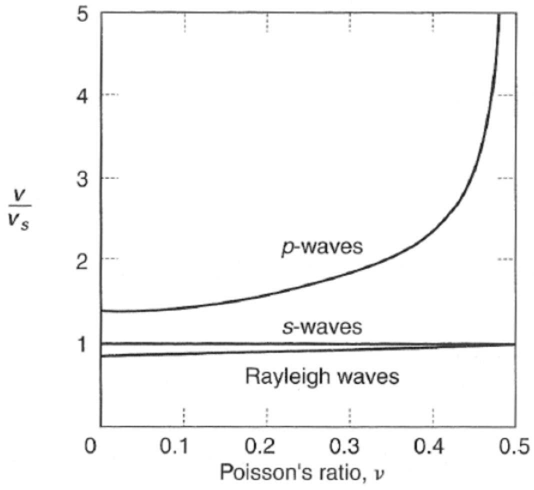

Figure 2.9: For increasing Poisson's ratio, the P-wave velocity will increase with respect to the S-wave velocity (Kramer, 1996).

Surface Waves

Surface waves are waves that do not penetrate deep into the ground. While Body waves are non-dispersive, the surface waves have wave dispersion, which means that the waveform changes as the the wave propagates. This indicate that for a non-uniform material, the velocity of propagation is dependent on the wavelength such as in equation 2.20 (Long et.al, 2008). There are two types of surface waves, known as Rayleigh and Love waves. The Rayleigh waves travel along the free surface of the ground medium, with amplitudes decreasing with depth. Rayleigh waves cause particle motion in an elliptical fashion. Particle motion associated with Rayleigh waves consist of both horizontal and vertical components, when close to the surface form a retrograde ellipse. With increased depth the particle motion changes to pure vertical, and finally to a prograde ellipse (Ismail et.al, 2001). This elliptical particle motion can often manifest itself as low-frequency ground roll waves. Ground roll can mask seismic reflections in different surveys, and are often considered noise. The deformations associated with Rayleigh waves are given in figure 2.10 (Reynolds, 2011).

$$\lambda = \frac{v_R}{f} \tag{2.20}$$

Where λ is the wavelength, f is the frequency and v_R is the velocity of the Rayleigh wave.

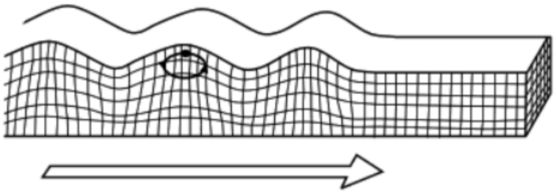

Figure 2.10: Deformations produced by Rayleigh waves (Reynolds, 2011).

Love waves only occurs where a a layer with low shear wave velocity lies over another layer with higher velocity. Love waves cause particles movement parallel to the surface plane and at right angles to the wave direction, as illustrated from figure 2.11.

The Velocity of the surface waves are approximately equal to the shear wave velocity. Love waves are polarised S-waves, and are therefore set to equal velocity as the the S-waves. Reynolds (2011) state that Rayleigh waves travel slightly slower than the S-wave at about 92 percent of the

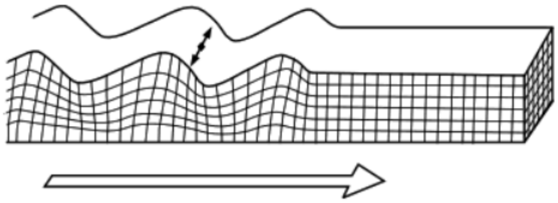

Figure 2.11: Love waves generate particle movement in the surface plane at right angles to the wave direction.

shear wave velocity for a material with Poisson's ratio of ν=0.25). with ν increasing towards 0.5 the velocity of Rayleigh wave propagation will increase towards the S-wave velocity, as can be seen from figure 2.9. For simplicity and practical reasons the velocity of Rayleigh and shear waves are considered to be approximately equal, and one get the relationship given in equation 2.21.

$$v_R = v_L = v_s \tag{2.21}$$

2.3 Shear Modulus, G

The equivalent linear model is a simple model for describing dynamic soil behaviour. The model describes the general shape of the hysteresis loop assuming linearity. This assumption is only reasonable for very small strains. In relation to the stress-strain loop, the inclination is decided by the shear stiffness of the material, which is described by the shear modulus, G_{tan}. The tangential modulus varies for every step along the loop, and is not a practical measure. To describe the general inclination of the loop, is is preferred to use an avarage value of G_{tan} over the entire hysteresis loop. This approximation is called the secant shear modulus, G_{sec} (Kramer,1996), and is given by equation 2.22. An illustration of G_{tan} and G_{sec} are given in figure 2.12

$$G_{sec} = \frac{\tau_c}{\gamma_c} \tag{2.22}$$

Where τ_c and γ_c are the shear stress and shear strain amplitude induced by a cyclic load. The secant modulus is more commonly referred to only as G.

The Shear modulus, G varies with the cyclic strain amplitude, and increased strain results in decreased G. By looking at the backbone curve, it becomes apparent that the inclination of the

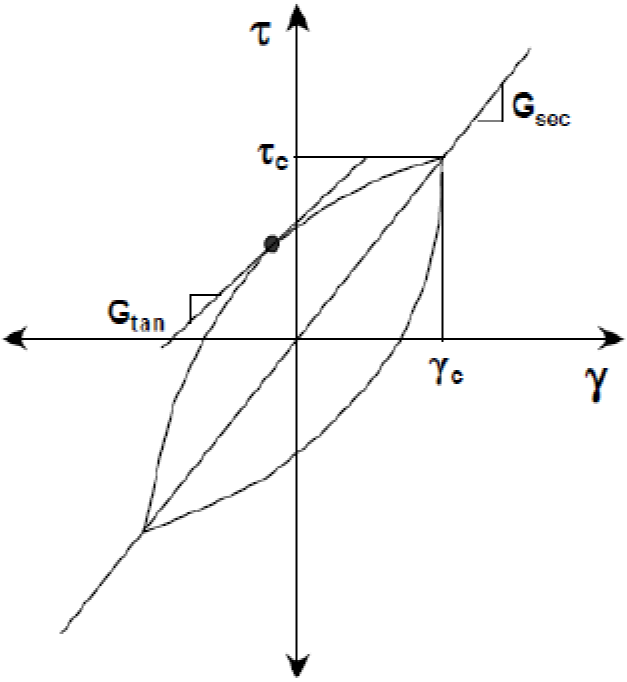

Figure 2.12: A generalised stress-strain loop, with principles for finding the tangential and the secant shear modulus (Kramer, 1996).

curve is steepest for lower levels of strain amplitude, yielding a high value of G. As the strain increases the backbone curve flattens out and the resulting secant shear modulus will be lower. This principle is illustrated in figure 2.13.

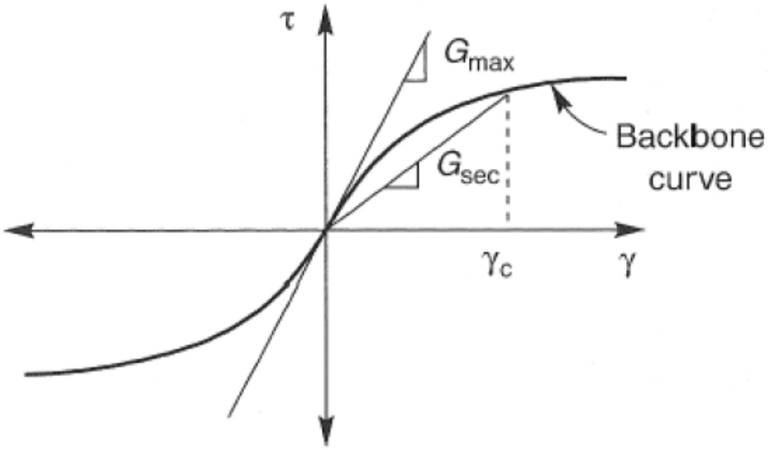

Figure 2.13: Secant shear modulus G_{sec} and small-strain stiffness G_{max} for the backbone curve (Kramer).

The small-strain stiffness is represented by G_{max} in figure 2.13, and is the inclination at zero dynamic strains. This stiffness is only applied for low strain levels, see chapter 3.

Chapter 3

Small-Strain Stiffness, G_{max}

The small strain stiffness, G_{max} often denoted G_0 is the shear stiffness of soil exerted to small strains, such that almost all strain exhibited are fully recoverable. The most common way of determining the small-strain shear modulus, is by measuring the shear wave velocity, v_s in field or by laboratory testing, then using the following equation (Kramer, 1996):

$$G_{max} = \rho v_s^2 \tag{3.1}$$

3.1 Strain Ranges

The maximum strain at which soils behave elastically is found to be very small, in the range of $\gamma_s \leq 1\times10^{-6}$, and are called very small strains. The small strain-strain stiffness in this range is considered a fundamental property of all soil materials under static and dynamic loading (Hoque Tatsuoka, 2004). Atkinson (2000) defines small strains as $\gamma_s \leq 1\times10^{-3}$, and strains $\gamma_s \geq 1\times10^{-3}$ are defined as larger strains. Figure 3.1 illustrates the modulus reduction curve with the different strain ranges.

The reduction curve show how the modulus ratio G/G_{max} varies with shear strain γ on the logaritmic scale. The curve contains the same information as the backbone curve (Kramer, 1996). As stated in chapter 2, the small-strain modulus is given by the inclination of the backbone curve at zero strains. The modulus ratio is therefore approximately equal to 1, for very small strains. As shear strain increases the modulus ratio decreases to values less than one

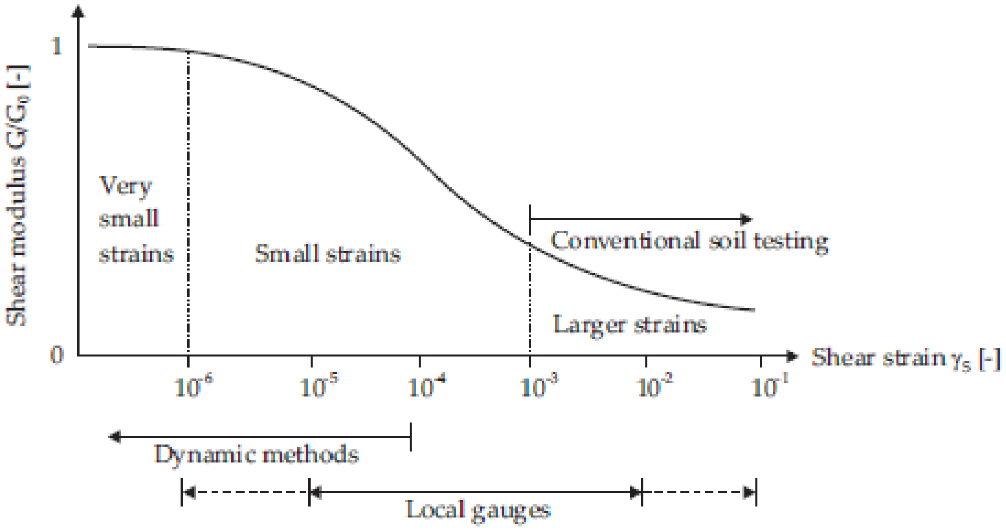

Figure 3.1: Characteristic stiffness and definitions of strain ranges (Atkinson, 2000).

(Atkinson, 2000). Since shear stiffness varies with cyclic strain amplitude, it is important to evaluate both the G_{max} and the modulus ratio G/G_{max} to get a good overview of the stiffness of a geological material (Kramer, 1996)

3.2 Parameters Affecting the Small-Strain Shear Stiffness

To get a good understanding of the small-strain stiffness, and to better understand the its decay and damping behaviour, this section will address the parameters that affect G_{max}. The most important parameters are regarded as the strain amplitude, confining stress, void ratio and the degree of interparticle bonding between soil grains (Benz, 2007).

3.2.1 General

An expression for G_{max} including all parameters influencing it was presented by Hardin (1978). This relationship is given in equation 3.2

$$G_{max} = AF(e)\sigma'^{\,n}_{m}\sigma_r^{(1-n)}(OCR)^k \tag{3.2}$$

Where the included parameters are as follows:

- A: Constant dependent on soil type and reference stress.
- F(e): A function of void ratio.
- σ'_m: Mean effective confining stress.
- σ'_r: Reference stress, most commonly set to atmospheric pressure equal to 100 kPa.
- OCR: Overconsolidation ratio.
- n and k: exponents varying for different soil types.

Several other variations of this equation exist including equation 3.3 (L'Heureux & Long, 2016).

$$G_{max} = AF(e)(\sigma'_v \sigma'_h)^n \sigma_r^{(1-2n)} \tag{3.3}$$

Later research has found more parameters influencing the G_{max}, such as the time consolidation which is a function of plasticity index, I_p (Vucetic Dobry, 1991). Other parameters include degree of saturation (Stokoe Santamarina, 2000), post-depositional processes like diagenesis, cementation and ageing (Mitchell, 1993). All parameters considered to affect the small-strain stiffness is compiled in figure 3.2 (Knudsen, 2014), describing how they affect the G_{max}, and in figure 3.3 addressing which soils the parameters are more relevant for (Benz, 2007).

In order to to better describe the small strain stiffness, and to quantify its day, it is useful to introduce the following terminology:

- G_0 denote the maximum small strain shear modulus, instead of using G_{max}.
- $G_{0.7}$ denote the small strain shear modulus after its decayed to 70 % of the initial maximum value G_0.
- $\gamma_{0.70}$ denote the shear strain when the shear modulus has decayed to $G_{0.7}$.

The damping of the small strain stiffness with applied strain can be described by the degradation curve using the points $(G_0, 0)$ and $(G_{0.7}, \gamma_{0.70})$. In model proposed by Hardin Drnevich, the behaviour of the entire degradation curve can be extrapolated from these points (Hardin Drnevich, 1972). With this model, the shear strain $\gamma_{0.70}$ is related to the damping. for high values of $\gamma_{0.70}$, the less damping is present. The normalized Hardin-Drnevich relationship is given by figure 3.4

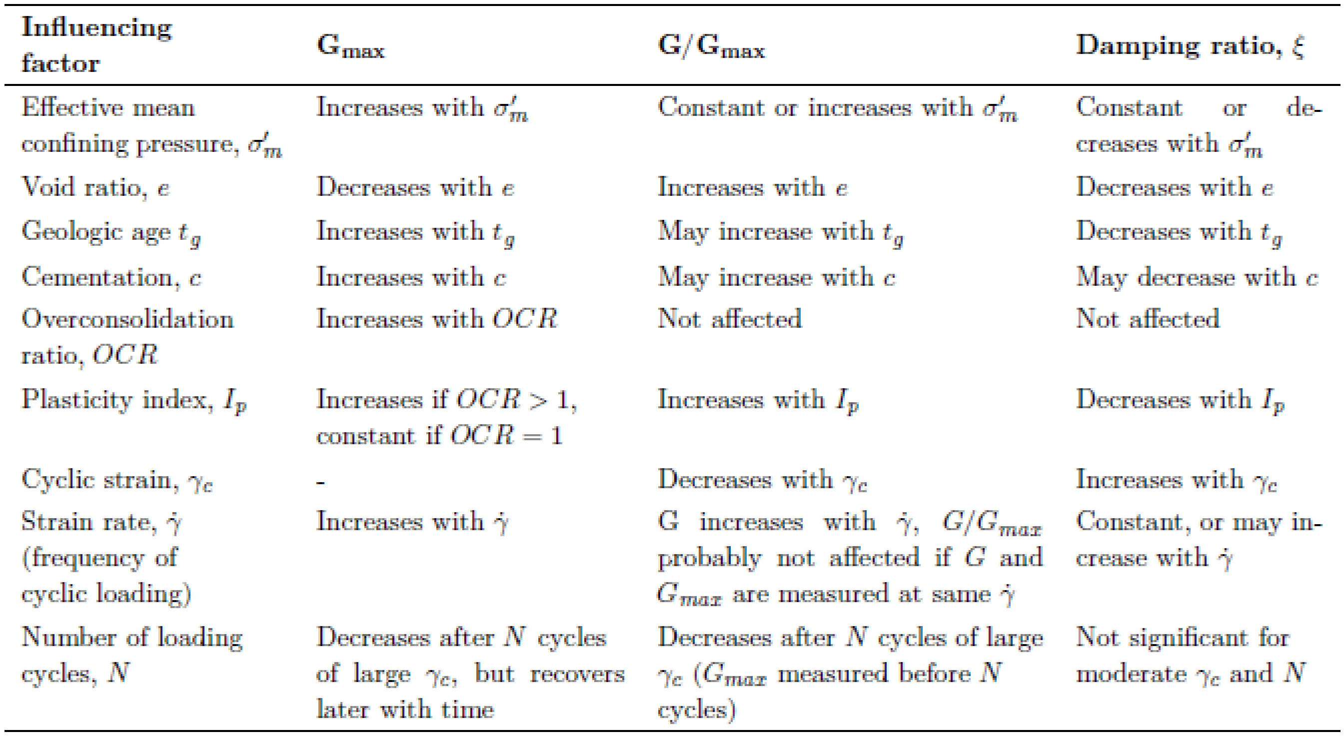

Influencing factor	$\mathbf{G_{max}}$	$\mathbf{G/G_{max}}$	**Damping ratio, ξ**
Effective mean confining pressure, σ'_m	Increases with σ'_m	Constant or increases with σ'_m	Constant or decreases with σ'_m
Void ratio, e	Decreases with e	Increases with e	Decreases with e
Geologic age t_g	Increases with t_g	May increase with t_g	Decreases with t_g
Cementation, c	Increases with c	May increase with c	May decrease with c
Overconsolidation ratio, OCR	Increases with OCR	Not affected	Not affected
Plasticity index, I_p	Increases if $OCR > 1$, constant if $OCR = 1$	Increases with I_p	Decreases with I_p
Cyclic strain, γ_c	-	Decreases with γ_c	Increases with γ_c
Strain rate, $\dot{\gamma}$ (frequency of cyclic loading)	Increases with $\dot{\gamma}$	G increases with $\dot{\gamma}$, G/G_{max} probably not affected if G and G_{max} are measured at same $\dot{\gamma}$	Constant, or may increase with $\dot{\gamma}$
Number of loading cycles, N	Decreases after N cycles of large γ_c, but recovers later with time	Decreases after N cycles of large γ_c (G_{max} measured before N cycles)	Not significant for moderate γ_c and N

Figure 3.2: An overview of the parameters affecting G_{max} and the effect they have (Knudsen, 2014).

3.2.2 Shear strains and loading history

The small strain shear stiffness G_{max} is the initial shear stiffness before the soil is subjected to shear strains, which is why it is also denoted G_0. This initial shear stiffness is only conserved at very small strains, meaning that the material will recover its stiffness upon load reversals. As the shear strains increase, the shear stiffness will decrease. This means that all excess strain that is accumulated over the load cycles, will contribute to the reduction of the small strain stiffness. The accumulated strain for one loading cycle is called the *strain amplitude*. In research it is most common to use the shear strain γ_s, which is the deviatoric strain amplitude (Benz, 2007).

The hysteresis in stress-strain behaviour can be described by *Masing's Rule*, which states the following (Chiang, 1999; Benz, 2007):

1. The shear modulus in unloading is equal as the initial tangent modulus for the initial loading curve.
2. The unloading-reloading curves will have the same shape as the initial loading curve, but

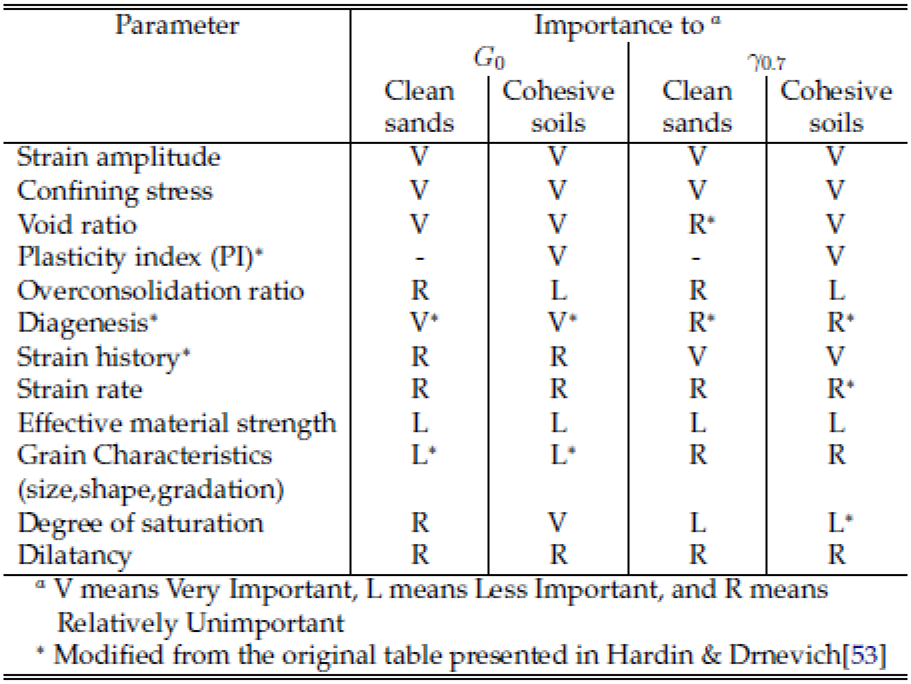

Parameter	Importance to [a]			
	G_0		$\gamma_{0.7}$	
	Clean sands	Cohesive soils	Clean sands	Cohesive soils
Strain amplitude	V	V	V	V
Confining stress	V	V	V	V
Void ratio	V	V	R*	V
Plasticity index (PI)*	-	V	-	V
Overconsolidation ratio	R	L	R	L
Diagenesis*	V*	V*	R*	R*
Strain history*	R	R	V	V
Strain rate	R	R	R	R*
Effective material strength	L	L	L	L
Grain Characteristics (size,shape,gradation)	L*	L*	R	R
Degree of saturation	R	V	L	L*
Dilatancy	R	R	R	R

[a] V means Very Important, L means Less Important, and R means Relatively Unimportant

* Modified from the original table presented in Hardin & Drnevich[53]

Figure 3.3: An overview of the parameters affecting G_{max} and what soils the given parameters are most relevant (Benz, 2007).

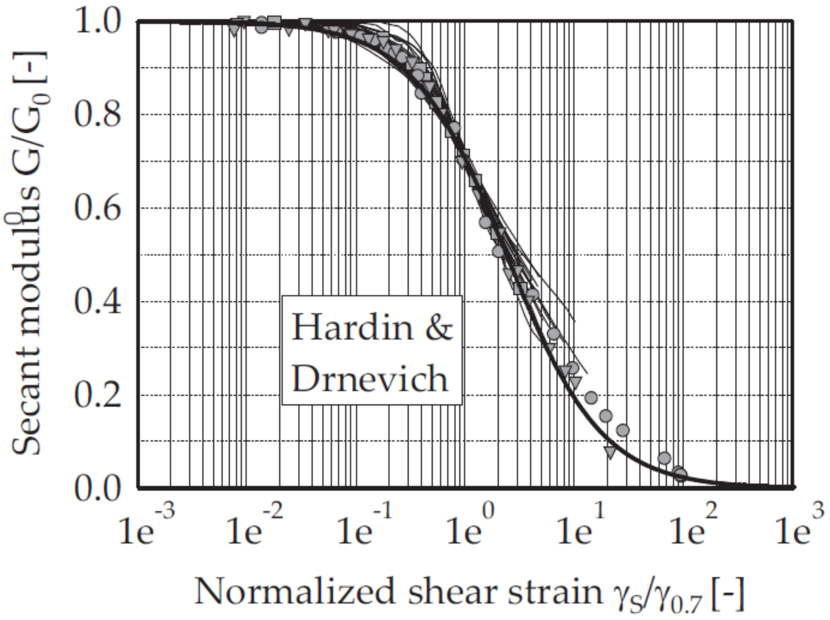

Figure 3.4: Normalized modulus reduction curve by Hardin-Drnevich (modified version by Benz, 2007)

will be larger by a factor of approximately two. This relationship is described in equation 3.4

$$(\gamma_{0.7})_{initial} = 0.5(\gamma_{0.7})_{reloading} \tag{3.4}$$

Masing's first rule imply that if an interior curve under continued loading or unloading crosses a curve described by a previous load cycle, the curve will follow that of the previous load cycle. Masing's second rule implies that the equation for any hysteretic response can be obtained by investigating the initial (virgin) loading curve using the latest point of load reversal (Chiang, 1999). The principle of Masings rule is illustrated in figure 3.5 showing a hysteresis loop for an arbitrary response

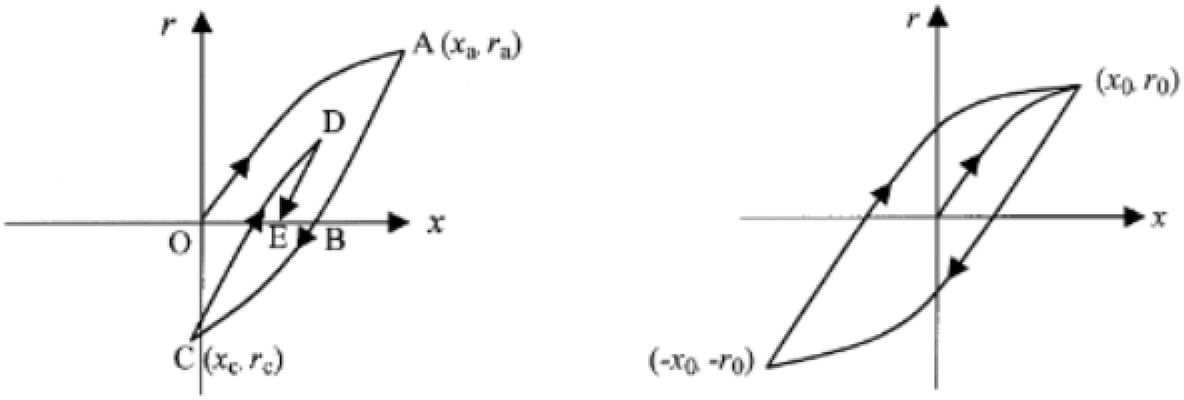

Figure 3.5: Right side showing a hysteretic curve for an arbitrary response. Right side showing a steady-state cyclic hysteretic response.

The hysteresis curves in figure 3.5 are force-displacements curves, where r is the restoring which corresponds to a displacement x. The hysteresis curve on the right show a steady-state cyclic hysteretic response, indicating that the unloadiing and reloading response is geometrically similar, illustrating Masing's first rule. The curve on the left is a hysteresis loop for an arbitrary response, where OA is the initial virgin loading curve.The curve is unloaded from A to C, then reloaded from C to D. From this figure it is easy to see that, if the loading has continued a closed hysteresis loop ABCDA would form. Similarly if unloading DE would be continued it would reach point C, forming another closed hysteresis loop (Chiang, 1999).

3.2.3 Confining stress

As stated in equation 3.2, Hardin (1978) proposed a dependency between the small strain shear modulus and given by equation 3.5. There is wide agreement in this relationship, and that increased confining stress leads to increased small strain shear stiffness, i.e. damping decreases with increased confining stress (Jamiolkowski et.al, 1991; Shibuya et.al, 1992; Vucetic Dobry, 1991; Benz, 2007). This relationship is illustrated in figure 3.6, with density index $I_D = \frac{e-e_{min}}{e_{max}-e_{min}}$ accounting for the impact of void ratio (Wichtmann Triantafyllidis, 2004).

$$G_0 \propto (\sigma'_m)^n \tag{3.5}$$

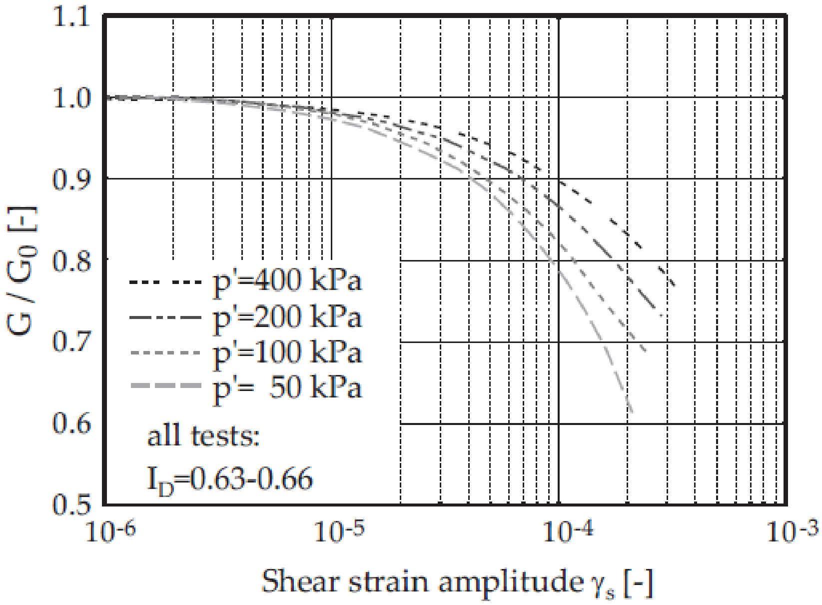

Figure 3.6: The influence of confining pressure (here denoted by p') on the normalized reduction curve. Increased confining pressure leads to increased small strain shear modulus, G_0 (Wichtmann Triantafyllidis, 2004)

The confining stress is expressed as the mean effective stress, σ'_m. For an anisotropic stress state it is suggested to use $\sigma'_m = (\sigma'_1 + \sigma'_3)/2$, as the effect of a principal stress direction σ'_2 normal to the wave propagation plane is negligible. Furthermore, G_{max} is equally dependent on the principle stress direction of wave propagation and particle movement (Jamiolkowski et.al, 1991). The power exponent n varies in the range $0.40 \leq n \leq 0.55$ for non-cohesive soils. The value of n varies more for cohesive soils, as research has indicated values from 0.5 and up to 1 (Benz, 2007). The confining stress and its exponent n therefore play a big role in the degradation of G_{max} for clays. As seen from equation 3.2, the G_{max} is also influenced by void ratio e, which is also affected by the confining stress.See section 3.2.5 for how the influence of void ratio. Studies show that the power exponent n can be correlated to the plasticity index I_P and the liquid limit, w_L (Viggiani & Atkinson, 1995; Hicher, 1996). By assuming constant void ratio, Viggiani & Atkinson (1995) showed that for a large number of clay samples at very low strains, the exponent n increases with increased plasticity, as shown in figure 3.7. Hicher (1996) compiled the results from clay tests against the liquid limit, given in figure 3.8. The plot show relatively good agreement with the results of Viggiani & Atkinson, give further indications on how to set the value of n for clays.

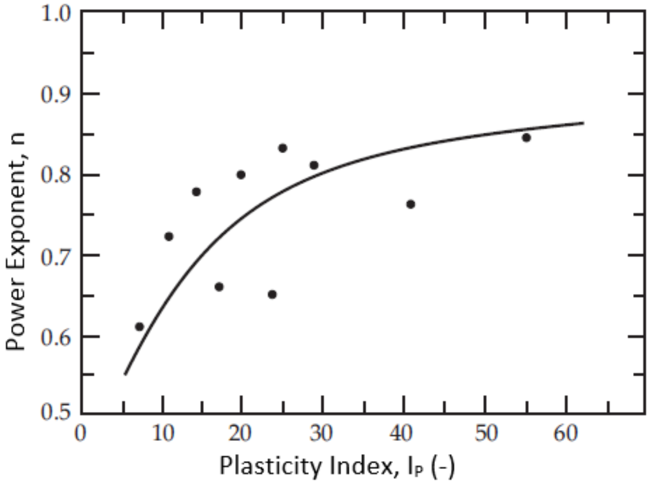

Figure 3.7: Exponent n correlated against plasticity index for clays (Viggiani & Atkinson, 1995)

3.2.4 Overconsolidation Ratio, OCR

From equation 3.2, Hardin (1978) proposes that G_0 (G_{max}) is dependent on the overconsolidation ratio (OCR). The OCR is defined as the ratio of the highest past vertical effective stress to the current vertical effective stress , and is a measure how much stress the soil have previously experienced. The expression for OCR is given in equation 3.6, and the small strain shear modulus' empirical dependence on OCR is given by equation 3.7. The factor k varies between zero for sands and 0.5 for soft sensitive clays (Benz, 2006).

$$OCR = \frac{\sigma_{v,OC}}{\sigma'_v} \tag{3.6}$$

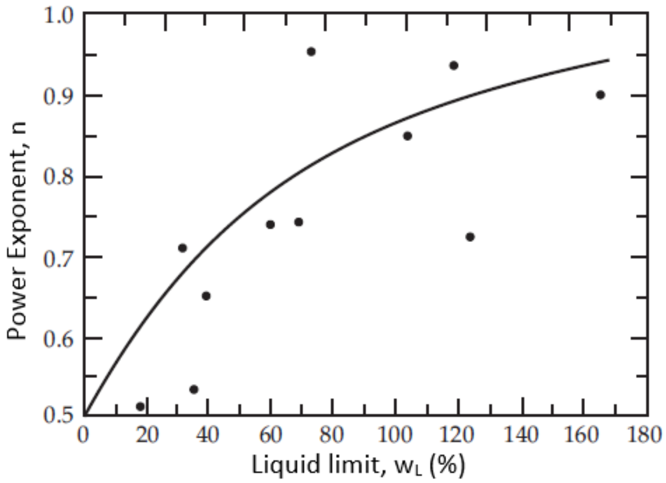

Figure 3.8: Exponent n correlated against liquid limit for clays (Hicher, 1996)

$$G_0 \propto (OCR)^k \tag{3.7}$$

Overconsolidation has small impact on the normalized modulus reduction curve for non-plastic materials. However, in plastic soils overconsolidation tend to increase the $\gamma_{0.70}$ value. This indicates that increased OCR for soils with high plasticity, reduces the damping of seismic signals. The increased $\gamma_{0.70}$ can by calculated by the empirical relationship given by equation 3.8. $(\gamma_{0.70})_{ref}$ is a reference shear strain corresponding to the shear strain value when the small strain stiffness is reduced to 70 % from its initial value, for a non-plastic ($I_P = 0$), non-OC (OCR = 1) soil. This relationship showed best agreement for overconsolidated soils with high plasticity (Stokoe et.al, 2004).

$$\gamma_{0.70} = (\gamma_{0.70})_{ref} + 5 \times 10^{-6} I_P (OCR)^{0.3} \tag{3.8}$$

The parameter k increases with plasticity for clays. The influence of OCR has been debated to not have significant impact on the small strain stiffness G_0. To better understand the impact of OCR on the small strain shear modulus G_{max}, Viggiani Atkinson (1995) suggested using the term $R_0 = \frac{\sigma'_{m,OC}}{\sigma'_m}$ giving a new equation for the dependency of the overconsolidation ratio. This equation is given in equation 3.9.

$$G_0 \propto R_0^k \tag{3.9}$$

The exponent k in equation 3.9 is again a function of plasticity and will increase with increased plasticity index, I_P. Using this relationship studies found that for clays with plasticity index ranging from 10 to 40, the k-value was found to be within the ranges $0.20 < k < 0.25$. This small variation may indicate that the effect of OCR on G_0 is negligible (Atkinson & Viggiani, 1995; Hardin, 1978) . Research conducted by Shibuya et.al (1992) showed by correcting for void ratio (e), soils with OCR between 1 and 4 indicated negligible influence on the small strain shear stiffness. the study suggested that by giving a good estimate for *F(e)* function in equation 3.2, the OCR dependency could be removed. Thid is the reason why OCR is not included in the proposed empirical relationship given from equation 3.3.

3.2.5 Void Ratio

Over the last 60 years, many different suggestions for the void ratio function F(e) has been suggested. Hardin & Richart (1963) initially proposed a linear relationship between void ratio e and wave propagation velocity. This resulted in the depencies given in equations 3.10 and 3.11 for sands with well-rounded grains and angular grains respectively.

$$G_0 \propto \frac{(2.17-e)^2}{1+e} \tag{3.10}$$

$$G_0 \propto \frac{(2.97-e)^2}{1+e} \tag{3.11}$$

Hardin & Black (1972) found that equation 3.11 gave a relatively good fit for clays. Later research has done many modifications to the void ratio function F(e). The equations by Hardin & Black (1963) is still commonly used for sands, with small variations in the number in the numerator (Benz, 2007; Hoque & Tatsuoka,2004; Kuwano & Jardine). Another common form of the function is described by equation 3.12.

$$F(e) = \frac{1}{e^x} = e^{-x} \tag{3.12}$$

Where x varies for different soil types. This formulation is sometimes used for sands with x varying between 0.8 for coarser sands and up to 1.3 for finer sands. The void ratio function in equation 3.12 is more commonly used for clays with with x ranging between 1.10 and 1.52 for different clays (Lo Presti & Jamiolkowski, 1998; Jamiolkowski, 1991).

No matter the equation chosen for F(e), there is broad agreement That G_{max} (G_0) decreases with increased void ratio (Vucetic & Dobry, 1991). Damping due to void ratio is more prevelent for cohesive soils as these soils are more compressible. As mentioned in section 3.2.3, the void ratio is related to the confining stress. As the confining stress increases, the void ratio will decrease, resulting in less damping and higher G/G_0. Void ratio is also a function of the plasticity, as higher plasticity generally given a more open and porous structure (Benz, 2007)

3.2.6 Soil Plasticity

As stated in section 3.2.4, the power exponent k is a function of the soil plasticity, i.e. the plasticity index I_P. Plastic soils, such as clay give higher values for k. From equation 3.2, one can see that the G_{max} dependency of k does only apply when OCR $\neq$ 1. Normally consolidated soils with OCR = 1 will therefore not have a contribution from the value of k. However, for overconsolidated soils, the G_{max} will increase with increased plasticity. results compiled by Vucetic & Dobry (1991) showed the impact of the plasticity index on the normalized modulus reduction curve. From figure 3.9 one can see the impact increased plasticity has on the degradation of G_{max} (G_0).

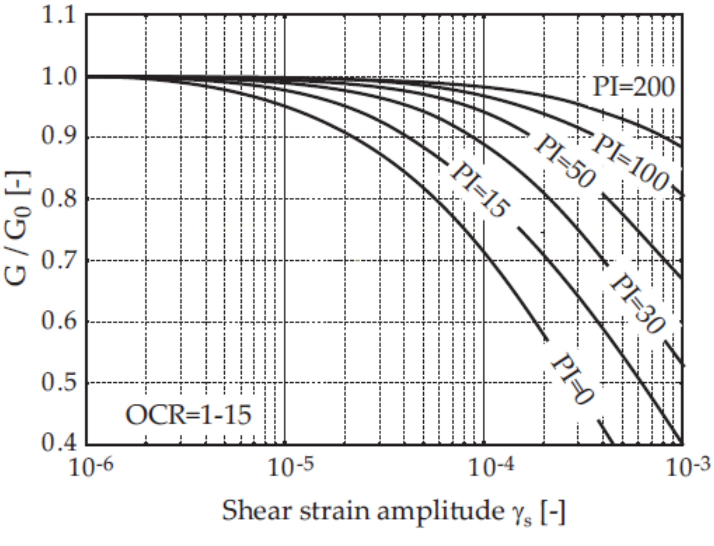

Figure 3.9: Normalized modulus reduction curve for soils with varying plasticity index. The figure only show the section for small strains. The soils included have OCR in the range of 1 to 15 (Vucetic & Dobry, 1991)

As many of the parameters affecting the G_{max} is a function of soil plasticity, the impact plasticity has on the parameters are covered in the respective parameter sections.

3.2.7 Anisotropy

Research conducted by Hoque & Tatsuoka (2004) show that G_{max} increase in the direction of major principle stress σ'_1 for stress ratios $\frac{\sigma'_1}{\sigma'_3} > 1$. Meanwhile, the stiffness in the direction of σ'_3 remains unaffected up to $\frac{\sigma'_1}{\sigma'_3} = 3$, after which the stiffness will be reduced (Hoque & Tatsuoka, 2004; Yu & Richart, 1984).

Sully & Campanella (1995) investigated variations shear wave velocities with anisotropy. They suggested an equation for the shear wave velocity under small strains dependent on the confining stress σ', and soil fabric. The relationship is given in equation 3.13

$$v_s = C_s(\sigma')^n \tag{3.13}$$

Where C_s is constant expressing the soil structure, while the power exponent n is dependent on stress.By examining isotropic and anisotropic shear waves in cross-hole and down-hole field tests, Sully & Campanella (1995) could evaluate how sensitive v_s, and therefore G_{max} is to anisotropy. An isotropic s-wave is a shear wave with propagation and particle movement in the same direction. An anisotropic s-wave have propagation and particle movement direction in different planes, and are exerted to different stress. By having the down-hole investigation transmitting waves with vertical propagation and horizontal particle movement (VH-waves), and cross-hole test transmitting waves with horizontal propagation and vertical particle movement, they could measure how sensitive G_{max} is to stress anisotropy. The finding of Sully & Campanella showed that the two field tests yielded different velocities for the same constant C_s, indicating different stress dependency in the direction of wave propagation and particle movement. However later testing using both isotropic and anisotropic wave velocities gave equal velocity measurements, contradicting the earlies results. After further investigations, they concluded that the difference in s-wave velocities in different planes is more sensitive to variations in the constant C_s, than to variations in effective stress state (Sully & Campanella, 1995; Knudsen, 2014).

G_{max} is therefore more dependent on the inherent structural anisotropy, than the stress anisotropy. The structural anisotropy is a a function of the soils genesis such as transport, depositional history and diagenesis. Due to these processes, the stiffness is often higher in the horizontal bedding plane than in the vertical plane (Benz, 2007). Considering the the research indicating the existence of stress induced anisotropy, one can argue that assuming isotropic stiffness may be reasonable since the inherent structural anisotropy compensates for the stress induced anisotropy for normally consolidated soils (Benz, 2007; Hoque & Tatsuoka, 2004). Other research suggest that G_{max} is independent of stress induced anisotropy, where only structural anisotropy will affect the shear wave velocity (Sully & Campanella, 1995).

3.2.8 Diagenesis

As mentioned in section 3.2.7, diagenesis have an impact on the soil stiffness. Diagenesis is the sum of all processes that cause changes in the sediment after its deposition and before lithification. Diagenesis is often mistaken as metamorphism, since both prosesses alter the soil properties. However, diagenesis happens at relatively low temperature and pressure, while metamorphism requires high temperature and pressure. Diagenesis is dominated by chemical reactions between different minerals, and is affected by changes in interstitial water content and temperature (Britannica, n.d.). Diagenesis also included processes such as burial, compaction and precipitation. The chemical processes in the soil can change the mineralogy, interparticle texture and bonding . Any alteration of the soil structure will alter the soil stiffness over time. Changes in stiffness due to diagenesis is dominated by *cementation* and *aging*. Cementation is the process of minerals precipitating from solution, hence cementing the soil grains and increasing the small strain stiffness. Aging is defined as a chenge in physical properties due to a secondary compression under a constant external load, which increases the small strain stiffness. Cementation is most important to the stiffness of sands, while aging is most prevalent in clays (Benz, 2007).

The increase in G_{max} due to diagenesis, may be lost when changing the stress state of the soil. This is contributing factor to why disturbed samples have significantly different small strain stiffness than undisturbed samples (Lo Presti et.al, 1996).

3.3 Field Tests

In this section field tests for acquisition of data used for determination of G_{max} is presented. Field tests allow for measuring the in situ soil properties, with the soil under its original chemical, hydrological, thermal and stress conditions. This eliminates many of the challenges associated with disturbance when soil sampling. In situ field tests allow for a larger soil body to be investigated, which eliminate the risk of assigning properties to a large area based on a small unrepresentative samples.

In the following subsections, a description will be given to the different tests relevant for this thesis.

3.3.1 Cross-Hole Seismic Method

The cross-hole seismic method is an increasingly important method for determining shear wave velocities, and shear modulus of the subsurface. For loading situations where no permanent soil displacements occur, the soil response to an input wave is mostly controlled by the shear modulus and damping ratios of the penetrated medium. At larger strains these dynamic properties are non-linear, with a shape and orientation, which are best suited to determine using laboratory testing. However, for small strains the cross-hole method is one of the easiest and most accurate method for determining the small-strain shear modulus, G_{max} (Hall & Bodare, 2000). All of the dynamic elastic moduli of a material can be determined from the knowledge of in-situ density, P- and S-wave velocities. Since determination of density is is standardised in laboratory tests, acquiring information on seismic velocities yields important information of a site. The cross-hole method is probably the most reliable methods for in-situ small-strain stiffness testing, making it an important tool for on site soil characterisation (EPA, 2016). This chapter will address the cross-hole method, the procedure and analysis.

Methodology

The seismic cross-hole test is utilised in two or more boreholes, with one hole being used to generate a signal at one or more depths. The other boreholes contain a receiver, such as a geophone, oscilloscope or a hydrophone if beneath water level. For boreholes with a know distance from one another, one measure the travel time from the seismic signal is initiated to the time the receivers pick up the signal. This allows for calculation of average wave velocity along each path (Reynolds, 2011). The method is preferably done with two or more receiver holes, since measuring wave travel times between adjacent receivers eliminate sources of error due to site anisotropy, or failure in measuring signal triggering time and receiver times (Kramer, 1996). Figure 3.10 gives an example of a trigger/receiver layout (EPA, 2016).

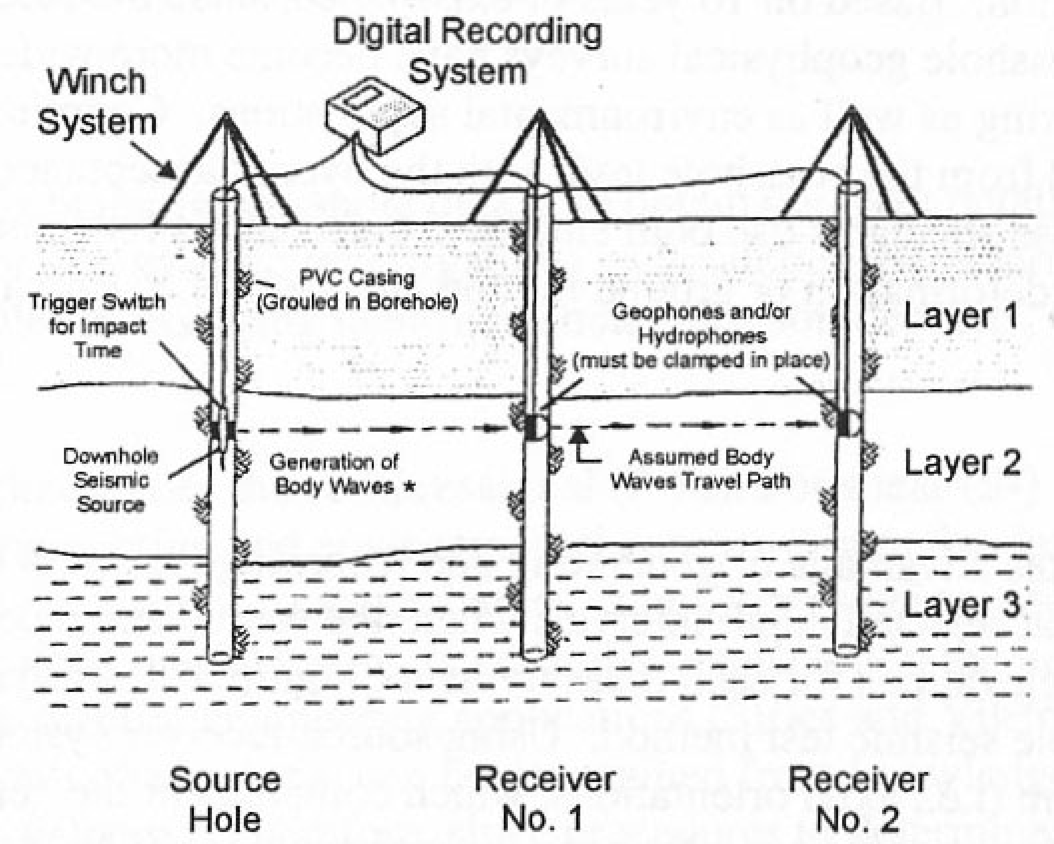

Figure 3.10: The trigger generates seismic body waves, while geophones placed to the same depth in other boreholes pick up the signal

The cross-hole method generate and record seismic waves at fixed depths, maintaining equal elevation of signal transmitter and receiver. The signal source and the receiver is then moved up or down in the borehole to a new elevation, and another test is performed. by doing this procedure for several depths, one can produce a velocity profile. The cross-hole method is therefore most viable when the formation layering is horizontal. The type of body wave generated is dependent on source type. P-waves are generally generated with a sparker or an explosive device (Kramer, 1996).

For cross-hole tests in unconsolidated, undrained soils, the P-wave velocity measurements are affected by the degree of saturation. As the water content and the degree of saturation increases towards 100%, the Poisson's ratio, ν will climb towards values of 0.5, and is no longer valid to represent the soil characteristics. Hence, for undrained formations with high water content, such as for marine clays, the P-wave is commonly called the fluid. The P-wave velocity is then governed by the pore water, and not the geologic material (EPA, 2016).

When instead generating S-waves for cross-hole testing, waves are typically generated by a blow of hammer to a metal rod. the waves may be split into two wave types with different particle motions. The two polarisations, SH (horizontal) and SV (vertical) allows for testing of the material in two different directions. Normally, the SV-wave is used for cross-hole testing. The SV-wave is both easier to generate and record due to better availability of commercial impact hammers, or other mechanical impulse sources with reversible directions of impact. The vertically polarised wave has horizontal propagation direction, but vertical particle motion, which allows for testing with only one vertical geophone in each borehole. The option to reverse the polarity of the wave signal is key to high quality data interpretation (EPA, 2016)

Advantages

The main advantages of the cross-hole method is that it is relatively simple and reliable with regards to measuring the dynamic soil properties. With the minimum of two boreholes one does not need to do extensive drilling. Since the wave only propagates horizontally on the same height there is no attenuation with depth (Frost & Burns, 2003). From the velocities measured, one can calculate the G_{max}, often without accurate information about the exact density of the soil, which may eliminate the need for lab tests (Benz, 2016). another advantage with the method is that it can detect hidden layers, which other seismic methods may not detect (Kramer, 1996).

Limitations

Due to the need for boreboles, the cross-hole method is more expensive than seismic refraction surface tests. Considering the need for a drill rig and operators, there is both extra execution costs and labour costs attached (Knudsen, 2014). Currently, with the use of impact sources are susceptible to disturbance from the P-waves. A source which does not generate sufficient shearing may be harder to interpret if disturbed by P-wave response. The method is also sensitive to trigger and receiver orientation, and one must have caution when placing the censors (Luna Jadi, 2000).

3.3.2 Spectral Analysis of Surface Waves (SASW)

In geotechnical engineering Rayleigh waves are most commonly used for assessment of shear wave velocities close to the surface. As mentioned in 2.2.1 under surface waves, the Rayleigh waves are dispersive, such that the velocity of propagation of a Rayleigh wave is dependent on wavelength. The surface methods are non-destructive, not requiring any boreholes. Both source and receivers are placed at ground level allowing for fast and easy setup and testing, yielding high repeatability (Ismail et.al, 2001).

In principle, the surface waves propagate along the surface of a halfspace with decreasing amplitude with depth. Rayleigh waves propagate away from the source along a cylindrical wave front. Due to both vertical and horizontal particle movement, deformation associated with Rayleigh waves is a result of elliptical particle motion , as explained in section 2.2.1 under surface waves. In a homogeneous, isotropic and elastic half-space, the velocity of Rayleigh waves are unaffected by variations in frequency. But for real soils there will layering and variation in stiffness with depth, which means Rayleigh wave velocity varies with frequency (or wavelength), given by equation 3.14.

$$\lambda = \frac{V_R}{f} \tag{3.14}$$

This frequency dependence of Rayleigh wave propagation velocity in a layered system is called dispersion. The dispersive characteristics of Rayleigh waves can be described from the phase velocity, which is the velocity a seismic disturbance of a given frequency propagates through a medium (Ismail et.al, 2001). Rayleigh waves with short wavelengths or high frequency will be affected by soil closer to the surface. Waves with longer wavelengths or lower frequencies will penetrate deeper and therefore be influenced by materials deeper in the ground.

The principle of the Spectral Analysis of Surface Waves (SASW) is to generate a wide range of frequencies from a source and use dispersion to produce velocity and frequency correlations called dispersion curves (Long et.al, 2008). Two receivers are placed vertically on the ground at a distance *d* from one another. A hammer can be used to generate seismic energy. A dynamic signal analyser collects the response from the receivers, and transform the output to the frequency domain, allowing for collection of data. An illustration of the setup is given in figure 3.11a . Several sets of tests with different receiver spacing are required to sample the different layers in the subsurface. Short spacing with high frequencies for shallow layers, and long spacing with low frequencies for deeper layers. This is illustrated in figure 3.11b (Ismail et.al, 2001).

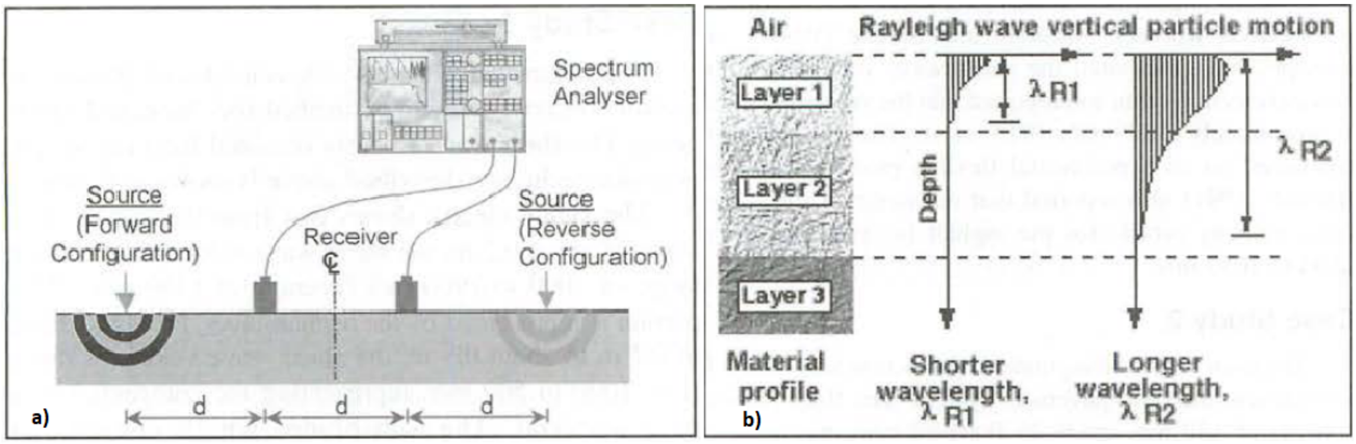

Figure 3.11: figure a) show a basic configuration of the equipment used for SASW testing.A dynamic signal analyser, the spectrum analyser collects and transforms the receiver data to te frequency domain. Figure b) illustrate how low frequencies (longer wavelengths) penetrate to a greater depth, than signals with high frequency (shorter wavelengths) (Ismail et.al, 2001).

From the frequency domain two functions are vital for the results. the first function is the *coherence function*, which is a measure of linear correlation between the input and output signals. Coherence function values close to one signify good correlation, and the recorded data can be considered trustworthy and unaffected by noise. The second function is the phase information of the cross power spectrum between receivers. The cross power spectrum is used to obtain the relative phase shift between two signals at each frequency in the range of frequencies excited in the SASW test. The phase shift is translated into travel times (Ismail et.al, 2001)

One of the biggest advantages of the SASW method and other surface wave tests, are that they are non-destructive, not requiring any boreholes. The testing can be relatively easy and quick, but will require increasing time and workforce if several measurements with different configuration is needed (Long et.al, 2008; Ismail et.al, 2001). The method also allows for testing to great depths (Kramer, 1996). SASW testing is particularly good for irregular profiles, allowing for easy detection of varying soil layers. The method can find softer layers trapped between stiffer layers, stiff layers trapped between softer layers, as well as softer layers deeper in a soil profile (Ismail et.al, 2001).

3.3.3 Multichannel Analysis of Surface Waves Test (MASW)

The multichannel analysis of surface waves is similar to the SASW method. It is a non-destructive surface wave method that enable acquisition of key geotechnical parameters such as shear and bulk moduli found from v_s and v_p of materials near the surface. While the SASW method analyses only one type of seismic waves (the fundamental-mode Rayleigh waves) recorded by two receivers, the MASW identifies each type of seismic waves on a multichannel record (Park et.al, 2001).

When a source generate seismic waves, both body waves and surface waves are generated simultaneously. As the body waves consist of direct, reflected, refracted and air waves, the surface waves is made up of the fundamental and higher modes of Rayleigh waves. MASW identifies each type of seismic waves on a multichannel record using pattern recognition techniques. this recognition leads to the setup of a optimum field configuration which yield the highest signal-to-noise ratio possible. By including many of the different types of waves, the MASW method can generate cross sections of v_s from the surface waves, as well as v_p from analysis of the refracted waves.

A schematic showing a MASW setup is given in figure 3.12. An impact of a hammer is ypically used as seismic source. The MASW method is normally carried out by deploying a number of receivers in a linear pattern with equal spacing. Each receiver is connected to an individual recording channel. A measurement is made up of multiple recordings of seismic wavefields, called *traces*, at different offsets from the source (Park et.al, 2001).

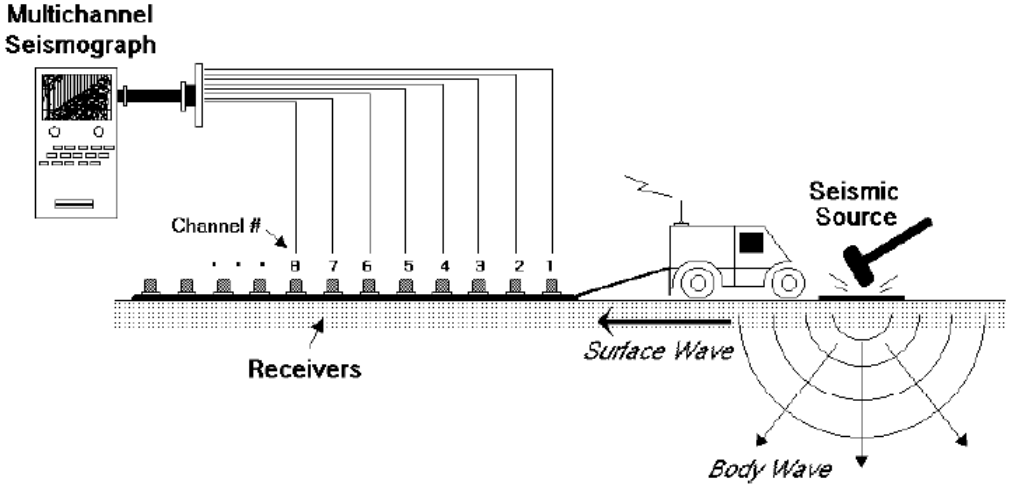

Figure 3.12: An illustration of a MASW field configuration, and instruments used during field survey (Park et.al, 2001).

The main advantages of the MASW method are pattern recognition capability and redundancy in measurements. The pattern recognition allows for quility control both during data acquisition and processing. It makes it possible for identification of body and surface waves separately, due to their unique patterns of amplitude and arrival times. Redundancy in measurements allows for noise suppression techniques to optimize the signal-to-noise ratio. The standard configuration for the MASW during field survey, is the same as the one used for Common Depth Point (CDP) reflection surveys, enabling the MASW method to be applied to reflection, or refraction data (Park et.al, 2001). Since the MASW method allows for between 12 to 60 receivers to be used at the same time, the data acquisition is highly effective, and the work load is significantly reduces compared to that of the SASW method (Long et.al, 2008).

3.3.4 Seismic Dilatometer Test (SDMT)

The seismic dilatometer (SDMT) is the combination of the standard mechanical flat dilatometer (DMT) with a module for measuring shear wave velocity, v_s. The seismic module is a cylindrical device equipped with two receivers, spaced by a 0.5 m distance. Such a configuration with two receiver is often called the *True-Interval Test*, and is preferred over a single-receiver setup due to better accuracy in the determination of the zero-time at hammer impact. The receiver deviced is either pushed into the subsurface or placed in a predrilled hole. a seismic source such as the blow of a hammer to a metal plate is placed on the surface. The seismic signals recorded by the receivers at a given depth correspond to the same hammer blow, and not to different blows in sequence. This gives the measurements of v_s from SDMT good repeatability. The shear wave velocity is found by calculating the ratio between the difference in distance between the receivers and the source (L_2 - L_1) and the delay in arrival time from the first to the second receiver (t_2 - t_1) (Marchetti et.al, 2008). The setup of a seismic dilatometer test is illustrated in figure 3.13 (Campanella & Steward, 1992) and equation for finding v_s is given in equation 3.15.

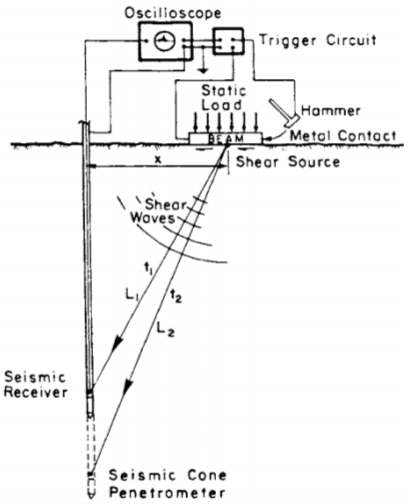

Figure 3.13: An illustration of a SDMT setup and parameters required for calculation of shear wave velocity (Campanella & Steward, 1992).

$$v_s = \frac{L_2 - L_1}{t_2 - t_1} \tag{3.15}$$

The wave source at the surface a steel plate being hit by a pendulum hammer horizontally. The steel plate is pressed against the ground with its longest axis parallel to the direction of the receivers, and therefore provide the highest sensitivity to the shear wave generated upon impact (Marchetti et.al, 2008).

Chapter 4

Digital Signal Analysis

This chapter will give a brief overview of digital signal analysis, and how analog signals are registered and transferred to digital information during data acquisition in the field. When measuring signal responses at different boreholes , the dynamic soil properties can be determined. Most important is the determination of the material damping and propagation velocity, and thus the small-strain stiffness (EPA, 2000). The soil properties may be determined using the time domain, or in the frequency domain which is more prevalent for digitised signals. In the time domain, the wave velocity is evaluated by looking at arrival times, and using the known distance. Damping may be calculated be examining the decay in amplitude between signals. The material damping is often very hard to determine in the time domain due to inhomogeneous effects corrupting the signals. In the frequency domain, the propagation velocity and material damping is determined from the phase difference between signals in the cross power spectrum. by using the phase difference the travel times may be calculated, knowing that a phase shift of 360 degrees constitutes one period (Hall & Bodare, 2000).

The determination of S-wave velocities can be improved by signal processing techniques, and with further work the damping ratios can also be estimated. When no permanent displacements occur in the soil, the response to a specific dynamic input load is primarily controlled by the small-strain shear modulus and the damping ratios of the soil being subjected to the load. At small strains the material properties behave nearly linear elastic, and thus, linear elastic stress-strain models can be utilised for wave propagation analysis associated with small strains (Hall Bodare, 2000).

The determination of shear wave velocity from field tests can be enhanced by using processing techniques such as the Fourier transformation algorithm. This will also enable relatively simple calculation of the damping ratio. The Fourier transforms allows for determination of the phase velocity and material damping by calculating the phase difference between the measurements of two receivers (geophones). By use of the Fourier transformation, one can transform the data from time domain to the frequency domain. measured velocity time history can be transformed into the frequency domain by utilising the discrete Fourier transformation, given by equation 4.1 (Hall & Bodare, 2000).

$$X(f_n) = \Delta t_s \sum_{k=0}^{N-1} [x(t_k)\cos(2\pi f_n t_k) - i x(t_k)\sin(2\pi f_n t_k)] = \Delta t_s \sum_{k=0}^{N-1} x(t_k) e^{-i2\pi f_n t_k} \tag{4.1}$$

Where f_n is the frequency in Hertz, t_k is the time. By establishing the formulation for radian frequency ω, equation 4.1 can be simplified. The radian frequency is given from 4.2

$$\omega = 2\pi f_n \tag{4.2}$$

By inserting for equation 4.2 in equation 4.1 one get a simplified expression for the Fourier transformation (Kulkarni, 2016), as seen from equation 4.3

$$X(\omega) = \Delta t_s \sum_{k=0}^{N-1} x(t_k) e^{(-i\omega t_k)} \tag{4.3}$$

4.1 Analog and Digital Signals

When the domain and range of a signal f(x) is modelled continuously, with the time coordinate x allowed to take on arbitrary values, the value of f(x) is also allowed to take on arbitrary values. Such a signal is called *Analog signal* (Kulkarni, 2016). Travel times for dynamic waves may be measured in the time domain, yielding analog signals. However, often it is more convenient to work with *digital signals*. Digital signals are signals with discrete domain and range. For accurate gathering of seismic data it is necessary to convert the initial signal to digital signal. This process of digitising the domain is called *sampling*, and allows for continously logging of data as digital values.

Chapter 5

The Flotten Test Site

To better understand the challenges for geotechnical engineers working with sensitive clays, The Norwegian Geotechnical Institute (NGI) partnered with the Norwegian University of Science and Technology (NTNU), SINTEFs Building and Infrastructure branch, the University Centre in Svalbard (UNIS), and the Norwegian Public Roads Administration (NPRA) established a national testing site for sensitive clays at Flotten, Tiller. The Flotten test site is one of the five test sites which constitute the national project termed *Norwegian GeoTest Site* (NGTS). The NGTS quick clay site at Flotten is aimed to gain further knowledge and find better approaches for sampling of undisturbed material and interpretation of in situ- and laboratory test data (L'Heureux et.al, 2019). The results from the NGTS quick clay site will help serve as guidelines for engineers to overcome the challenges related to working with sensitive clays. The information aquired from the NGTS project can help reduce the risk caused by climate change, extreme weather and landslides, as well as establish more sustainable and cost effective solutions for the construction, transportation and energy sector (NGI, n.d).

5.1 Location

The Flotten site is located approximately 20 km south of Trondheim city centre, Norway. The location is is given in figure 5.1, showing the site location relative to Trondheim city centre, and a zoomed in picture of the flotten site (Emdal, n.d).

As can be seen from figure 5.1 the test site is divided into two sections, where section A consists of grassy and open terrain, easily accessible. Section B lies within a vegetated bog, and re-

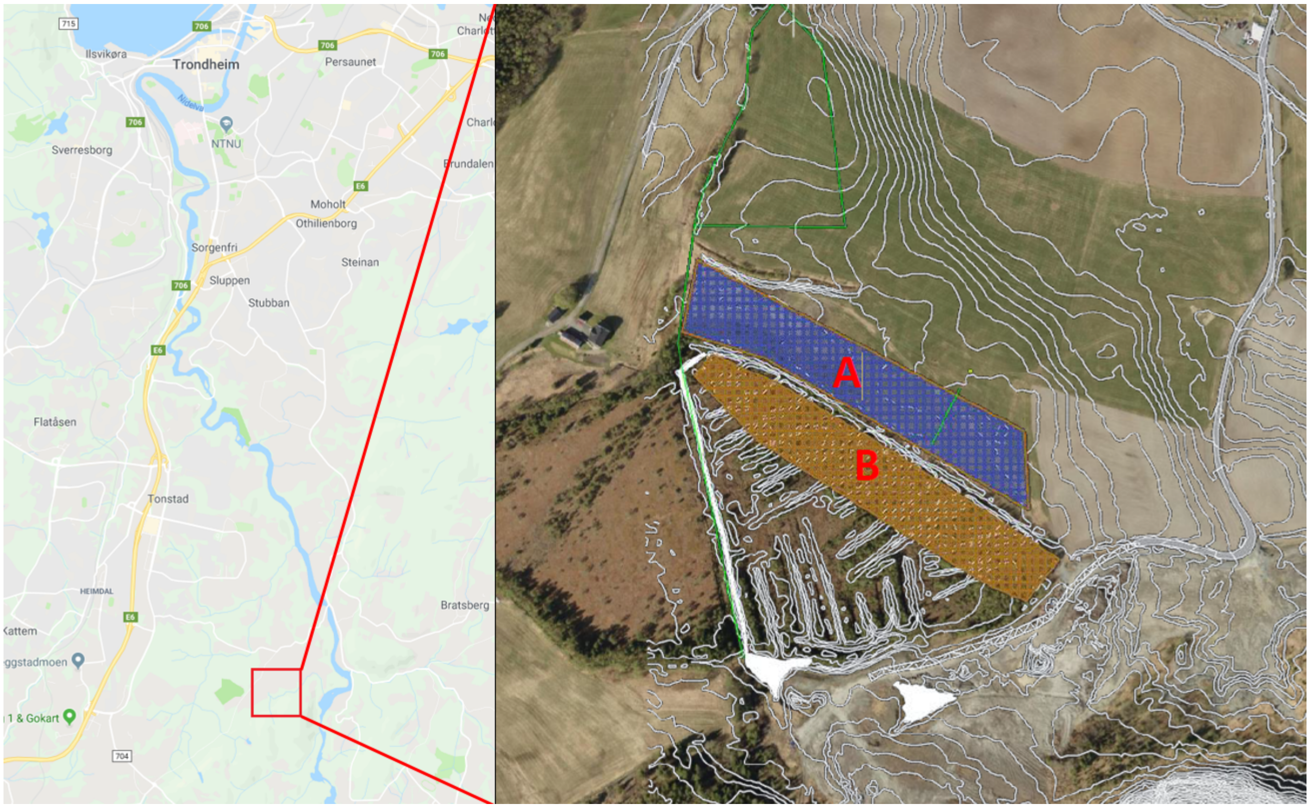

Figure 5.1: Location of the Flotten quick clay site, show by an overview map (Google Maps) to the left, and a site specific map to the right (Emdal, n.d).

quire further measures to be utilised as testing grounds. The site is located on relatively flat farm land, with ground level ranging from 125 m above sea level (masl) in the northwestern corner to +123 masl in the southeastern corner. The site drains towards the Nidelva river to the southeast at elevation approximately 72 masl. As a result of the receding ice sheet over this area during the last ice age, a basin was formed enabling deposits of glacial material. Deposits at the site consists of marine and glaciomarine sediments that emerged during post-glacial rebound and subsequent fall in relative sea-level (Emdal, n.d). For this thesis only the southeastern corner of section A has been investigated. The soil material at the site can be seen from the quaternary maps of the location, shown in figure 5.2. A quick clay hazard zone map (faresonekart) and risk map (risikokart) is given in figure 5.3. The figure shows that the southeastern corner of section A is within a a zone with high degree of quick clay hazard (www.ngu.no). By factoring in the consequences and damages of a potential slide, the site location has been given *risk class* 3 out of 5, since little infrastructure and few households would be affected in the occurrence of a slide. (NGU, n.d)

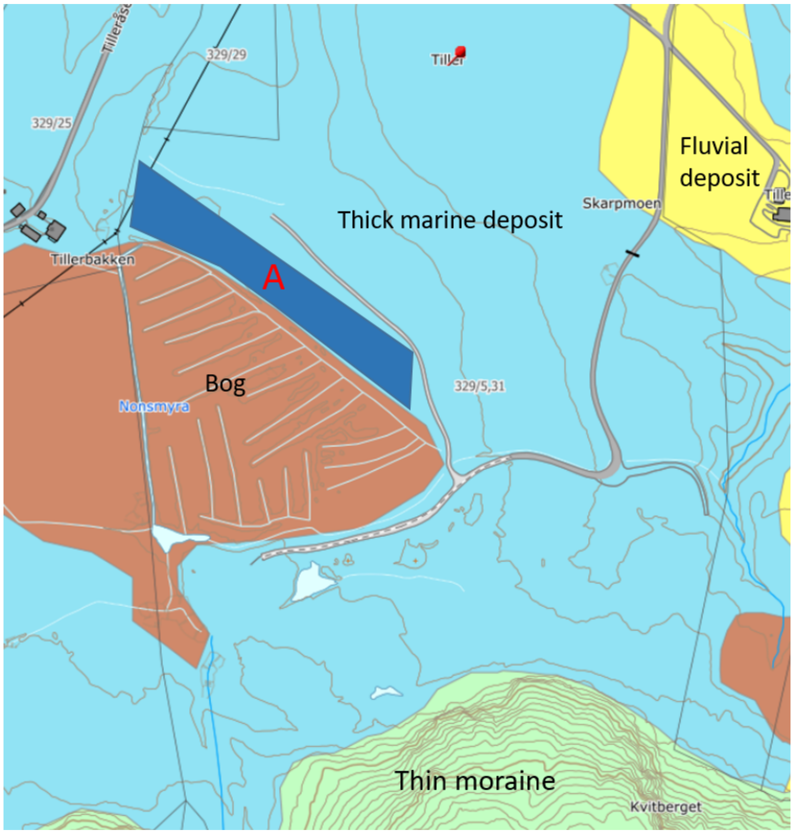

Figure 5.2: Location of Flotten site on a quaternary map (www.ngu.no).

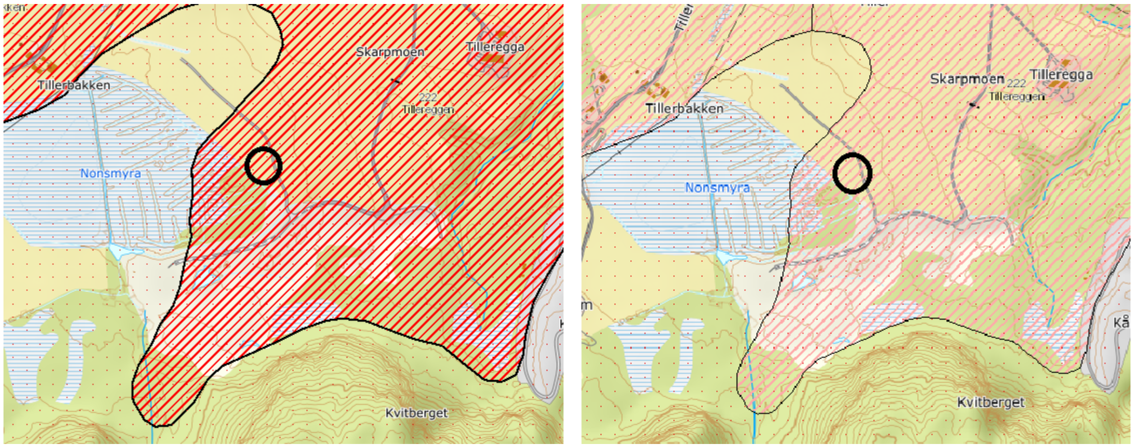

Figure 5.3: Left side: quick clay hazard map of the site location showing high degree of hazard for a quick clay event at the location (www.nve.no). Right side: Risk map indicating risk class 3.

5.2 Flotten Material

The test site is located on a marine clay deposit. A wide variety of laboratory and in-situ testing has been conducted on the Tiller site for investigation of its geotechnical, geophysical and geological properties. Results from previous field and lab investigations will be presented in this section.

The site consists of a 50 meters thick marine clay deposit. The top 8 meters show relatively low sensitivity, with the upper 2 meters being non-sensitive dry crust. A clay is classified as quick if the sensitivity, S_t is higher than 30 and the remoulded shear strength,s_r is less than 0.5 kPa (L'Heureux, 2012). On the site quick clay is characterised from 8 meters depth to 20 meters, with an accompanied increase in sensitivity to values around $S_t \sim 200$. (L'heureux et.al, 2019).

5.2.1 Field and Laboratory Tests

The geotechnical and geological properties on the site has been investigated from several different field investigation methods. Tests previously conducted include Cone Prenetration Tests wtih pore pressure measurements (CPTU), Cone Penetration Tests with resistivity sounding (RCPTU), Seismic Cone Penetration Testing (SCPTU), Total Pressure Soundings (TPS), Multi Spectral Analysis of Surface Waves (MASW), Electrical Resistivity Tomography (ERT), Seismic Dilatometer Tests (SDMT), piezometer tests as well as collection of undisturbed samples for laboratory testing (L'Heureux et.al, 2019)

Collected samples were sent to the laboratories of the Norwegian Geotechnical Institute (NGI), Geological Survey of Norway (NGU) and NTNU for identification, index testing and classification. Laboratory testing include grain size distribution, CAUC and CAUE triaxial tests, Constant rate of strain oedometer tests (CRS), Falling drop method, hydrometer method, direct simple shear tests (DSS), Bender element testing for unconfined measurements of shear wave velocity as well as confined shear wave velocity after consolidation to in sity stresses (L'heureux et.al, 2019).

5.2.2 Stratigraphy

Based on the findings from the field and laboratory investigations, the stratigraphy and soil layering has been divided in to three sections. The 2 meters thick top clay crust, consist of dry and weathered clay.the second clay section ranges from 2 meters depth to 19.5 meters. This unit show similar clay content and structure throughout, but differ drastically in sensitivity. From 2 meters to about 7.5 meters depth the clay exhibit low to medium sensitivity, while the bottom part from 7.5 meters to 19.5 meters show soil sensitivity values in the order of $S_t \sim 100$, meaning extremely sensitive clay. The third and last section below 19.5 meters depth consists of clay with several sandy layers, significantly lowering the sensitivity, and increasing the shear strength of the soil unit. This shift in layers at 19.5 meters below the surface has been speculated to be the boundary between marine and glaciomarine sedimentation during the Younger Dryas period, which marked the last decline in global temperatures in the last glaciation (L'Heureux et.al, 2019).

5.2.3 Index Properties

L'Heurex, Emdal & Lingård (2019) compiled the data and results from the different field and laboratory tests. The clay content for the soil deposit are in the range of 50-70 %. The water content is around 50 % at 5 meters depth in soil section with low to medium sensitivity. In the top part of the quick clay at 7.5 meters depth, the water content is approximately 45 % with values slightly decreasing towards 40 % at 20 meters depth. The unit weight, γ_t is around 18 kN/m^3 for the clay body. The identified Atterberg limits of the clay show that the water content is above the liquid limit w_l for the whole quick clay unit, while the plasticity index I_p varies between 8-18. The index properties plotted with depth presented by L'heureux et.al (2019) is presented in figure 5.4, along with sensitivity data. In the figure section two is divided two units, one for clay with low to medium sensitivity (IIa), and another for quick clay (IIb). Index testing has not been conducted for the third section below 20 meters depth.

5.2.4 Cone Penetration Test, CPTU

Results from cone penetration test with pore pressure measurements (CPTU) are included in figure 5.4. The results show clear indication of quick clay from about 7.5 meters depth, due to low cone resistance q_t accompanied by a substantial increase in normalised pore pressure u_2 (Pore pressure parameter, B_q). This is backed up by low undrained shear strength s_u and high sensitivity S_t.

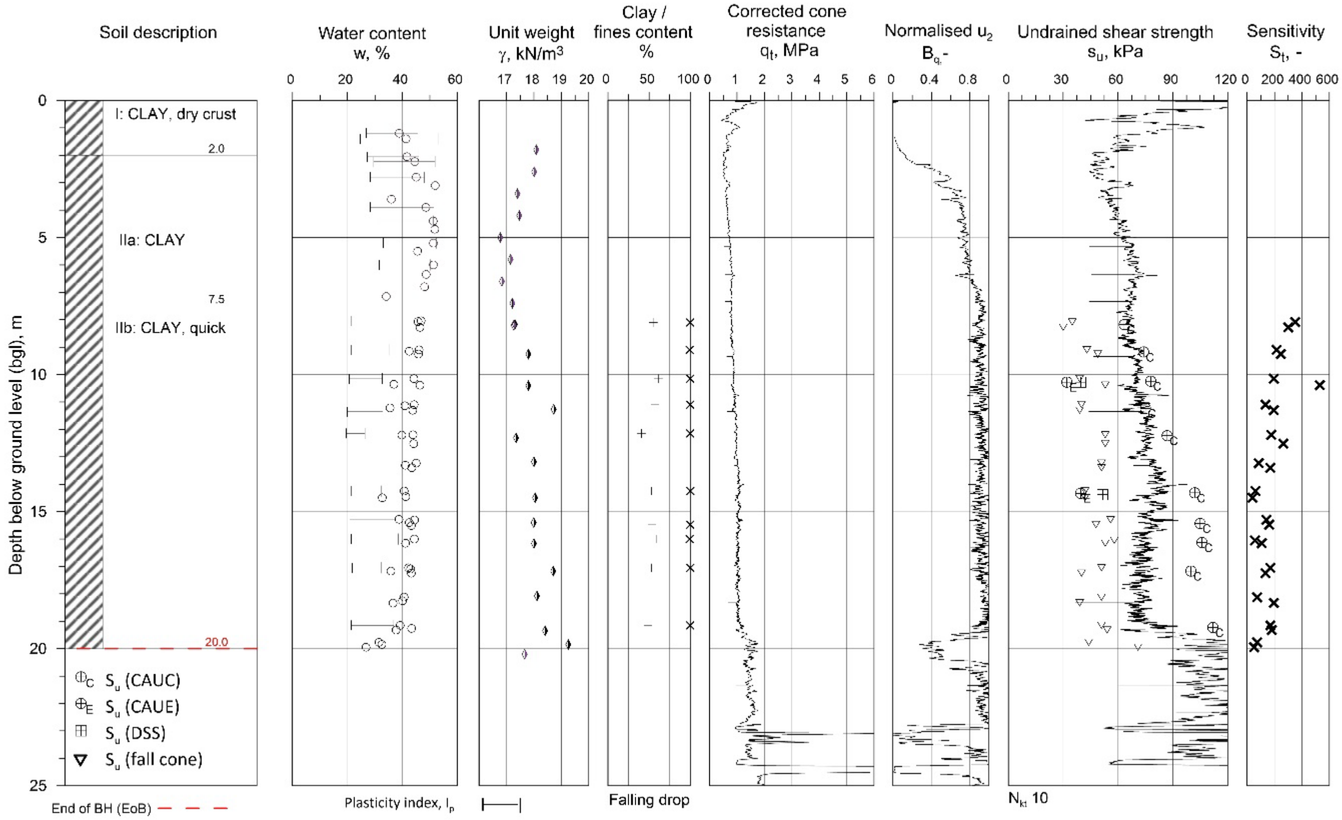

Figure 5.4: Soil profile at the test site, showing the identified material from laboratory tests on block samples and cone penetration test (CPTU) (L'Heureux et.al, 2019).

5.2.5 Undrained Shear Strength, s_u

Figure 5.4 show the results for undrained shear testing from triaxial tests; CAUc (anisotropic consolidation, undrained compression test), CAUe (anisotropic consolidation, undrained extension test), as well as DSS (direct simple shear test) and falling cone test. The strength of the clay increase in strength with depth until about 15 meters below surface. from 15 to 20 meters depth there is a slight decrease in strength. This strength anisotropy is linked to layering in the clay (L'Heureux et.al, 2019).

The remoulded shear strength, s_{ur} in the quick clay was found using the liquidity index of the clay. The plot of remoulded shear strength versus liquidity index is given in figure 5.6 (L'Heureux et.al, 2019). The figure show a majority of points plotted in the range of $s_{ur} \leq 0.5$, which is define the clay as quick.

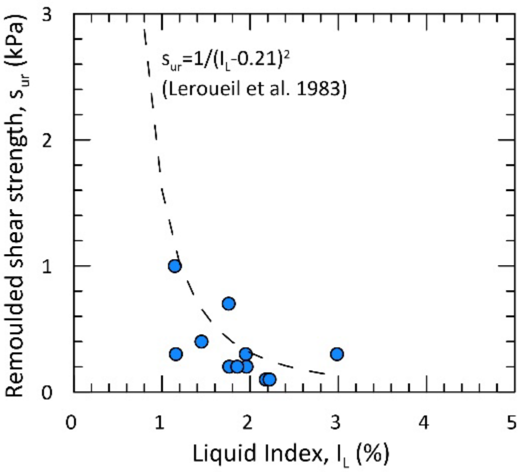

Figure 5.5: Remoulded undrained shear strength as a function of liquidity index, I_L for the quick clay section from 7.5 meters to 19.5 meters depth. The relationship used is given in the figure. (L'Heureux et.al, 2019).

5.2.6 Oedometer Testing

Results from 1D CRS oedometer testing suggest a preconsolidation stress of double the in situ vertical effective stress σ'_v, with an overconsolidation ratio (OCR) of 2.3 at 7 meters depth, and 1.7 at 19.5 meters depth. The clay is therefore significantly overconsolidated, which is as expected considering previous glacial history of large overburden due to the ice mass. The preconsolidation stress with depth is given from figure 5.6 (L'Heureux et.al, 2019).

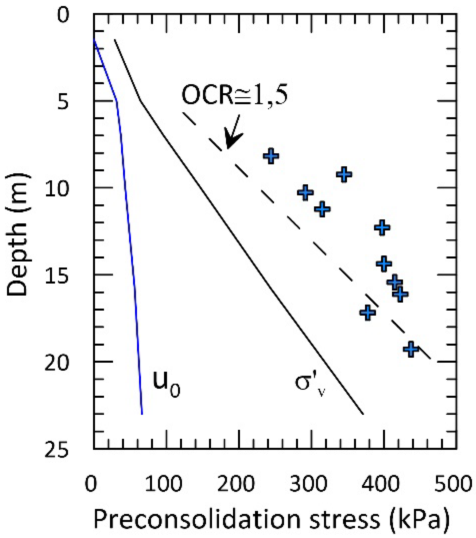

Figure 5.6: Preconsolidation stress versus depth, showing large degree of overconsolidation (L'Heureux et.al, 2019).

Chapter 6

Seismic Cross-Hole Test, Flotten

As part of this thesis, seismic cross-hole testing was conducted at the NGTS quick clay site at Flotten, for determination of G_{max}. The aim of the test is to check the viability and accuracy of the cross-hole test for determining shear wave velocities, and therefore the basis for determination of G_{max}. The gathered data and results are compared against results from previously performed field tests.

Equipment used in the cross-hole test is developed by NTNU for research purposes. The test performed in this study will therefore serve as valuable experience for further development of equipment and procedure. For a description of the seismic cross-hole method in general see section 3.3.1.

The cross-hole field test was conducted 24.05.2019 and 04.06.2019, Where the first day served as a test day, boring holes for source and receivers, as well as gathering first data at 2.5 m depth. On day two testing was done at 5 m depth, with updated software for better data aquisition. Participants for the field surway was Karl Ivar Volden Kvisvik, Espen Andersen, Per Asbjørn Østensen and myself, Marcus Hagen.

6.1 Equipment

The receiver tips for this setup are designed and prepared by Per Asbjørn Østensen. The receivers consist of an electrical accelerometer chip mounted to a conical plastic tip. The accelerometer is a sensor that measures the gravitational forces pulling on it in all three dimensions of the chip. The accelerometer is in principle a MEMS (Micro-Electro-Mechanical Systems) which can sense movement on a micro-scale. The MEMS device has two conductive plates that are electrically separated by a *combed finger arrangement*, as illustrated in figure 6.1.

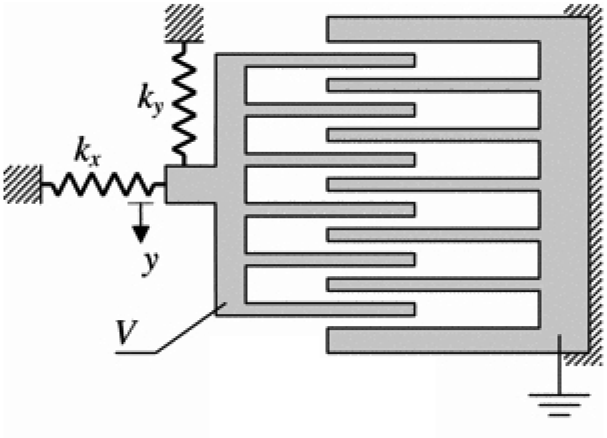

Figure 6.1: Illustration of a single sided combed finger arrangement (Elata Leus, 2005)

This structure consists of many parallel surfaces which form a capacitor. One of the conductive plates is attached to a small suspended mass, here indicated as springs on the left side in figure 6.1. As the suspended mass is subjected to vibrations the whole plate moves, shifting the distance between the combed finger arrangement. This movement in the structure leads to a change in capacitance, yielding a system that converts mechanical movement to electric signals. The accelerometer senses movements and converts the change in capacitance to useful voltages which can be logged over time (Loughborough University, 2002). Electrical chords from the receiver tip are led through plastic pipes that can be screwed to the tip, making it possible to penetrate the accelerometer to greater depths

At ground level the chords from both receivers are plugged to an analog-to-digital converter, which convert the electric signals to digital values. The converter is plugged to a computer, allowing the now digital signals to be logged. For measuring and storing the data, a program developed by Per Asbjørn Østensen using the LabView (National Instruments, n.d) is utilised. The accelerometer measures vibrations in X, Y and Z direction, and the specialised program logs the vibration in all three dimensions for both receivers. The program will record all vibrations over a span of one second, requiring the user to manually click at source impact. The program layout during testing will immediately show recorded results, allowing the user to control whether the impact was recorded or not. as seen by figure 6.2 show the layout of the software with only noise, giving response in X, Y and Z direction for both accelerometers. The red and yellow line with the highest amplitude are the response in y-direction, which corresponds to depth direction.

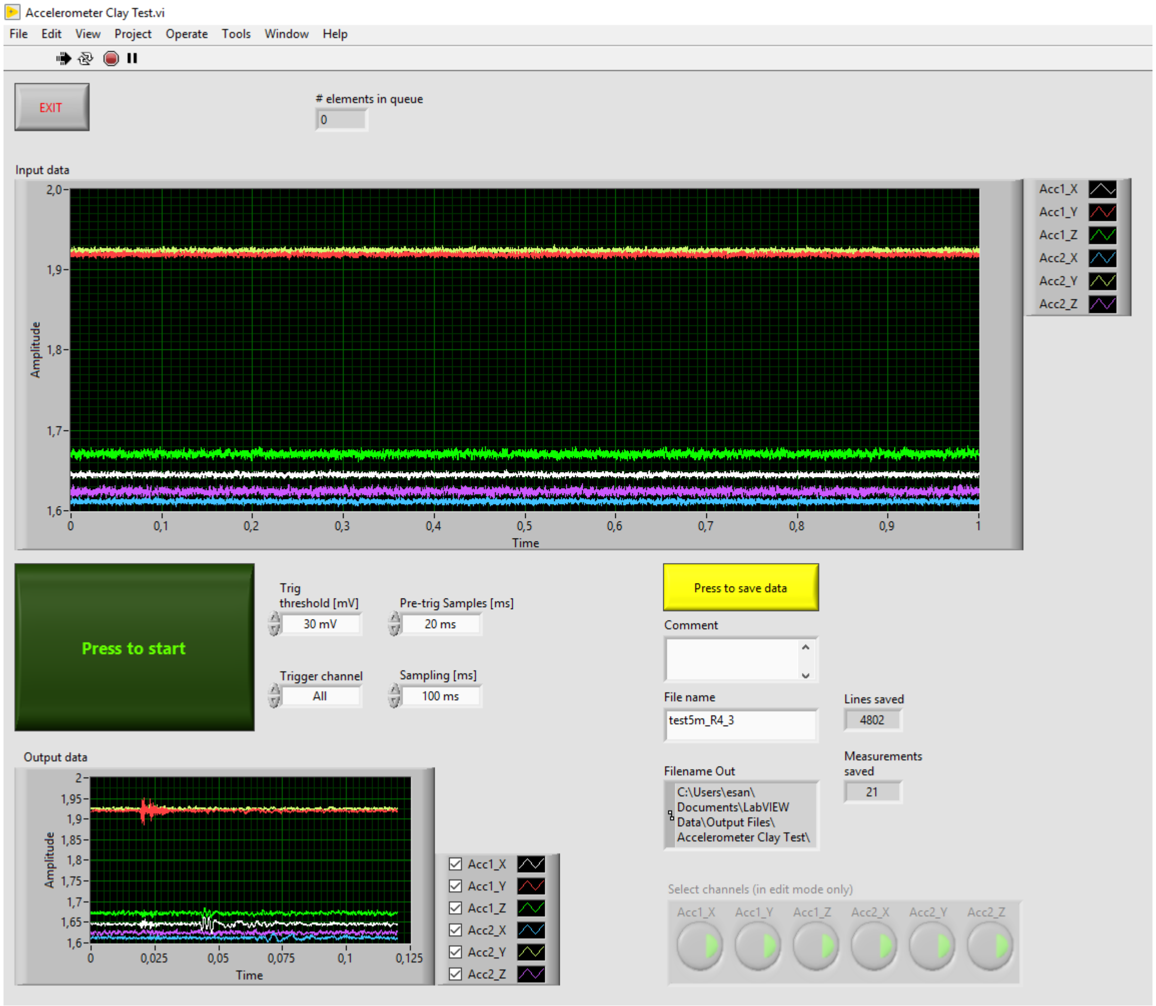

\# elements in queue: 0

Trig threshold [mV]: 30 mV

Pre-trig Samples [ms]: 20 ms

Trigger channel: All

Sampling [ms]: 100 ms

File name: test5m_R4_3

Lines saved: 4802

Filename Out: C:\Users\esan\Documents\LabVIEW Data\Output Files\Accelerometer Clay Test\

Measurements saved: 21

Figure 6.2: Layout of cross-hole test software. Programmed in LabView by Asbjørn Østensen.

A geotechnical drill rig with 76 mm diameter drill bit was used to bore holes for the accelerometers. The same drill bit was also used as impact source, striking a sledgehammer against it to generate seismic waves in the subsurface. Where penetration of receiver pipes proved difficult an auger was used to clear the path. A level was used to ensure sufficient verticality of the boring and piping, as well as to calculate the verticality offset.

6.2 Setup

The test was performed in the southeastern corner of section A on the Flotten site, as this area of the test site was optimal due to its flat terrain and accessibility to existing road. Two tests were conducted, one at 2.5 m depth, and at 5 m depth. A linear configuration with 4 m separation was chosen for this test, with 4 m from source to A1 and another 4m distance fro A1 to A2. The chosen setup and configuration is illustrated by figure 6.3

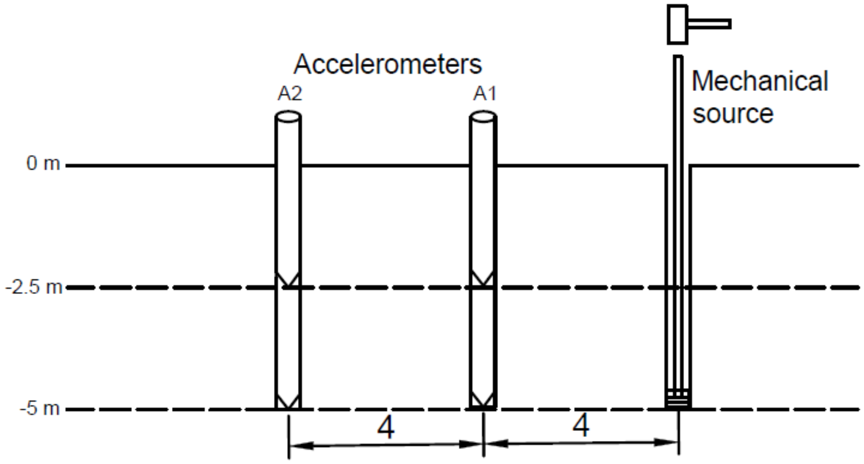

Figure 6.3: Illustration of the seismic cross-hole setup at depths of 2.5 m and 5m. A linear configuration was used with an equal separation of 4 m between all components, giving a distance of 4 m from source to receiver 1, and 8 m from source to receiver 2. The impact of a sledgehammer against a steel drill bit was used as source.

6.3 Procedure

6.3.1 Boring and Placing of Pipes

At the test site the first boring spot was chosen at random, at a flat and easily accessible lot of the southeast part of the NGTS section A. The borehole for accelerometer A2 was bored first using a 76 mm drillrod to 2.5 m depth. the drillrig was utilized for inserting and placing the receiver piping through the remoulded masses. The same procedure was applied for placing accelerometer

A1, but resulted in broken pipe transitions. A 76 mm auger was used to remove masses down to 2 m depth, making the hole open for easier implementation of receiver pipe while still allowing 0.5 m to fully penetrate the accelerometer into the soil. When continuing to 5 m depth the receiver piped was pressed using the drillrig, requiring no further preboring

6.3.2 Verticality check

Before any testing was conducted it was iportant to ensure that the piping was placed vertical. This is crucial to secure exact distances between source and receivers. As these distances have direct impact on the calculated shear wave velocities, it is important to control the alignment between accelerometers and source, and measure any discrepancies. Before any holes were bored the verticality was first controlled by holding a level against the drillrod and adjusting it to ensure optimal penetration angle, as shown by figure 6.4.

Since the the soft clay had been remoulded, the placing of receivers and their casing may lead to movement down-hole. After the pipes were successfully placed in their respective borehole, a second verticality check was applied. Assuming the casing is perfectly straight and rigid, not prone to any bending, a level was held up against the section of the pipe protruding above ground level. By holding the bottom end of the level to the base of the pipe and adjusting the level perfectly vertical, one can take measurements of the deviation at the top of the level. From the measured deviation, calculations were made to correct the distance between source and receivers. Only accelerometer A2 were found to have any deviations. The principle for the correction and calculations made for A2 are sketched in 6.5

Using simple geometry of the pipe section above ground level yielded an inclination of 0.955 degrees (θ), tilting the accelerometer casing down and away from the source. Assuming no bending of the pipe indicate that the accelerometer is displaced by 41.7 mm (x) away from the source, giving a new total distance of approximately 4.042 m from accelerometer A1 and 8.042 m from impact source. Due to the amount of piping placed in the ground is equal to 2.5 m, the tilted direction leads to the accelerometer tip being located above than the original 2.5 m. Because of the very small inclination this height difference is only 0.35 mm. This deviation in depth

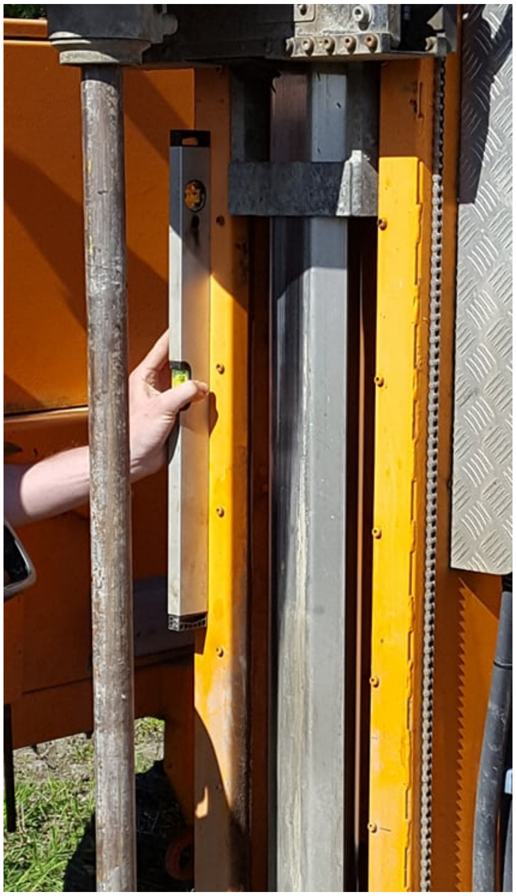

Figure 6.4: A level was used to check the verticality of the drillrod before boring.

is considered negligible, and for simplicity the depth to receiver A2 will remain the same. The piping consists of flexible plastic tubes, thus the inclination of the pipe above ground level may not reflect the actual movement in the subsurface. Verticality check from day two gave little to no inclination of piping above ground, which further strengthen the simplification made above. All distances between source and receivers, as well as depth is kept as illustrated on figure 6.3.

6.4 Generation and Registration of Seismic Waves

The 76 mm steel drill rod was used as impact source. As only the head of the rod is in direct contact with the surrounding soil, impact is assumed to cause seismic waves mainly at the desired depth. By striking the rod with a sledgehammer both vertically and horizontally one produces a variety of seismic signals with different wave fronts and polarity. A vertical strike was expected to give the best response at receivers A1 and A2, but by testing the response before recording

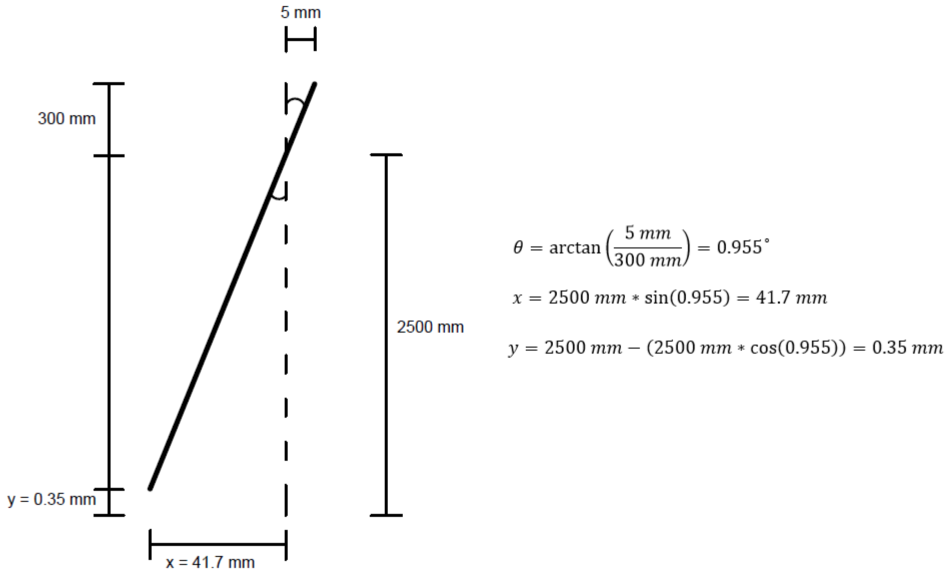

$$\theta = \arctan\left(\frac{5\ mm}{300\ mm}\right) = 0.955^{\circ}$$

$$x = 2500\ mm * \sin(0.955) = 41.7\ mm$$

$$y = 2500\ mm - (2500\ mm * \cos(0.955)) = 0.35\ mm$$

Figure 6.5: An exaggerated illustration of the pipe inclination and the following deviation from planned values at 2.5 m depth for accelerometer A2. The displacement of the pipe protruding above ground is used to estimate the offset from perfect verticality at the bottom of the borehole.

proved that horizontal strikes gave better results. From reviewing past work on cross-hole tests from the previous NGTS quick clay test site done by M. Knudsen (2014), combined with experimentation done on site, it proved necessary to conduct testing with horizontal impact as well as vertical impact. figure 6.6 show the setup for horizontal impact directions.

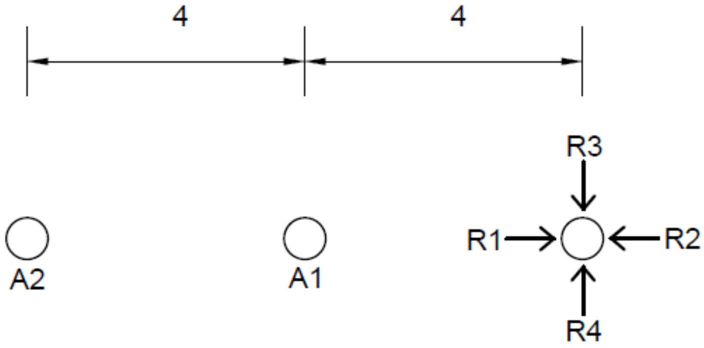

Figure 6.6: An illustration over the four different horizontal impact directions the cross-hole test was done for. As seen from above, looking down on the setup.

Chapter 7

Results

In this chapter the results from seismic cross-hole testing and seismic dilatometer testing will be presented. The results will be compared for 5 meters depth to check the compatibility of the two methods.

7.1 Cross-Hole Test

All plots of accelerometer findings are presented in Appendix C. An overview of the calculations done for finding G_{max} from the accelerometer time differences are given in figure C.29. The soil density used for calculation was $\rho = 1934 kN/m^3$, as this is the value found from previous tests at 5 m depth (NGI, 2017). The summary of the results from cross-hole testing is presented in tables below. Table 7.1 gives the interpreted shear wave velocity and small strain shear modulus from three tests for each horizontal direction. The directions R1, R2, R3 and R4 were given in figure 6.6. The tests with vertical impact are presented in table 7.2, with interpreted shear wave velocity and G_{max}. all results for v_s and G_{max} from cross-hole testing are summarised in table 7.3.

Plots from horizontal impact directions R3 and R4 gave warped readings and were hard to define the exact wave arrivals. interpretation of time difference between the two receivers proved difficult, and therefore only the two best plots were included. Received signals from source impact direction parallel to the accelerometers (R1 and R2) gave far better plots, and interpreted velocity values were more coherent. As can be seen from table 7.3 the results from impact directions R1 and R2 fits well with the results from vertical impact at source.

Table 7.1: Cross-hole results from 5 meters depth and horizontal impact

Impact direction	v_{s1} (m/s)	v_{s2} (m/s)	v_{s3} (m/s)	Var. coeff. (%)	v_s (m/s)	G_{max} (MPa)
R1	128.41	128.82	127.39	0.47	128.21	31.79
R2	129.55	129,76	128,72	0.39	129,35	32.36
R3	135.36	–	145.85	3.73	140.61	38.29
R4	156.86	–	155.79	2.55	156.33	47.26

Table 7.2: Cross-hole results from 5 meters depth and vertical impact

Impact direction	v_{s1} (m/s)	v_{s2} (m/s)	v_{s3} (m/s)	v_{s4} (m/s)	v_{s5} (m/s)	Var. coeff. (%)	v_s (m/s)	G_{max} (MPa)
Vertical	135.16	134.34	128.10	127.69	128.10	2.55	130.67	33.05

Table 7.3: Average cross-hole shear wave velocity and small strain shear modulus from all impact directions

Impact direction	v_s (m/s)	G_{max} (MPa)
R1	128.21	31.79
R2	129.35	32.36
R3	140.61	38.29
R4	156.33	47.26
V	130.67	33.05

Figure 7.1 and 7.2 show the results from a test with horizontal impact direction R1. from the plot in figure 7.1 one can see that the y-direction (depth direction) is the axis with the most clear response, while both x- and z-direction lack any defined wave motion. Figure 7.2 show a zoomed in plot of the response in y-direction, with black lines indicating the points for measurement of time difference between receivers A1 and A2. This time difference is the basis for calculating the shear wave velocity v_s, and therefore the small strain shear modulus G_{max}. Test results from direction R1 gave the best signal readings, and is could be considered being given a higher weight for evaluation of the G_{max}

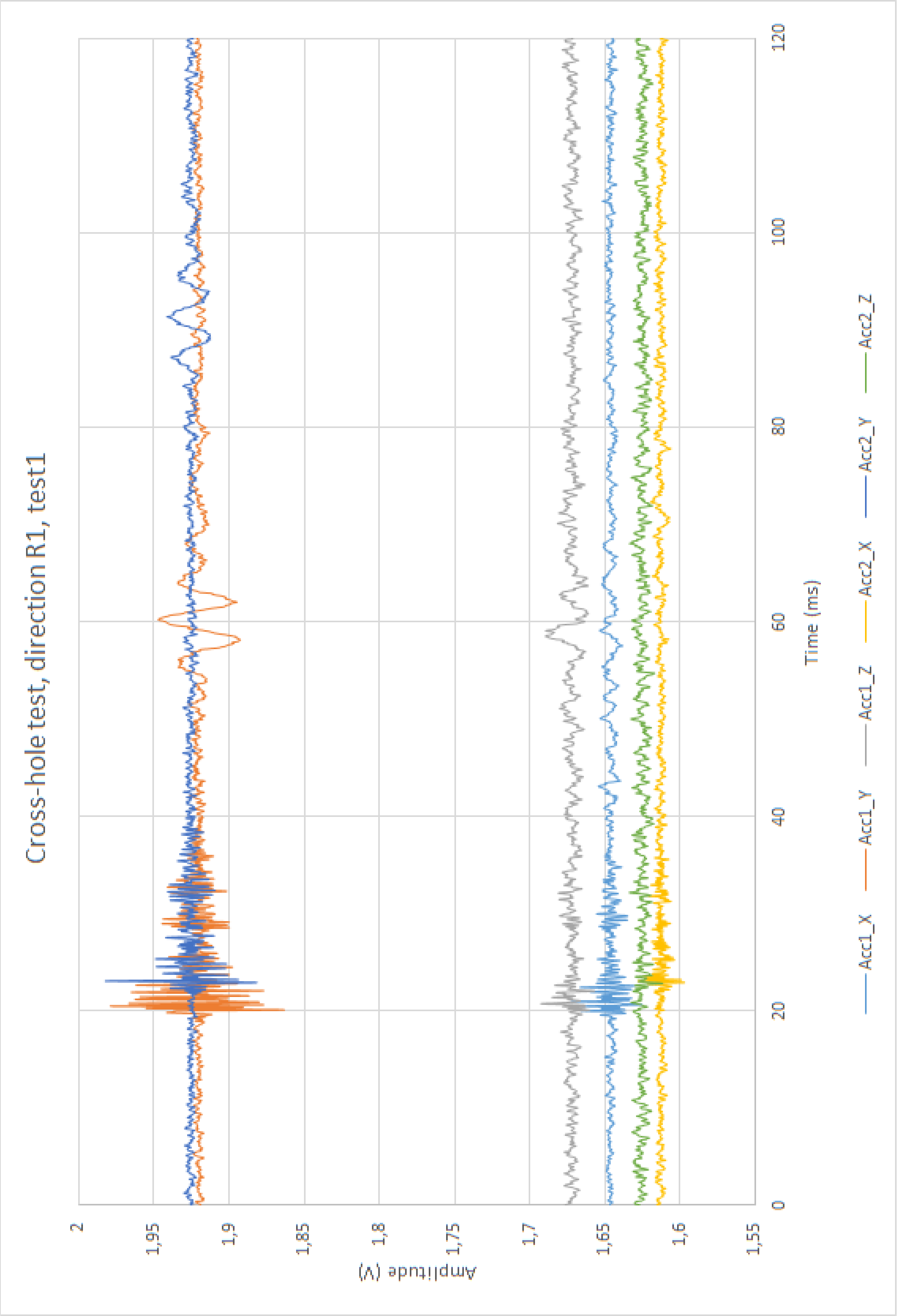

Figure 7.1: Total response curve from cross-hole test with horizontal impact direction R1, test 3. The curves constitute response in x-, y-, and z-direction for accelerometers A1 and A2. Testing conducted with automatic trigger, signals recorded are 20ms before and 100 ms after first impact using a 30 mV trigger threshold.

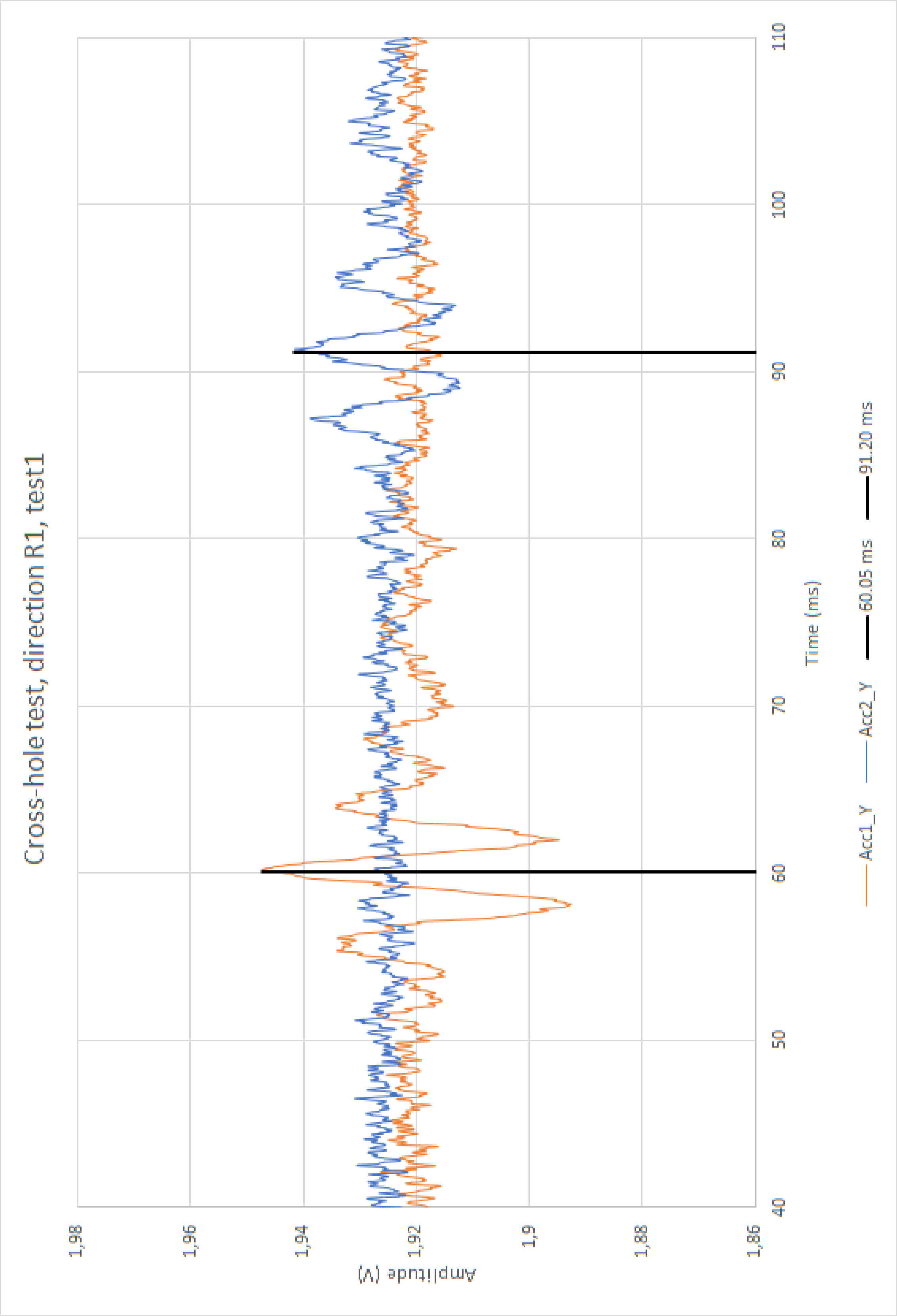

Figure 7.2: Cross-hole test with horizontal impact direction R1, test 3. close-up of response in y-direction for determination of shear wave velocity, v_s. Orange curve is for signals received by A1, while the blue curve is by A2. Black lines mark equivalent points, used for determination of time difference between A1 and A2.

7.2 Seismic Dilatometer

Data from previously conducted SDMT testing at the same location on Flotten was revisited to compare its results to those found by cross-hole testing. The SDMT test was done to 20 meters depth, at the same location as the cross-hole test. three shear wave velocity measurements was done for every 0.5 m. The calculation data for the SDMT is given in Appendix D. A full plot of estimated G_{max} with depth is given in figure 7.3, where each data point is the average value of the three measurements. The results for 5 meters depth is presented in table 7.4, including the three separate shear wave velocity measurements. Judging by v_1, v_2 and v_3, there is considerable scatter in the values, given a high coefficient of variation (σ/μ). The evaluated G_{max} value of 28.79 is therefore quite uncertain.

Table 7.4: Results from seismic dilatometer testing at 5m depth

v_{s1} (m/s)	v_{s2} (m/s)	v_{s3} (m/s)	Var. coeff. (%)	v_s (m/s)	G_{max} (MPa)
127	104	134	10.51	122	28.79

The results from cross-hole testing at 5 m depth is also included in figure 7.3, showing that the most accurate data from vertical impact direction, and horizontal impact directions R1 and R2 seem relatively consistent with the G_{max} from SDMT. Just looking at the trend of the SDMT results (light blue) may give the impression that the determined value for $G_{max} = 28.79$ at 5 m depth could be wrong. The SDMT value at 5 m is not consistent with the values 0.5 m above and below. This combined with the large deviation in shear wave velocities seen in table 7.4 could indicate that the measurement at 5 m should be ignored. This statement is backed up by MASW results from the flotten site, given in figure 7.4 together with the SDMT (L'Heureux, 2019). However, the data from cross-hole testing seem to back up this sharp decline in G_{max} at this depth, even though the cross-hole results give somewhat higher stiffness.

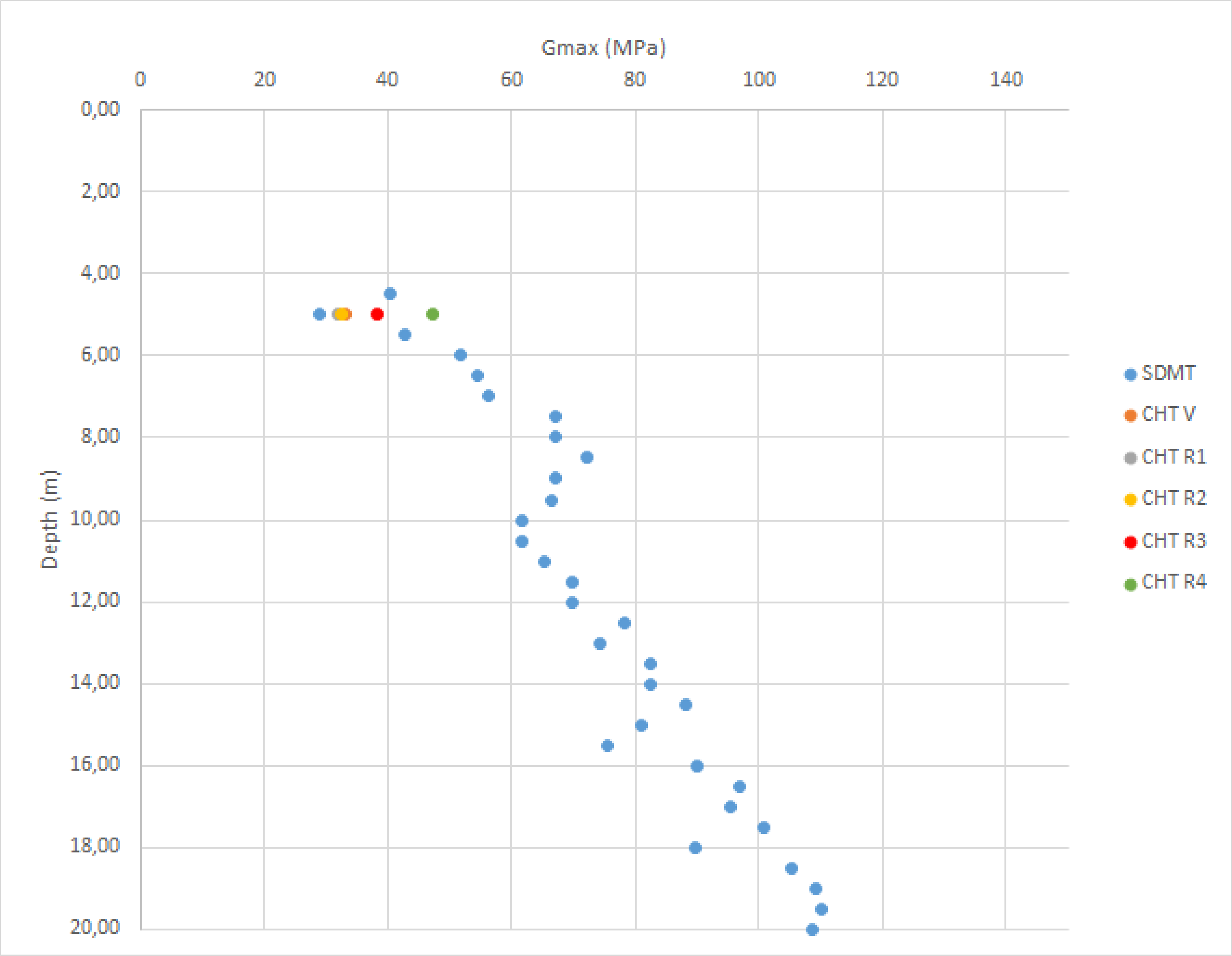

Figure 7.3: G_{max} from SDMT plotted against depth for the Flotten test site. Results from cross-hole testing at 5 m depth is included (NGU, 2017)

7.3 Summary of the Results

The results for G_{max} at 5 m depth is summarised in table 7.5.

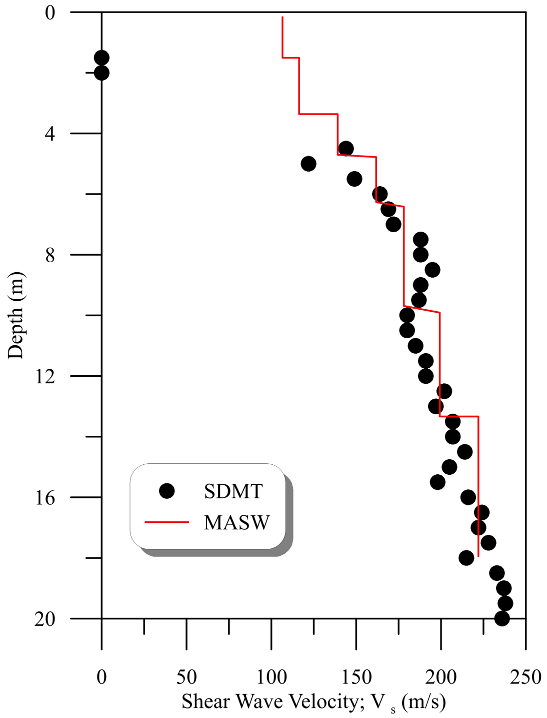

Figure 7.4: v_s from SDMT and MASW plotted against depth for the Flotten test site (L'Heureux, 2019)

Table 7.5: Average cross-hole shear wave velocity and small strain shear modulus from all impact directions

Method	v_s (m/s)	G_{max} (MPa)
CHT R1	128.21	31.79
CHT R2	129.35	32.36
CHT R3	140.61	38.29
CHT R4	156.33	47.26
CHT V	130.67	33.05
SDMT	122.00	28.79
MASW	~ 160	~ 49.5

Chapter 8

Discussion

This chapter consist of a discussion of the cross-hole test conducted on the Flotten test site. Sources of error during testing and data interpretation will be presented and discussed. The results will be compared to characteristic values, and the viability of the cross-hole method versus the Seismic dilatometer will be discussed.

8.1 Sources of Error

8.1.1 Cross-hole setup

During implementation of cross-hole setup during day one, borehole A2 was first predrilled to 2.5 m depth, while borehole A1 was augered to 2 m depth and the pipe was pressed to the final 2.5 m depth. On day two, both accelerometer pipes were pressed to the final depth of 5 m. This means that accelerometer A1 has an open borehole to 2 m depth, then the last 3 m the pipe is fully embedded in the soil. Meanwhile the pipe for accelerometer A2 is placed soil with the top 2.5 m being fully remoulded, and pressed through the last 2.5 m. The implications of this variation in penetration method may lead to differences in how the source impact is travelling down-hole, and how much the surrounding soil contributes in attenuating the signal.

As mentioned in section 6.3.2, the verticality may be a significant source of error. The verticality of the pipes were checked both test days, and proved that the section above ground level was close to perfectly straight. The verticality was checked with a lever both before predrilling the holes, as well as after placing the pipes. However, as the pipes were pressed to higher depths, there is no way to adequately check that the pipe stays perfectly straight. As the tubing consist of PVC plastic, the high flexibility could have made the tube go off course as pressure was applied at ground level. a displacement of pipes in the subsurface would lead to deviations in both vertical direction as well as horizontal directions. Due to this uncertainty, the distances used for calculations were kept at the original values; 4 m between receivers and source, and final depth of 5m as shown in figure 6.3. This is a fair assumption given the uncertainties mentioned. Since both receiver holes were verticality checked during predrilling, one could assume the pipe stays approximately vertical at least for the first 2 - 2.5 m. By penetrating the pipes to larger depth, the pipes may stay on the predetermined course, which could lead to good verticality. nonetheless, this aspect is a significant source of error, and may lead to especially large deviations if the receiver pipes have opposite inclinations. Under section 6.3.2, figure 6.5 show how the displacement was first determined. Using this method, only a very small displacement would exist at the final depth, assuming the pipes were kept perfectly linear. The method used for measuring this displacement at the top was done with a measuring tape and a hand-held level, which give rise to more uncertainty due to error in measuring and reading of values. The initial measuring and marking of the borehole location was also done using a measuring tape. The distance of 4 m between source and receivers should ideally be placed in a perfectly straight line for optimal accuracy during surveying. The linear configuration was measured and checked using eyesight of the field participants. Inherent human error is therefore also a source of error during setup.

A 76 mm diameter drillrod penetrated to the desired depth was used as basis for the seismic source. The impact of a sledgehammer against the drillrod was done to generate seismic energy. A rod with a circular cross section is sufficient for vertical impact. As it was decided to conduct tests with horizontal impact direction some sources of error arise. There may be large variations in the impact directions, and what angle the sledgehammer hits the steel rod. This may give smaller variations in the response at the receivers. a steel rod with quadratic cross-section may have made horizontal impact more consistent.

8.1.2 Accelerometers and software

Before recording any signal response, the accelerometers were checked by striking the receiver tubes, as well as by jumping on the ground surrounding the setup. This check yielded satisfactory response. During day one of testing, the software required manually timing and activating the recording. For the second field day, the software was updated to automatically trigger the recording as long as the first wave arrival reached a set amplitude. For vertical strikes the software could easily record and register the signals. During horizontal testing the threshold value had to be lowered. Especially for horizontal impact normal to the receiver direction (R3 and R4), the threshold value for triggering the software had to be reduced even more. Since the signal is smaller for horizontal impact, the impact of noise becomes more prominent.

Interpretation of the data showed that horizontal impact parallel (R1 and R2) to the receivers gave the most clear response in y-direction (depth direction). Vertical impact also gave clearest response in y-direction. However, horizontal impact normal to receiver setup (R3 and R4) gave little to no response in y-direction, but instead the dominating response was in x-direction. Comparing the response of the different impact directions, proved a much clearer sinusoidal fluctuations in directions R1 and R2. Vertical impact was expected to give the best response, but yielded less clear fluctuations than those of R1 and R2. This may be due to attenuation effects from the piping. Since the the accelerometers are placed inside inside the pipes, this could lead to undesirable effects. A setup with the possibility to loosen the receiver tip from the rest of the piping, may give better signal-to-noise ratio and enable higher quality data acquisition.

8.1.3 Determination of Shear Wave Arrival Times

The only parameters needed to calculate the shear wave velocity v_s, is the time difference between wave arrivals at the receivers and the distance between them. Since both of these inputs are associated with much uncertainty, the estimates of v_s is highly sensitive to any errors in distance and determined arrival times. As already mentioned, the distance has several potential sources of error.

The shear wave arrival time was determined by manually inspecting the response curve. By subjective interpretation the arrival time or corresponding points between receivers A1 and A2 was determined. All response plots, with corresponding points determined are given in Appendix C. For the majority of plots, the determination of corresponding points were difficult. For several tests, the response curve showed little to no clear arrival, with skewed and uneven response. Many tests gave response curves with different frequencies between A1 and A2, making both arrival time and corresponding points hard to evaluate. The plots of A1, the receiver closest to the source generally gave a more evident response. Receiver A2, placed 8 m from the source were more disturbed by noise, and yielded output with lower amplitude and frequency. These findings could be an indication that the chosen receiver distance was too long.

The use of corresponding points may give variations in time difference, depending on the point chosen. This method for determining the time difference can therefore produce error in the final estimate. The most viable option for good consistency is by using the first point of wave arrival. Using first response eliminate the error from different frequencies in the response from A1 and A2. However, many of the response plots had so low signal-to-noise ratios, that it was difficult to identify first wave arrival. Due to this, many of the tests were analysed using corresponding points such as maximum and minimum points. This is a clear weakness for many of the test results.

8.1.4 Assumptions of the Cross-hole Method

The principle of the cross-hole method assumes that the impact at the source generate vibrations travelling in a horizontal path from the source rod to the accelerometer at the same depth. For the determination of v_s in this thesis, horizontal wave propagation at 5 meters depth is assumed. In reality, the impact of a sledgehammer will generate both P- and S-waves in the soil, propagating in all directions with a wave front shaped as a hemisphere. The direction the hemisphere is facing is decided by the impact direction of the hammer blow. When the rod is stricken by a hammer, the rod deforms and cause vibrations along the full length, deforming the surrounding soil. Since the wave propagation velocity of the steel rod ($\sim 3250m/s)ismuchhigherthanthesoil,t$

This aspect is particularily important for the tests conducted on the Flotten site. The cross-hole setup used for this thesis utilises a drillbit directly as a source, with no casing surrounding it. As suggested by Hall Bodare (2000), a protective casing on the outside of the steel rod would help eliminate the disturbance from other wave types, giving a much clearer response. The setup used at Flotten induce a variaty of waves in the subsurface, clouding the response. It is therefore impossible to assess whether the exact wave paths that reached the receivers. This may

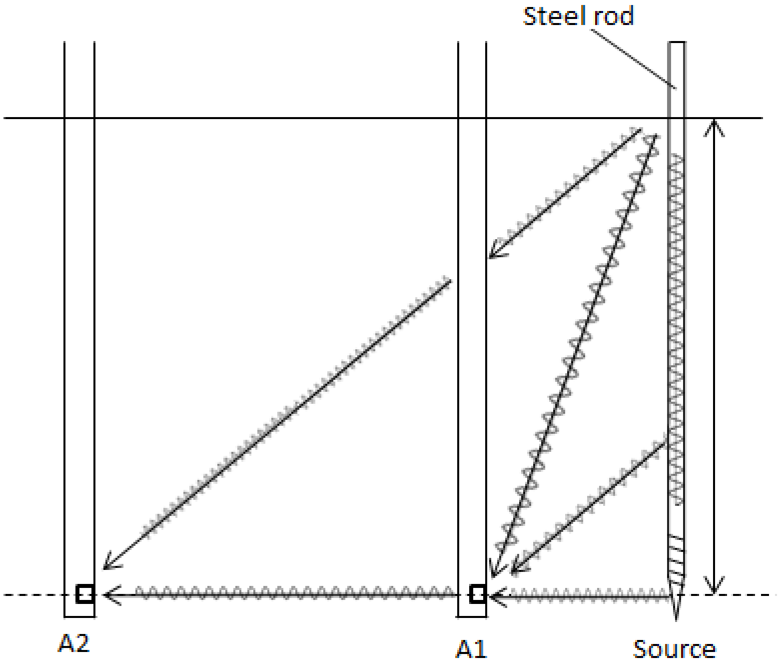

Figure 8.1: Illustration showing that body waves travelling with a hemispherical wavefront will reach the receivers with different directions, disturbing the signal of interest durig cross-hole testing (modified image from Knudsen, 2014).

be one of the main reasons why acquired data showed heavy influence of noise, and disturbed response. The assumption of perfectly horizontally traversing shear waves is a source of error, and may lead to lower accuracy in the estimated v_s and G_{max} values.

8.2 Analysis of Shear Wave Velocities

In this section the results from cross-hole tests will be discussed. two tests with vertical impact, and two tests of each horizontal impact direction is included in Appendix C.

8.2.1 method for Determination of Shear Wave velocities

As previously mentioned, assessment of time difference between received signals at accelerometers A1 and A1 was evaluated subjectively. By personally finding the most promising points on curves corresponding to the same response, this section will showcase the method used, and the difficulties associated with it.

Vertical Impact

The tests conducted with a vertical impact on the source, gave highly disturbed response plots, with no smooth sinus curves. This can be seen from figure 8.2. All tests with vertical impact showed this chaotic behaviour, making it difficult to pinpoint the exact wave arrival. one can see the wave arrival from the top plot, but when zooming in there is no clearly defined wave arrival. For all tests with vertical impact a method of corresponding points were used. For this test a center line was added to better visualise the major fluctuations in amplitude. The initial assumption for finding corresponding points was to output the minimum and maximum points of the curves. These points were easy to identify, but the time difference between minimum points and maximum points did not always yield the same time difference. Determination of corresponding points were therefore a combination of evaluating max/min values, as well as inspecting the response curves, making sure the curve made corresponding fluctuations around the chosen point.

Horizontal Impact

The cross-hole tests with horizontal impact gave the most promising response diagrams for impact directions R1 and R2, which are parallel to the test configuration. The most clear wave response was given by tests in direction R1, which corresponds to striking the source in a direction away from the receivers. This may be due to less disturbance from other wave forms. From figure 8.3 one can see a significant improvement in the response, compared to the tests with vertical impact. For this test the maximum wave peak was used as a corresponding point.

Polarity

One of the main interests of conducting horizontal impact tests was to use the plots from opposite impact directions for determination of time difference. Hammer blows from opposite sides should produce waves with inverted signal curve. Due to large differences in the response plots, this was not possible. Figure 8.4 show response plots in x-direction from test R3 and R4. These tests were done striking the sledgehammer horizontally on the rod normal to the direction of the receivers. The figure show a clear shift in polarity, especially at receiver A2. However, the plots are not good enough for detailed determination of time difference.

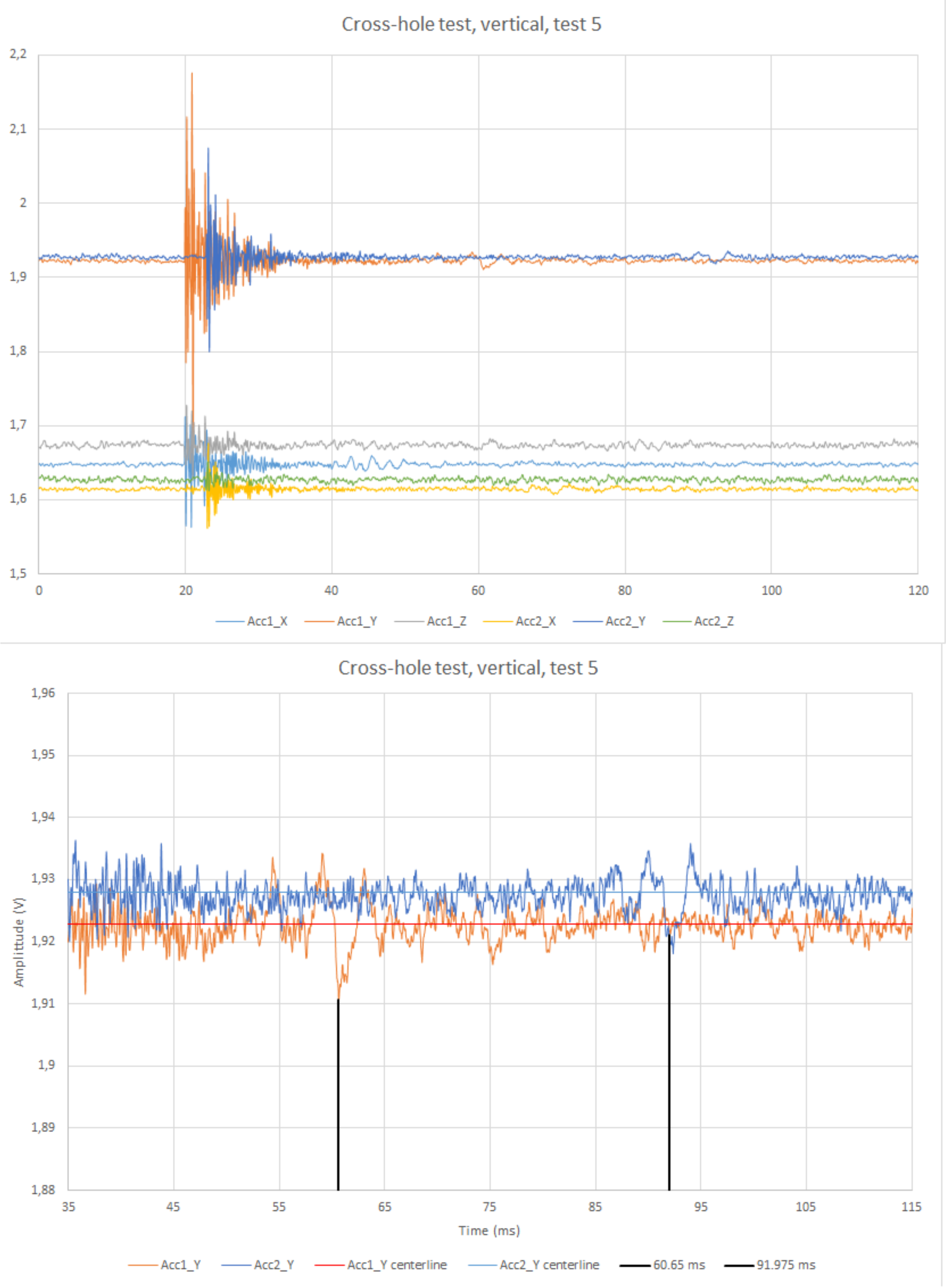

Figure 8.2: Cross-hole test from Flotten, Vertical impact test number 5.

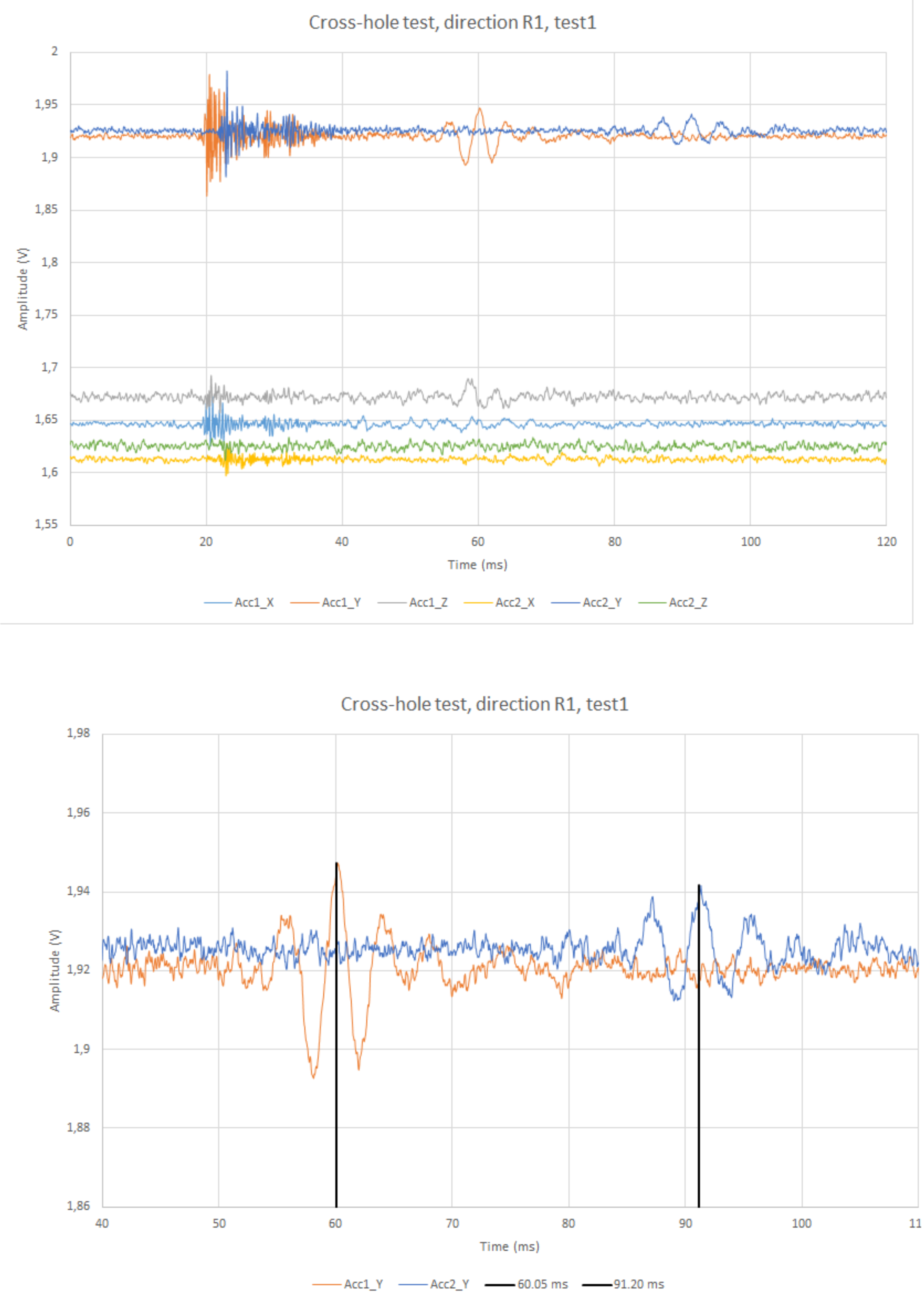

Figure 8.3: Cross-hole test from Flotten, Horizontal impact direction, test number 1.

Figure 8.4: Test for using polarity for determination of time difference between signals at receivers A1 and A2.

8.2.2 Characteristic v_s values

The shear wave velocity values determined in this thesis is summarised in table 7.5. The values determined from cross-hole testing show large variance. Particularly values from horizontal impact directions R3 and R4 differ significantly from the results of vertical impact and horizontal impact directions R1 and R2. All v_s values determined in this thesis are in the ranges 128 m/s to 160 m/s. Characteristic shear wave velocity values for Norwegian soft clays are in the range $100m/s \leq v_s \leq 300m/s$ (Long & Donohue, 2007). The results from Flotten is therefore in the expected range. A study by L'Heureux & Long (2016) collected data from 29 sites in norway, 13 of which from mid-norway. This study show that the majority of v_s data for Trondheim clays are in the range of 100 to 200 m/s. Values are typically 100 m/s in soil near surface level and increase to about 200 m/s at 12 m depth. A plot of in situ shear wave velocities for sites in the Trondheim region is given in figure 8.5 (L'Heureux & Long, 2016). The values found in this thesis are a good fit given the characteristic values for Trondheim clays.

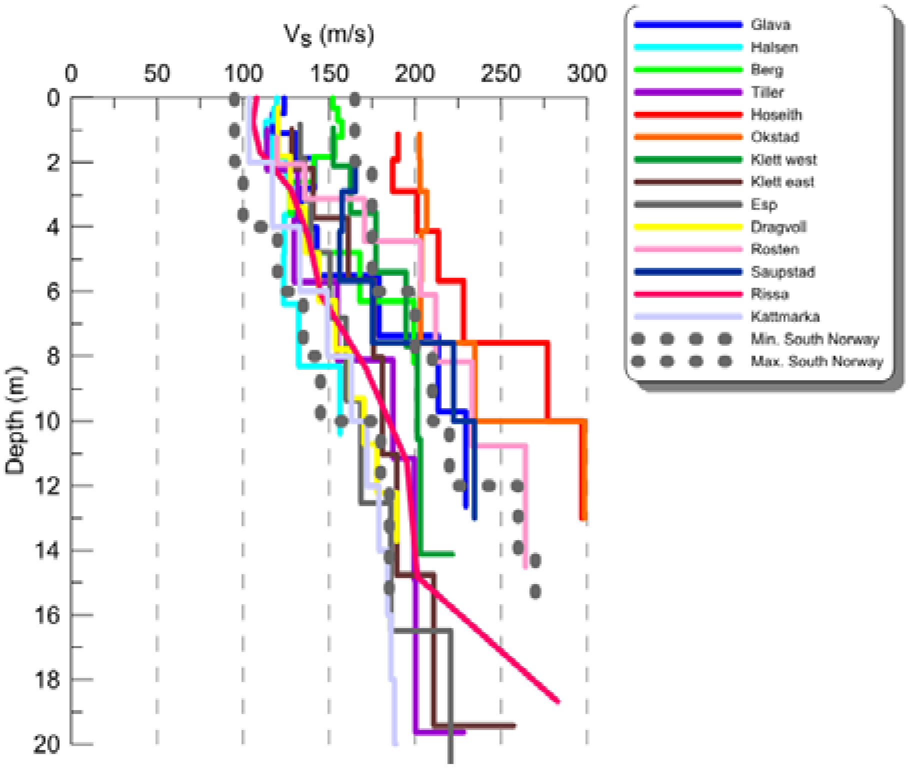

Figure 8.5: In situ shear wave velocity profile for sites in the Trondheim area. Purple line is for the previous NGTS site at Tiller (L'Heureux & Long, 2016)

8.3 Comparison of Cross-Hole and Seismic Dilatometer Test

The results of the cross-hole test at 5 m depth supports the low value given by the SDMT method at the same depth. Large scatter in the three recorded SDMT shear wave velocities, resulted in a relatively low v_s value compared to the higher values directly above and below. However, the results from Cross-hole tests with vertical impact and Horizontal impact R1 and R2 give values in the same order, as summarised in table 7.5. The cross-hole test in this thesis is only comprised of one depth, due to equipment restrictions. It is therefore not sufficient data to conclusively compare the cross-hole test to the seismic dilatometer. But based on the test done at 5 m depth, it seems to be good compatibility between the two. Based on previously conducted

MASW measurements on site, both the Cross-hole and SDMT method give significantly lower values at 5 m depth, but seem to agree well with the SDMT with larger depths (Figure 7.4).

Chapter 9

Conclusion

9.1 Summary

Both cross-hole testing and seismic dilatometer has been evaluated during this thesis. The two methods show comparable results, yielding v_s and G_{max} values of the same magnitude for the tested depth.

Cross-hole testing at 5 m depth at the NGTS test site at Flotten gave G_{max} values in the order of 31 to 33 MPa from Testing with vertical impact and horizontal impact parallel to receiver setup. Testing with impact normal to receiver direction gave G_{max} results much higher, with direction R4 as high as 47 MPa. Due to the low quality of these tests, the lower values have been given higher credibility.

The Seismic Dilatometer yielded an uncertain G_{max} value of 28 MPa, due to large scatter in the estimated shear wave velocities. Due to difficulties interpreting the cross-hole data, one can not fully confirm the validity of this relatively low value. Previously conducted MASW tests and SDMT show much higher shear wave velocity values in the soil above and below the tested depth of 5 meter. Generally all recorded values are within the typical characteristic shear wave velocity of Trondheim clays.

9.2 Further Work

The major weakness of this thesis is the lack of deeper cross-hole data. For further studies, it is recommended to produce and update the cross-hole equipment to combat the sources of error in this thesis. By using a square rod protected in a casing, the generated seismic signal will be allowed to mainly travel horizontally from source to receiver, without being heavily disturbed. A receiver system that allows for separating the accelerometer tip from the rest of the pipes, will eliminate unwanted attenuation in the pipe. Such a system could help increase signal-to-noise ratio, and yield better response in all three coordinates. Decreasing the distance from source to receivers can also help make the receiver response more coherent, achieving similar frequencies which will make analysis easier. By acquiring more robust equipment, deeper surveying can be achieved, which allows for better comparison to other in situ seismic surveying.

Bibliography

[1] ATKINSON, J. H. (2000) *Non-linear Soil Stiffness in Routing Design*, Géotechnique, 50(5), pages 487-508.

[2] BENZ, T. (2007) *Small-Strain Stiffness of Soils and its Numerical Consequences*, Institute for Geotechnics, University of Stuttgart.

[3] Britannica Encyclopædia (n.d.) *Diagenesis*, <https://www.britannica.com/science/diagenesis. Accessed 12.05.2019.

[4] CAMPANELLA, R., STEWART, W. (1992) *Seismic Cone Analysis using Digital Signal Processing for Dynamic Site Characterization*, Canadian Geotechnical Journal, Vol. 29, Issue 3, pages 477-486.

[5] CHIANG, D.-Y. (1999) *The Generalized Masing Models for Detoriating Hysteresis and Cyclic Plasticity*, Applied Mathematical Modelling, Vol. 23, pages 847-863.

[6] CHOPRA, A. K. (2012) *Dynamics of Structures, Theory and Applications to Earthquake Engineering 4th Edition*, Pearson Education Inc., Prentice Hall, USA.

[7] Dakota Ultrasonics (n.d) *Shear wave velocity table*, [Internet], <https://dakotaultrasonics.com/reference/>, accessed 20.05.2019.

[8] Elata, D., Leus, V. (2005) *How Slender can Comb-Drive Fingers be*, Journal of Micromechanics and Microengineering, Vol. 15, Number 5.

[9] Emdal, A. (n.d) *Kvikkleirefeltet på Tiller-Flotten* [Powerpoint presentation], <https://www.vegvesen.no/_attachment/2052549/binary/1215411?fast_title=Kvikkleirefeltet+p%C3%A5+Tiller-Flotten.pdf>, accessed 18.05.2019.

[10] EPA: U.S Environmental Protection Acency (2016) *General crosshole procedures*, <https://archive.epa.gov/esd/archive-geophysics/web/html/general_crosshole_procedures.html, accessed 30.02.2019

[11] FROST, D. J., BURNS, S. E. (2003) *The Civil Engineering Handbook, 2nd edition*, CRC Press, LLC, Florida

[12] HALL, L., BODARE, A. (2000) *Analyses of the cross-hole method for determining shear wave velocities and damping raios*, Soil Dynamics and Earthquake Engineering 20, pages 167-175.

[13] HARDIN, B.O., RICHART Jr, F.E. (1963) *Elastic Wave Velocities in Granular Soils*, Journal of the Soil Mechanics and Foundations Division, Vol. 89, Issue 1, pages 33-66, ASCE.

[14] HARDIN, B.O. (1978) *The nature of stress-strain behaviour of soils*, Earthquake Engineering and Soil Dynamics, Vol. 1, pages 3-90 54(7), ASCE.

[15] HARDIN, B.O., DRNEVICH, V. P. (1972) *Shear Modulus and Damping in Soils: Design Equations and Curves*, Journal of the Soil Mechanics and Foundations division.

[16] HARDIN, B.O., Black. (1972) *Shear Modulus and Damping in Soils: Design Equations and Curves*, Journal of the Soil Mechanics and Foundations division.

[17] HICHER, P. Y. (1996) *Elastic Properties of soils*, Journal of Geotechnical Engineering, 122(8), pages 641-648.

[18] HOQUE, E., TATSUOKA, F. (2004) *Effects of stress ratio on small-strain stiffness during triaxial shearing*, Géotechnique, 54(7), pages 429-439.

[19] ISMAIL, M. A., NAYAN, K. A. M., SAMSUDIN, A. R., RAFEK, A. G. (2001) *Spectral Analysis of Surface Waves Method: An Initial Assessment and its Potential Use in Geology*, Geological Society of Malaysia Annual Geological Conference 2001, Malaysia.

[20] JAMIOLKOWSKI, M., LO PRESTI, D. C. F., LEROUEIL, S. (1991) *Design Parameters from Theory to Practice*, Proceedings of the International Conference on Geotechnical Engineering for Coastal Development, Yokohama, Japan, pages 877-917.

[21] KNUDSEN, M. (2014) *On Determination of* G_{max} *by Bender Element and Cross-Hole Testing*, Norwegian University of Science and Technology, Geotechnical division.

[22] KRAMER, S. L. (1996) *Geotechnical Earthquake Engineering*, Prentice-Hall International series in Civil Engineering and Engineering Mechanics, University of Washington.

[23] KULKARNI, S. V. (2016) *Information Signals, Course Compendium*, Course ELE201, Princeton University.

[24] KUWANO, R., JARDINE, R. J. (2002) *On the Application of Cross-Anisotropic Elasticity to Granular Materials at Very Small Strains*, Géotechnique, Volume 52, Issue 10, pages 727-749.

[25] L'HEUREUX, J. S. (2012) *Natural Hazards Project: Work Package 6 - Quick Clay: Characterisation of Historical Quick Clay Landslides and Input Parameters for Q-Bing*, Norwegian Geotechnical Institute (NGI), Norwegian Water Resources and Energy Directorate (NVE), Norwegian Public Roads Administration (NPRA), Norwegian National Railways Administration (NNRA).

[26] L'HEUREUX, J. S., EMDAL, A., LINDGÅRD, A. (2019) *Geotechnical Characterication of the Tiller-Flotten Quick Clay Site in Norway*, XVII European Conference on Soil Mechanics and Geotechnical Engineering 2019.

[27] L'HEUREUX, J. S., LONG, M. (2016) *Correlations between Shear Wave Velocity and Geotechnical Parameters in Norwegian Clays*, NGM Nordic Geotechnical Meeting, Conference, Reykjavik.

[28] L'HEUREUX, J. S., LONG, M. (2017) *Relationship between Shear-Wave Velocity and Geotechnical Parameters for Norwegian Clays*, Journal of Geotechnical and Geoenvironmental Engineering, Volume 143, Issue 6.

[29] LO PRESTI, D. C. F., JAMIOLKOWSKI, M. (1998) *Estimate of Elastic Shear Modulus in Holocene Soil Deposits*, Soils and Foundations, Volume 38, pages 43-46.

[30] LO PRESTI, D. C. F., JAMIOLKOWSKI, M., PALLARA, O., CAVALLARO, A. (1996) *Rate and Creep Effect on the Stiffness of Soils*, Measuring and Modelling Time Dependent Soil Behaviour, Geotechnical Special Publication, Volume 61, pages 166-180.

[31] LONG, M., DONAHUE, S. O'CONNOR, P. (2008) *Rapid, Cost Effective and Accurate Determination of in situ Stiffness using MASW at Bothkennar*, Ground Engineering, pages 43-46, Thomas Telford Ltd.

[32] LONG, M., DONAHUE, S. (2007) *In situ Shear Wave Velocity from Multichannel analysis of Surface waves (MASW) Tests at Eight Norwegian Research Sites*, Canadian Geotechnical Journal, Vol. 44, Issue 5, pages 533-544.

[33] Loughborough University (2002) *An Introduction to MEMS (Micro-ElectroMechanical Systems)*, Prime Faraday Partnership, Wolfson School of Mechanical and Manufacturing Engineering, Loughborough University, Leicester.

[34] LUNA, R., JADI, H. (2000) *Determination of Dynamic Soil Properties using Geophysical Methods*, International Concerence on the Application of Geophysical and NDT Methodologies to Transportation Facilities and Infrastructure, St. Lous.

[35] MARCHETTI, M., TOTANI, G., MONACO, P., MARCHETTI, D. (2008) *In Situ Tests by Seismic Dilatometer (SDMT)*, Conference Paper in Geotechnical Special Publication, march 2008.

[36] Mitchell, J. K. (1994) *Fundamentals of soil behaviour, 2nd edition*, John Wiley Sons.

[37] National Instruments (n.d) *What is LabView*, [Online], <http://www.ni.com/en-us/shop/labview.html>, accessed 26.05.2019.

[38] NGI, Norwegian Geotechnical Institute (n.d) *NGTS - Norwegian Geo-Test Sites*, <https://www.ngi.no/eng/Projects/NGTS-Norwegian-Geo-Test-Sites>, accessed 10.05.2019

[39] NGI, Norwegian Geotechnical Institute (2017) *Tiller-Flotten Revised SDMT Data 14-02-17*, Excel file handed out by L'Heureux, J. S.

[40] NGU, Norwegian Geological Survey (n.d) *Dette er Kvikkleire og Kvikkleirekart*, <https://www.ngu.no/nyheter/dette-er-kvikkleire-og-kvikkleirekart>, accessed 11.05.2019

[41] NGU, Norwegian Geological Survey (n.d) *Kartdatabase*, <https://www.ngu.no/emne/kart-pa-nett>, accessed 24.03.2019

[42] PARK, C. B., MILLER, R. D., XIA, J., IVANOV, J. (2001) *Seismic Characterization of Geotechnical Sites By Multichannel Analysis of Surface Waves (MASW) Method*, Kansas Geological Survey, University of Kansas, Kansas, USA.

[43] PECKER, A. (2007) *Advanced Earthquake Engineering Analysis*, International Centre for Mechanical Sciences, SpringerWienNewYork.

[44] REYNOLDS, J. M. (2011) *An Introcution to Applied and Environmental Geophysics, 2nd edition*, Wiley-Blackwell, West-Sussex, UK.

[45] SHIBUYA, S., TATSUOKA, F., TEACHAVORASINSKUN, S., KONG, X. J., ABE, F., KIM, Y., PARK, C. (1992) *Elastic Deformation Properties of Geomaterials*, Soils and Foundations, Vol. 32, Issue 3, pages 26-46.

[46] STOKOE, K. H., SANTAMARINA, J.C (2000) *Seismic-wave based testing in geotechnical engineering*, Vol. 1, pages 1490-1536. Technomic publishing company, Australia.

[47] STOKOE, K. H., DARENDELI, M. B., GILBERT, R. B., MENQ, F. Y., CHOI, W. K. (2004). *Development of a New Family of Normalized Modulus Reduction and Material Damping Curves*. International Workshop on Uncertainties in Nonlinear Soil Properties and their Impact on Modeling Dynamic Soil response, Berkeley, CA.

[48] SULLY, J. P., CAMPANELLA, R. G. (1995) *Evaluation of in situ anisotropy from crosshole and downhole shear wave velocity measurements*, Geotechnique Vol. 45, Issue 2, pages 267-282.

[49] VIGGIANI, G., ATKINSON, J.H (1995) *Stiffness of Fine Grained Soils at Very Small Strains*, Geotechnique Vol. 45, Issue 1, pages 249-265.

[50] VUCETIC, M., DOBRY, R. (1991) *Effect of soil plasticity on cyclic response*, Journal of Geotechnical Engineering, 117(1), pages 89-107, ASCE.

[51] WICHTMANN, T., TRIANTAFYLLIDIS, T. (2004) *Influence of a Cyclic and Dynamic Loading History on Dynamic Properties of Dry Sand*, Soil Dynamics and Earthquake Engineering, Vol. 24, Issue 2, pages 127-147.

[52] YU, P., RICHART, F. E. (1984) *Stress Ratio Effects on Shear Modulus of Dry Sands*, Journal of Geotechnical Engineering, Vol. 110, issue 3, pages 331-345.

Appendix A

Acronyms

v_s	Shear wave velocity
v_p	Pressure wave velocity
v_R	Rayleigh wave velocity
G	Shear modulus
G_{sec}	Secant shear modulus
G_{max}	Small strain strain shear modulus
γ	Shear strain
γ_c	Cyclic shear strain
ρ	Density
A	Area
F	Force
ϵ	strain
ϵ_V	Volumetric strain
V	Volume
σ	Stress
σ'_1	Major effective principle stress

σ'_3 Minor effective principle stress

σ'_v Effective vertical stress

σ'_h Effective Horizontal stress

σ'_m Mean effective confining stress

σ_r Reference stress

K_0 Coefficient of earth pressure at rest

ζ Damping ratio

τ Shear stress

η Material viscosity

ω Angular Frequency

W Peak Energy during load cycle

λ & μ Lamé constants

SV Polarised shear wave in the vertical plane

SH Polarised shear wave in the horizontal plane

ν Poisson's ratio

λ Wavelength

γ_t Unit weight

e Void ratio

S_t Sensitivity

OCR Overconsolidation ratio

I_p Plasticity index

I_D Density Index

w_l Water limit

$SASW$	Spectral Analysis of Surface Waves
$MASW$	Multichannel Analysis of Surface Waves
CHT	Cross-Hole Test
$SDMT$	Seismic Dilatometer Test
$CPTU$	Cone penetration Test with pore pressure measurements
TPS	Total Pressure Sounding
$SCPTU$	Seismic Cone Penetration Test
ERT	Electrical Resistivity Tomography
CRS	Constant Rate of Strain oedometer test
DSS	Direct Simple Shear test
q_t	Cone resistance
u	Pore pressure
B_q	Pore pressure parameter
s_u	Undrained shear strength
s_{ur}	Remoulded shear strength
$CAUe$	Anisotropic consolidation, undrained extension test
$CAUc$	Anisotropic consolidation, undrained compression test

Appendix B

Task Description

The topic of this Master thesis was worked out as an agreement between Steinar Nordal, Arnfinn Emdal and myself, and this topic did not have a predetermined task description. It was suggested to conduct new cross-hole tests for determination of the small strain shear stiffness G_{max} at the NGTS test site on Flotten, Norway.

The task requires a literature study, to find out what parameters affect G_{max}, and how they affect it. The literature study will also cover methods of acquiring the G_{max} of soils.

The objectives are the following:

1. Presentation of theory regarding the determination of G_{max}, and parameters affecting it.
2. Evaluation of the cross-hole seismic method.
3. Compare the results from cross-hole testing to the results from previous investigations on site.

Appendix C

Results of Cross-Hole Test

This appendix present results for the conducted seismic cross-hole tests at Flotten, Tiller. In the following sections, results from 2.5 m and 5 m depth are presented as total response curves, as well as close-ups of the most prominent curves. For evaluation of the shear wave velocity (v_s), travel times between accelerometer A1 and A2 are investigated from the close-ups. Arrows from equivalent points on the response curve indicate the time difference between the two accelerometers. The largest response was observed in y-direction (depth direction) for vertical impact direction, as well as horizontal direction R1 and R1. For the horizontal impact directions R3 and R4, the receiver response in coordinate direction x was the dominant, and is therefore the preferred for tests with R3 and R4 directions.

Cross-hole test at 2.5 meters depth were done with manual recording of seismic response, requiring the user to coordinate the impact time and press the record button at the right time. This method gave signal output over 1000 ms, which proved sufficient to record the signals of interest but yielded no consistent zero time event. For testing at 5 meters depth, the registration software was updated to automatically trigger at time of impact, recording 20 ms before and the following 100 ms after first impact. Using this software the zero time is set to 20 ms before first impact. This variation in software setup from 2.5 to 5 meters depth lead to inconsistent time axes in the results between the two depths. Since only the time difference between received signals from accelerometers A1 and A2 is required to calculate the shear wave velocity, the variation in times displayed on results is not of any importance.

C.1 Results from 2.5 Meters Depth

The first day of testing (24.05.2019) was done at 2.5 meters depth. The borehole for accelerometer A1 was augered to 2 m depth, and the receiver was penetrated the last 0.5 m. The borehole for A2 was drilled to the full depth, and the accelerometer was pushed through the masses to 2.5 m. The response curves from these tests showed no obvious response at the accelerometer, and therefore the shear wave velocity could not be easily identified. See chapter 8 for possible explanations, and sources of error that may have led to these results. 7 tests were done with vertical impact direction, while 8 tests were done with horizontal impact direction; 2 strikes with a sledgehammer in directions R1, R2, R3, and R4.

All results from testing at 2.5 meters depth gave no clear wave arrivals, and consisted predominantly of noise spikes. These results are not included, but can be supplied by demand.

C.2 Results from 5 Meters Depth

The second day of testing (04.06.2019) was conducted at 5 meters depth. The accelerometers were pressed through the clay from the previous depth of 2.5m, requiring no preboring or augering. The response at the accelerometers were significantly improved from the test at 2.5 m. 8 tests were done with vertical impact direction, while 12 tests were done with horizontal impact direction; 3 strikes with a sledgehammer in directions R1, R2, R3, and R4. An illustration of the horizontal impact directions was given in figure 6.6, but is given again for every test with horizontal impact for easy reference. In this section results from two of each impact direction is presented. Tests with vertical impact direction was expected to produce the best results, but instead yielded chaotic response signals. Horizontal strikes parallel to the receivers (towards or away from receivers) gave most dominant response in y-direction, while impact normal to the linear configuration gave most promising response in x-direction.

C.2.1 Cross-hole Test 1, Vertical Impact

Tests were done by striking a sledgehammer vertically on top of the drillrod. Figure C.1 gives the total response registered by both A1 and A2. A close-up of the response in y-direction for determination of G_{max} is presented in figure C.2. due to somewhat chaotic and incoherent response, the determination of time difference between receivers A1 and A2 proved difficult. a visual evaluation of the responses still gave time estimates in the same order as later tests with better response.

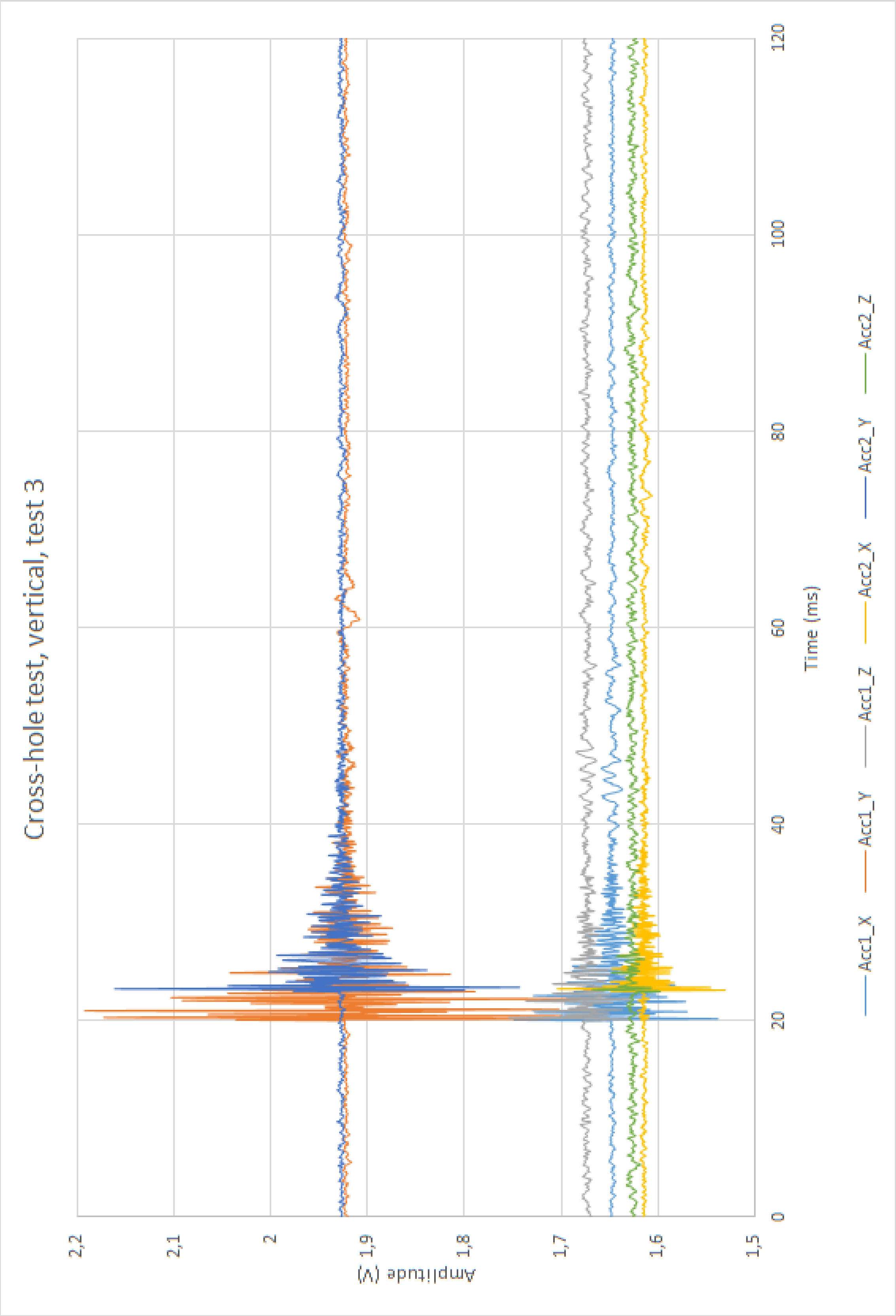

Figure C.1: Total response curve from cross-hole test with vertical impact direction. The curves constitute response in x-, y-, and z-direction for accelerometers A1 and A2. Testing conducted with automatic trigger, signals recorded are 20ms before and 100 ms after first impact using a 100 mV trigger threshold.

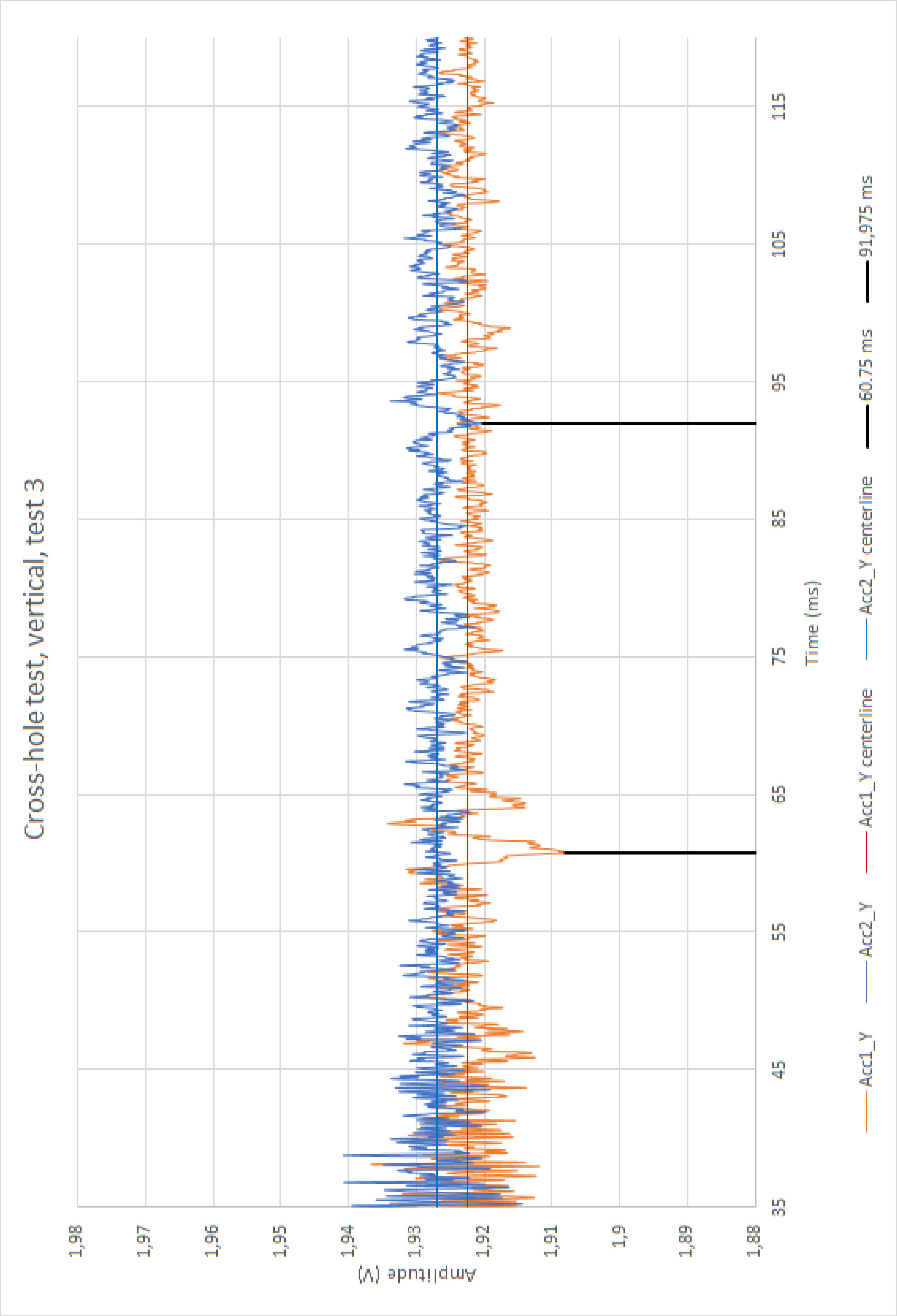

Figure C.2: Cross-hole test with vertical impact direction. Close-up of response in y-direction for determination of shear wave velocity, v_s. Orange curve is for signals received by A1, while the blue curve is by A2. Black lines mark equivalent points, used for determination of time difference between A1 and A2.

C.2.2 Cross-hole Test 2, Vertical Impact

Tests were done by striking a sledgehammer vertically on top of the drillrod. Figure C.3 gives the total response registered by both A1 and A2. A close-up of the response in y-direction for determination of G_{max} is presented in figure C.4. due to somewhat chaotic and incoherent response, the determination of time difference between receivers A1 and A2 proved difficult. a visual evaluation of the responses still gave time estimates in the same order as later tests with better response.

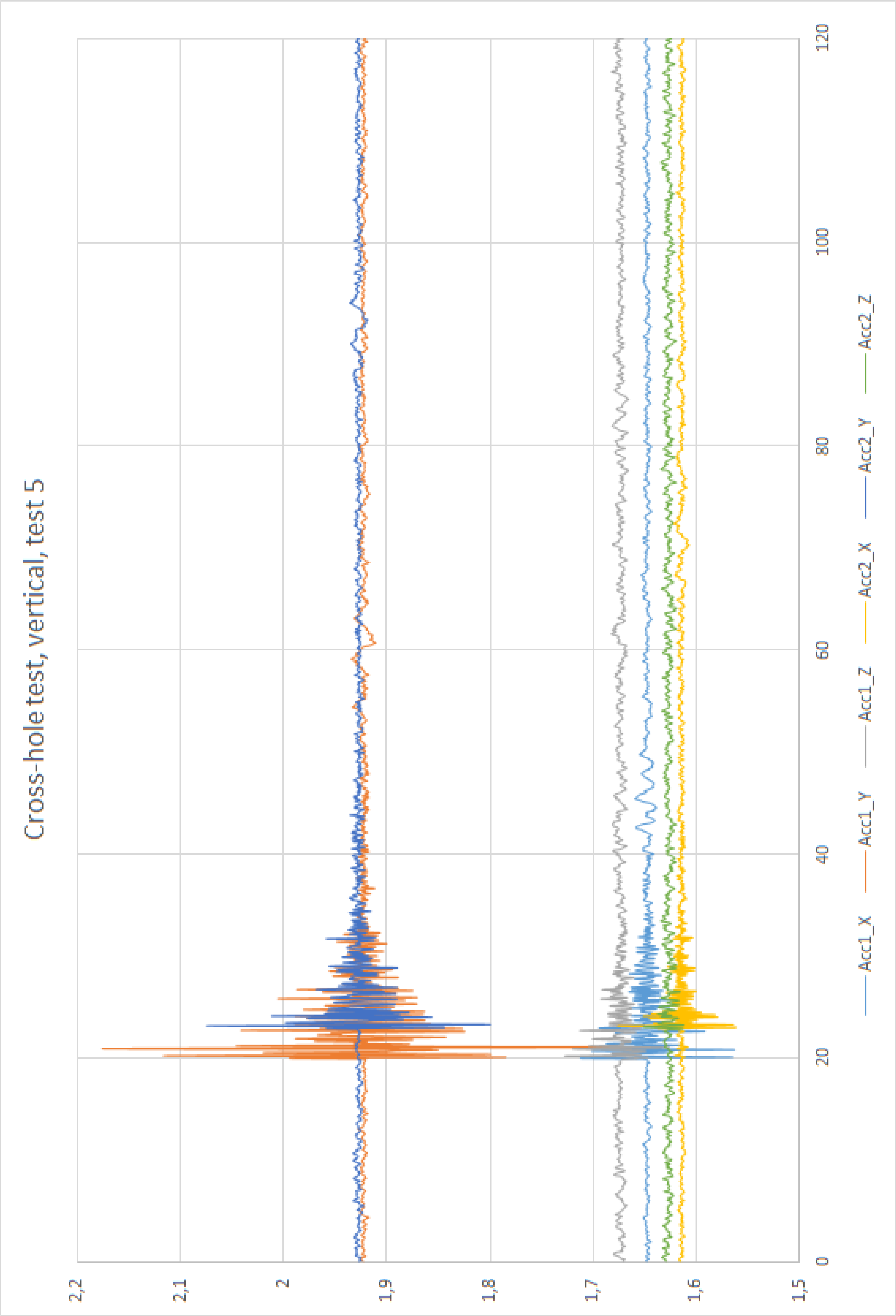

Figure C.3: Total response curve from cross-hole test with vertical impact direction. The curves constitute response in x-, y-, and z-direction for accelerometers A1 and A2. Testing conducted with automatic trigger, signals recorded are 20ms before and 100 ms after first impact using a 100 mV trigger threshold.

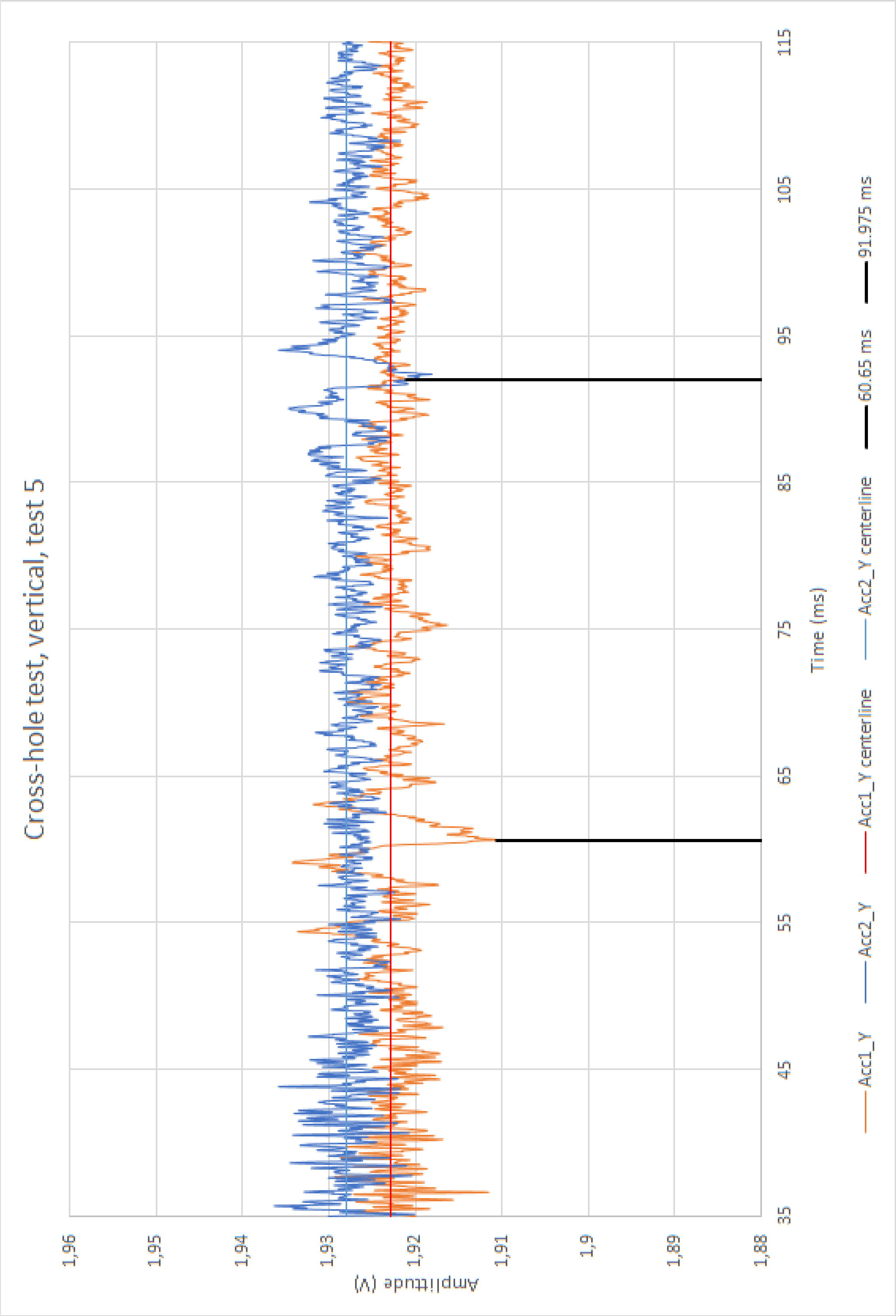

Figure C.4: Cross-hole test with vertical impact direction. Close-up of response in y-direction for determination of shear wave velocity, v_s. Orange curve is for signals received by A1, while the blue curve is by A2. Black lines mark equivalent points, used for determination of time difference between A1 and A2.

C.2.3 Cross-hole Test 3, Horizontal Impact R1

For test with direction R1, a blow from the sledgehammer was given to the drillrod in a direction parallel to, and away from the receivers, as seen from figure C.5. Figure C.6 gives the total response registered by both A1 and A2. A close-up of the response in y-direction for determination of G_{max} is presented in figure C.7.

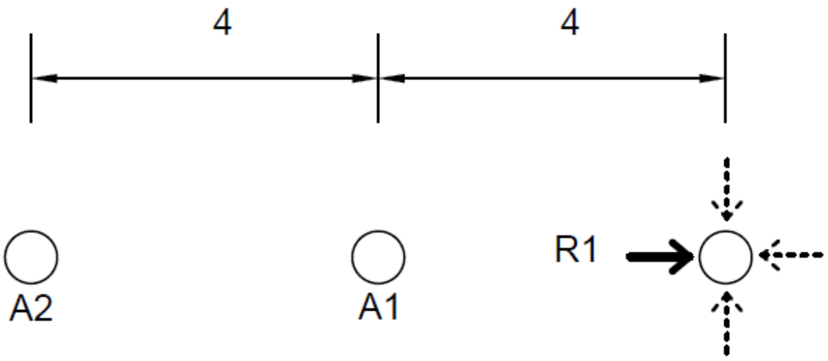

Figure C.5: Impact direction R1 seen from above. Length measurements in meters.

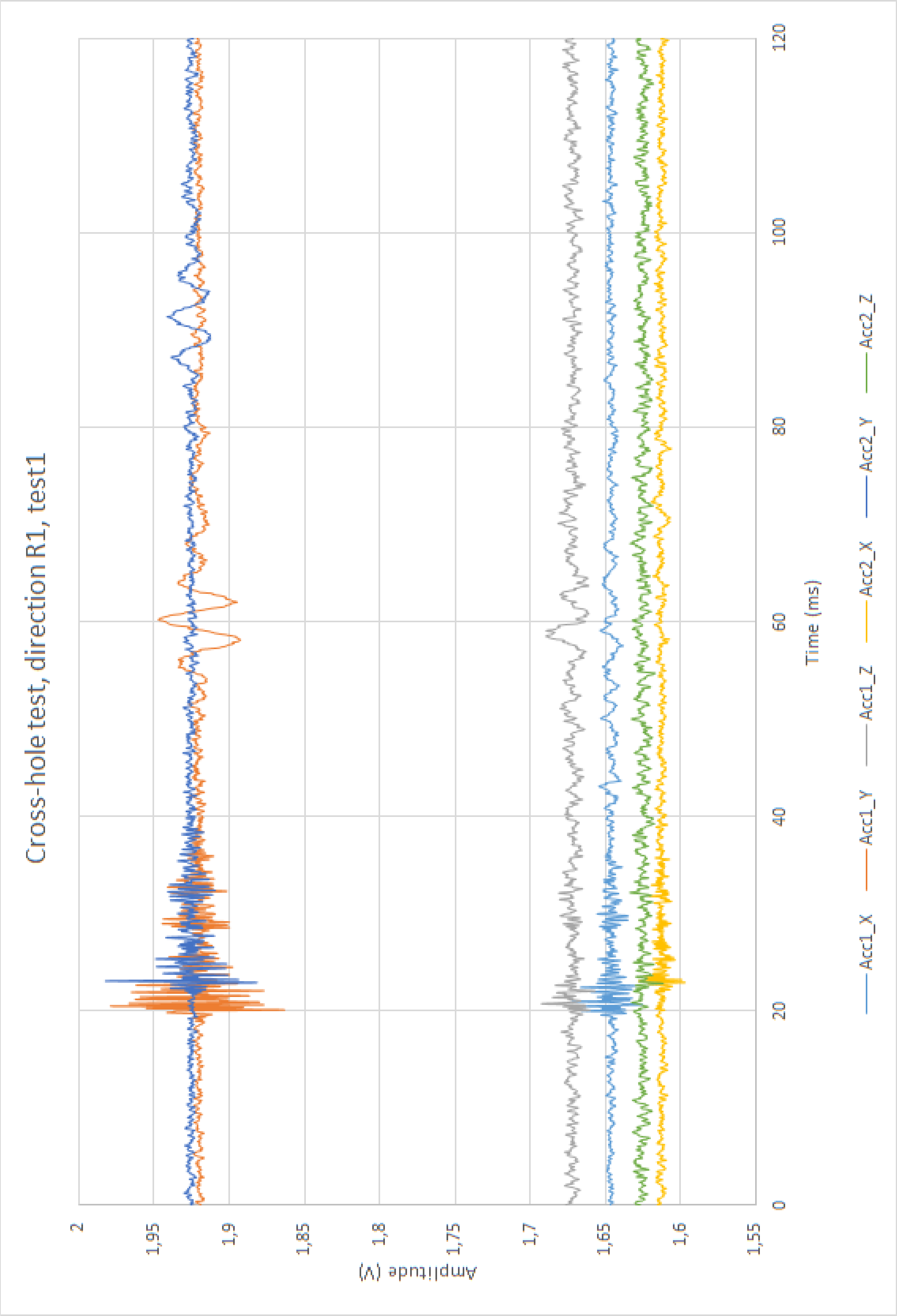

Figure C.6: Total response curve from cross-hole test with horizontal impact direction R1, test 3. The curves constitute response in x-, y-, and z-direction for accelerometers A1 and A2. Testing conducted with automatic trigger, signals recorded are 20ms before and 100 ms after first impact using a 30 mV trigger threshold.

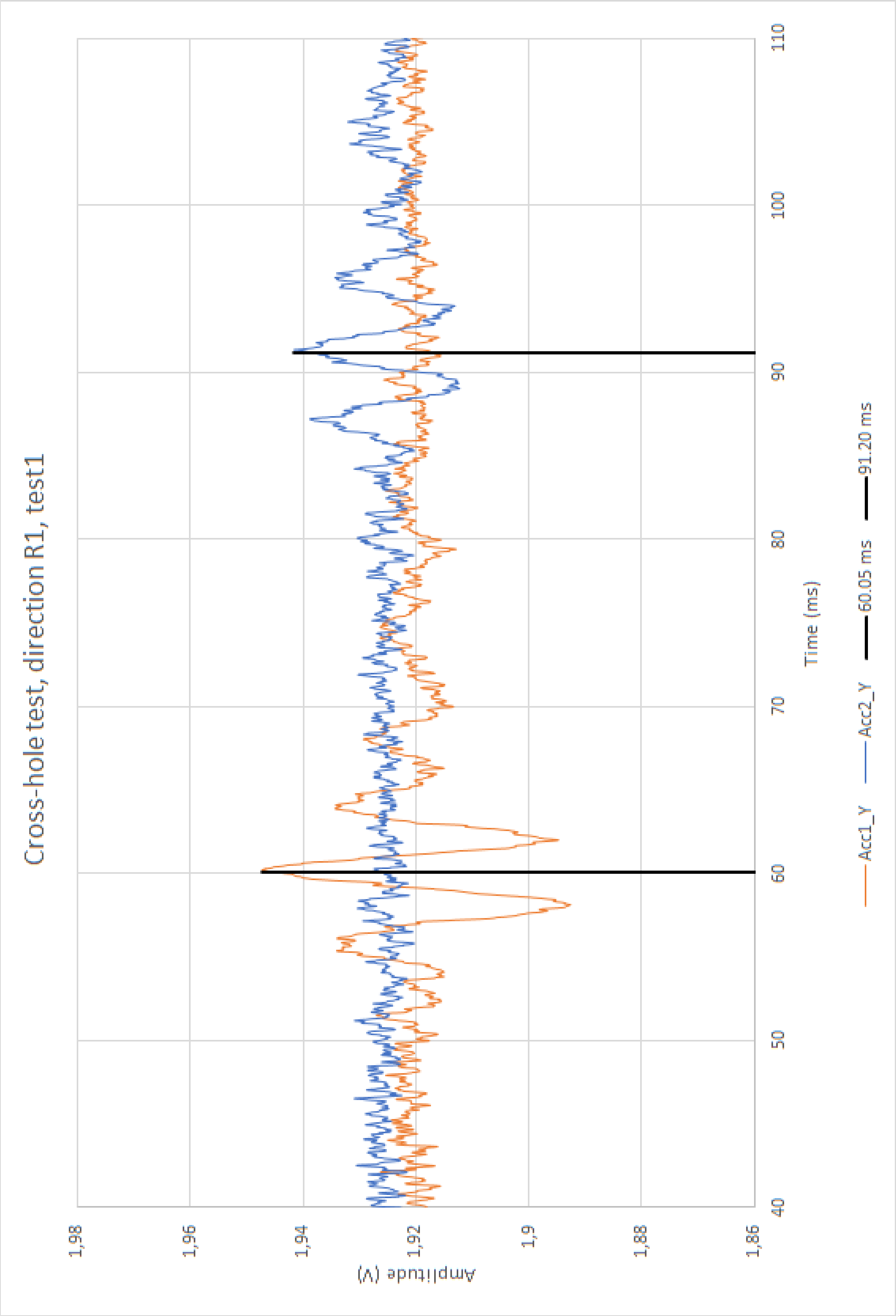

Figure C.7: Cross-hole test with horizontal impact direction R1, test 3. close-up of response in y-direction for determination of shear wave velocity, v_s. Orange curve is for signals received by A1, while the blue curve is by A2. Black lines mark equivalent points, used for determination of time difference between A1 and A2.

C.2.4 Cross-hole Test 4, Horizontal Impact R1

For test with direction R1, a blow from the sledgehammer was given to the drillrod in a direction parallel to, and away from the receivers, as seen from figure C.8. Figure C.9 gives the total response registered by both A1 and A2. A close-up of the response in y-direction for determination of G_{max} is presented in figure C.10.

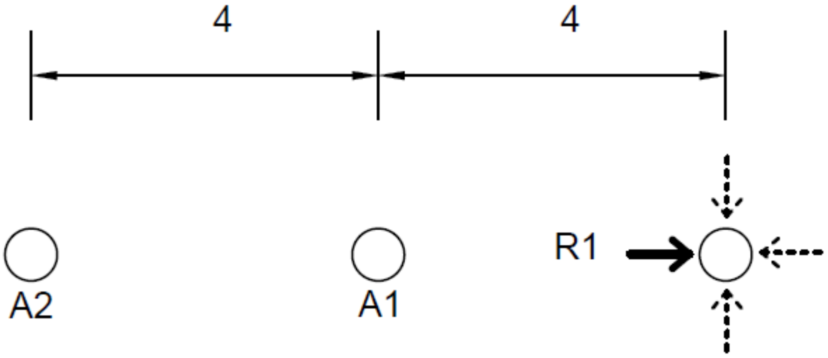

Figure C.8: Impact direction R1 seen from above. Length measurements in meters.

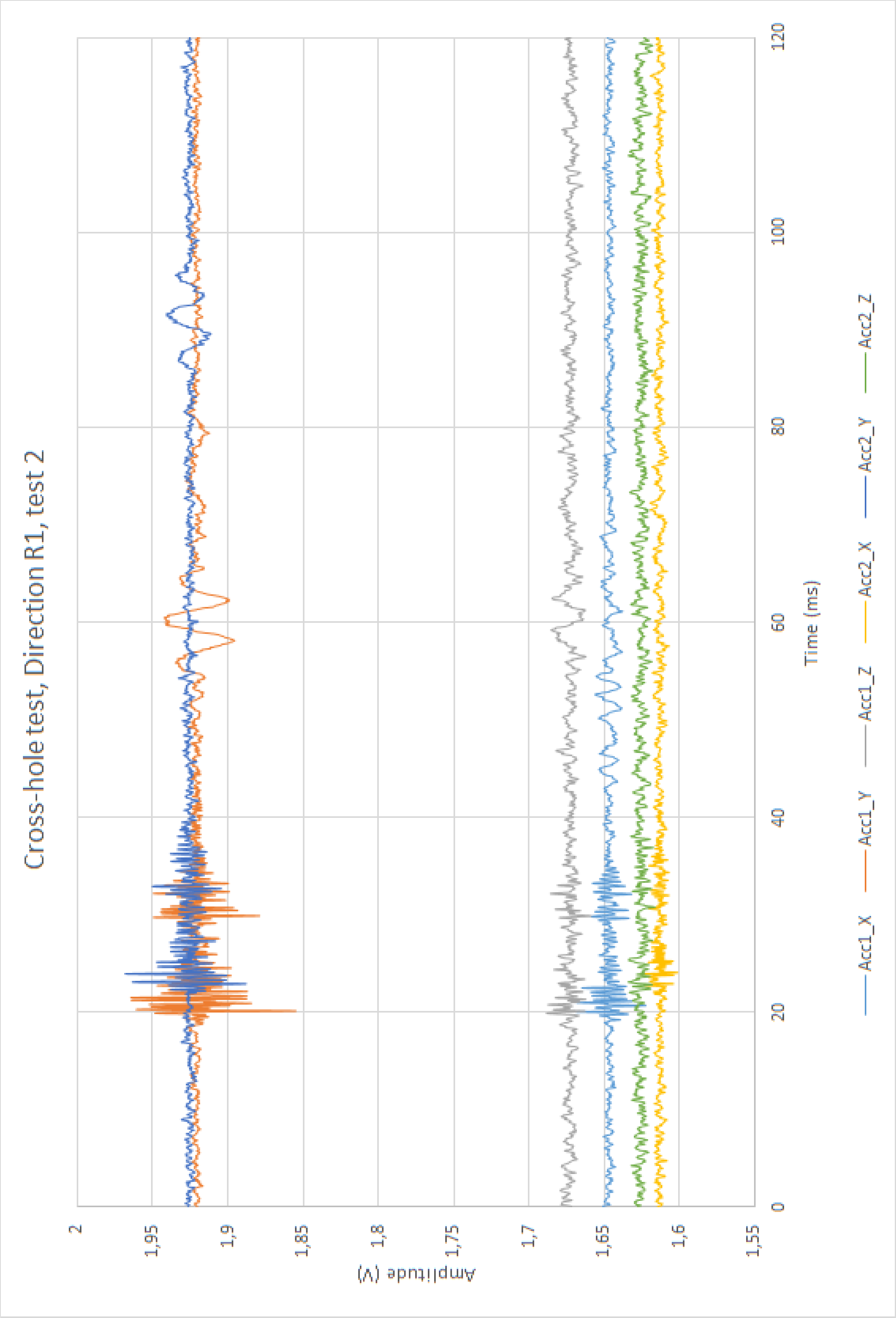

Figure C.9: Total response curve from cross-hole test with horizontal impact direction R1, test 4. The curves constitute response in x-, y-, and z-direction for accelerometers A1 and A2. Testing conducted with automatic trigger, signals recorded are 20ms before and 100 ms after first impact using a 30 mV trigger threshold.

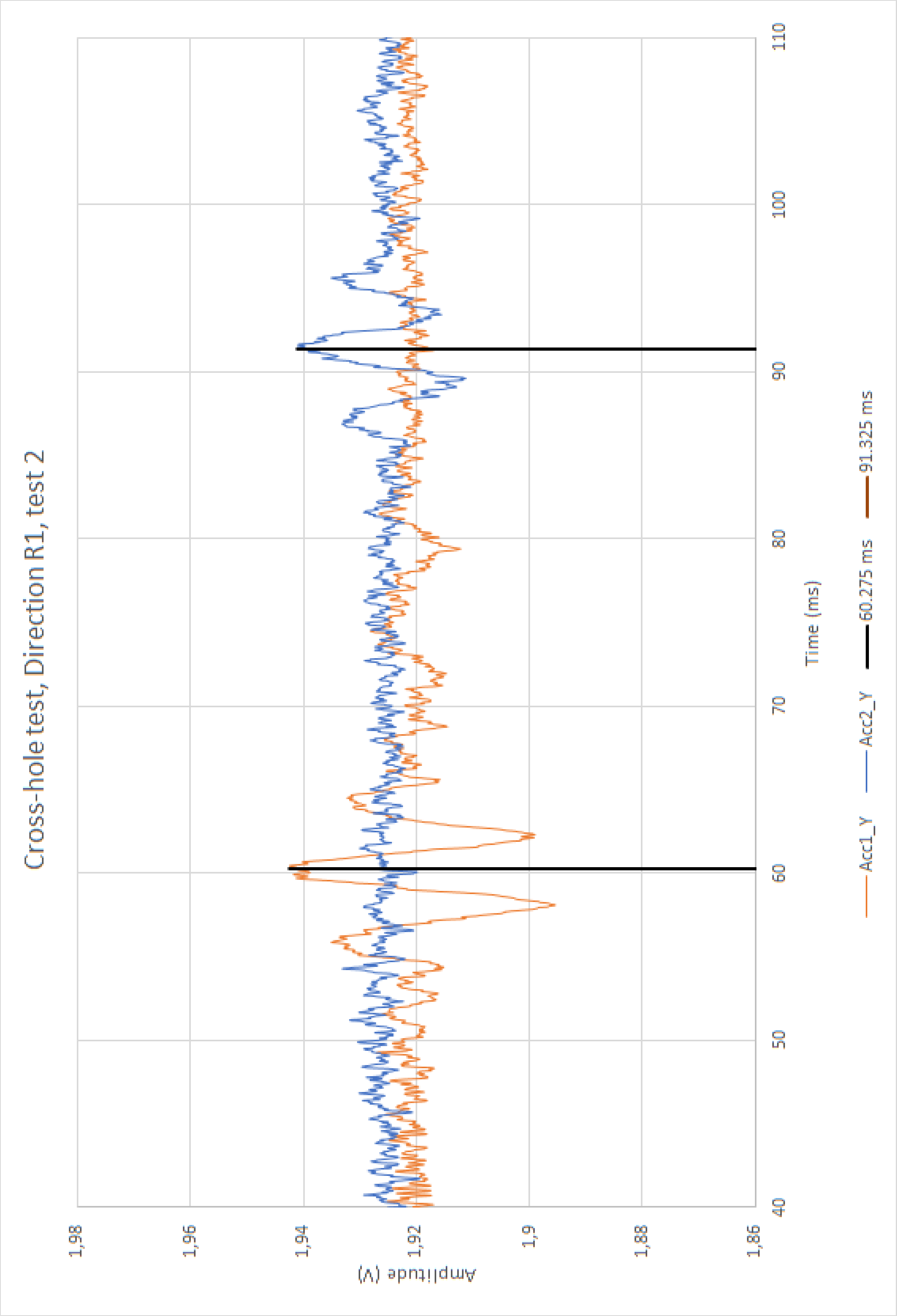

Figure C.10: Cross-hole test with horizontal impact direction R1, test 4. close-up of response in y-direction for determination of shear wave velocity, v_s. Orange curve is for signals received by A1, while the blue curve is by A2. Black lines mark equivalent points, used for determination of time difference between A1 and A2.

C.2.5 Cross-hole Test 5, Horizontal Impact R2

For test with direction R2, a blow from the sledgehammer was given to the drillrod in a direction parallel to, and towards the receivers, as seen from figure C.11. Figure C.12 gives the total response registered by both A1 and A2. A close-up of the response in y-direction for determination of G_{max} is presented in figure C.13. Due to somewhat chaotic response, interpreting equivalent events proved difficult. A centerline was added to figure C.13 to better visualise the major deflections.

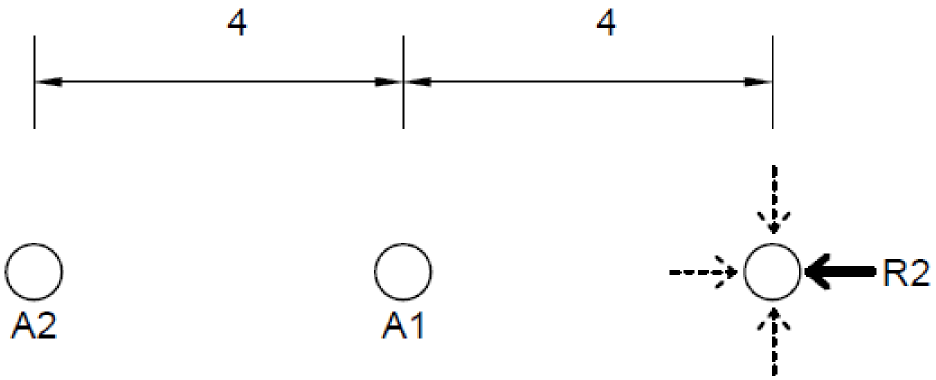

Figure C.11: Impact direction R2 seen from above. Length measurements in meters.

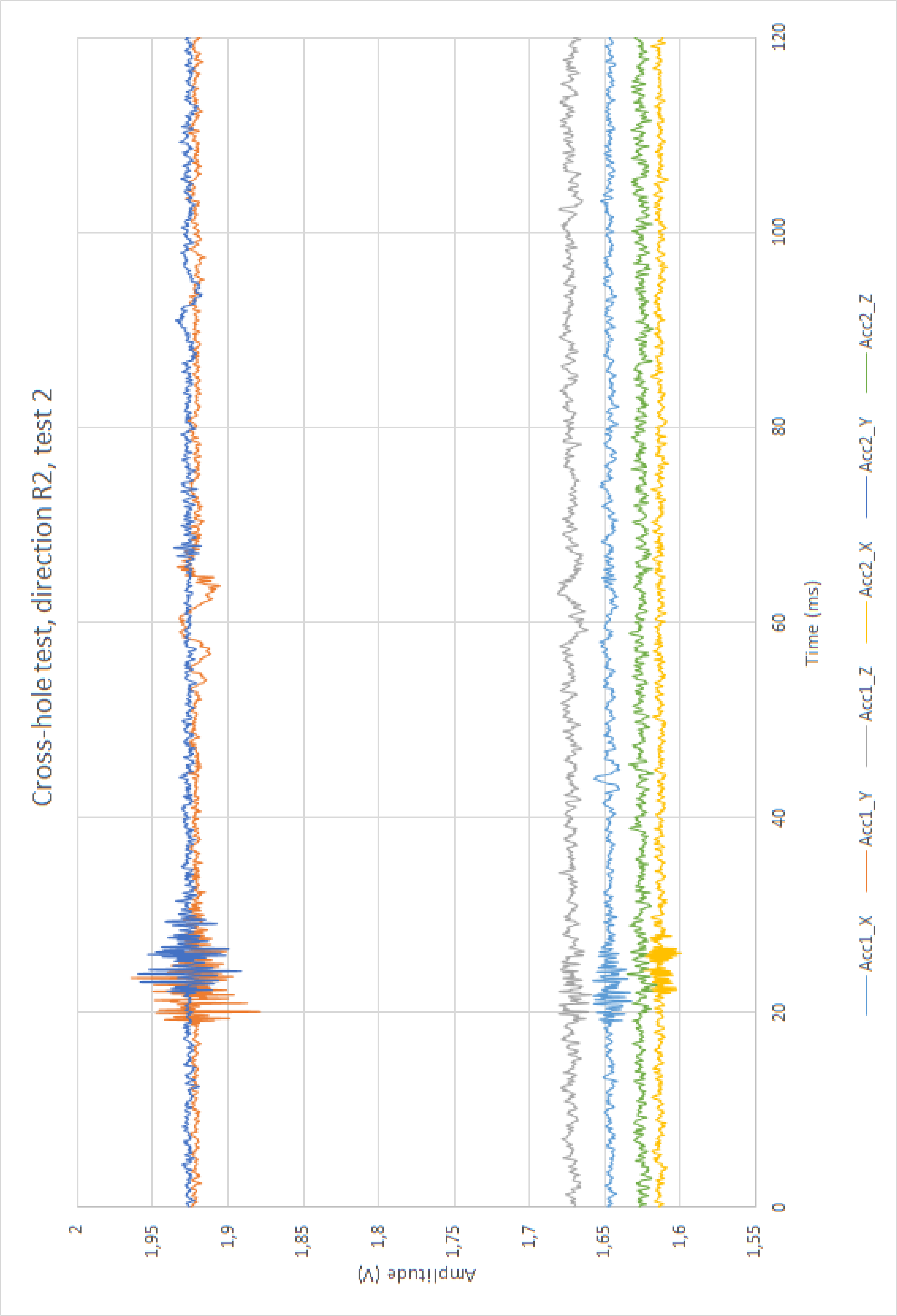

Figure C.12: Total response curve from cross-hole test with horizontal impact direction R2, test 5. The curves constitute response in x-, y-, and z-direction for accelerometers A1 and A2. Testing conducted with automatic trigger, signals recorded are 20ms before and 100 ms after first impact using a 30 mV trigger threshold.

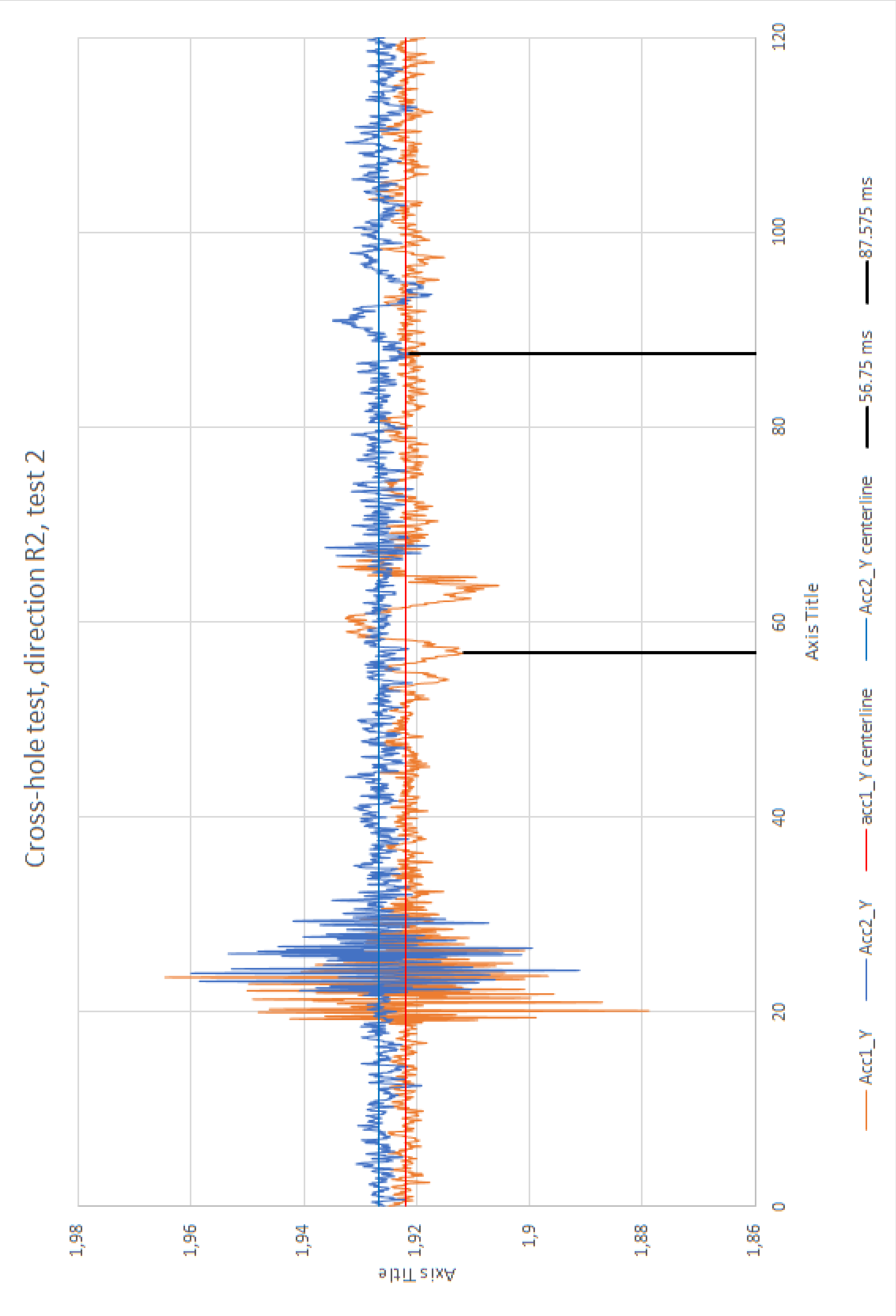

Figure C.13: Cross-hole test with horizontal impact direction R2, test . close-up of response in y-direction for determination of shear wave velocity, v_s. Orange curve is for signals received by A1, while the blue curve is by A2. Black lines mark equivalent points, used for determination of time difference between A1 and A2. A centerline was added to help point out major deflections above noise level.

C.2.6 Cross-hole Test 6, Horizontal Impact R2

For test with direction R2, a blow from the sledgehammer was given to the drillrod in a direction parallel to, and towards the receivers, as seen from figure C.14. Figure C.15 gives the total response registered by both A1 and A2. A close-up of the response in y-direction for determination of G_{max} is presented in figure C.16.

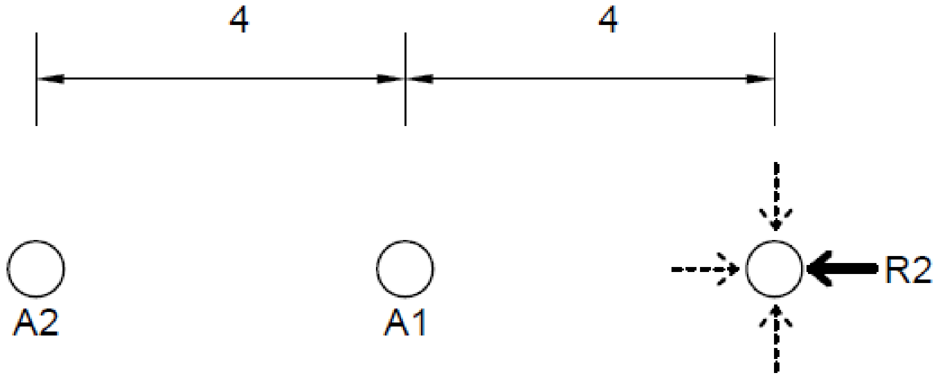

Figure C.14: Impact direction R2 seen from above. Length measurements in meters.

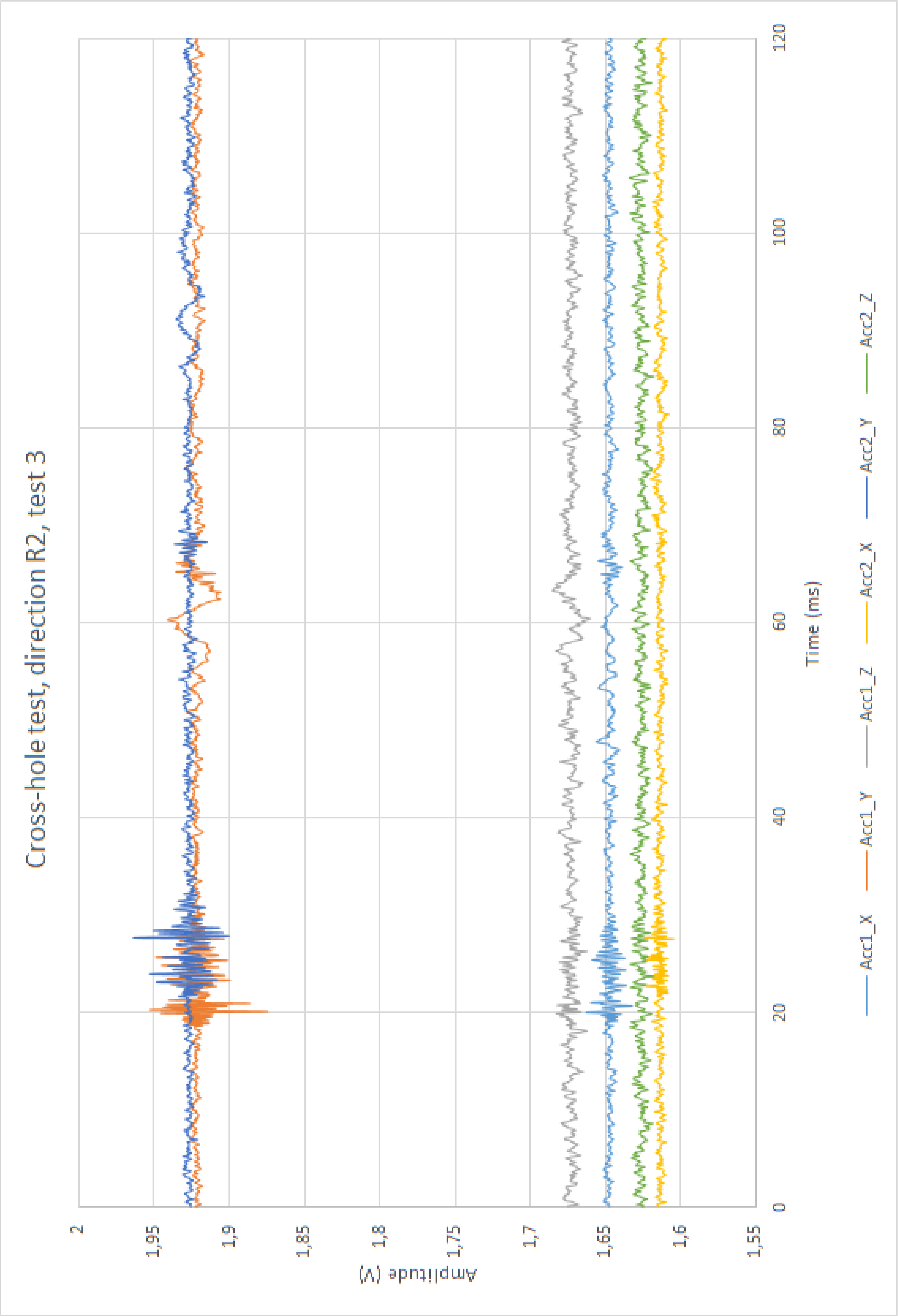

Figure C.15: Total response curve from cross-hole test with horizontal impact direction R2, test 6. The curves constitute response in x-, y-, and z-direction for accelerometers A1 and A2. Testing conducted with automatic trigger, signals recorded are 20ms before and 100 ms after first impact using a 30 mV trigger threshold.

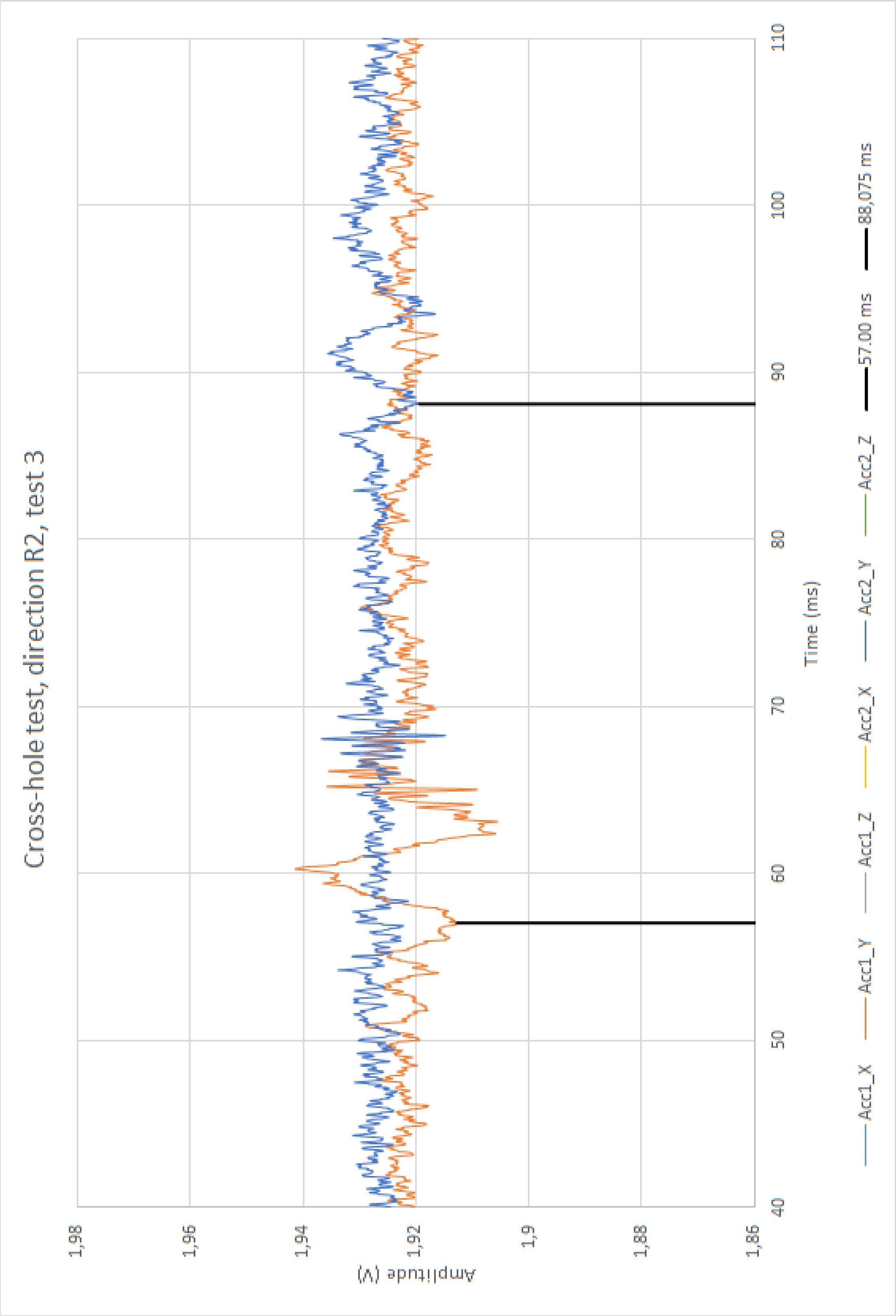

Figure C.16: Cross-hole test with horizontal impact direction R2, test 6. Close-up of response in y-direction for determination of shear wave velocity, v_s. Orange curve is for signals received by A1, while the blue curve is by A2. Black lines mark equivalent points, used for determination of time difference between A1 and A2.

C.2.7 Cross-hole Test 7, Horizontal Impact R3

For test with direction R3, a blow from the sledgehammer was given to the drillrod in a direction normal to the direction of receiver setup, as seen from figure C.17. Figure C.18 gives the total response registered by both A1 and A2. A close-up of the response in x-direction for determination of G_{max} is presented in figure C.19.

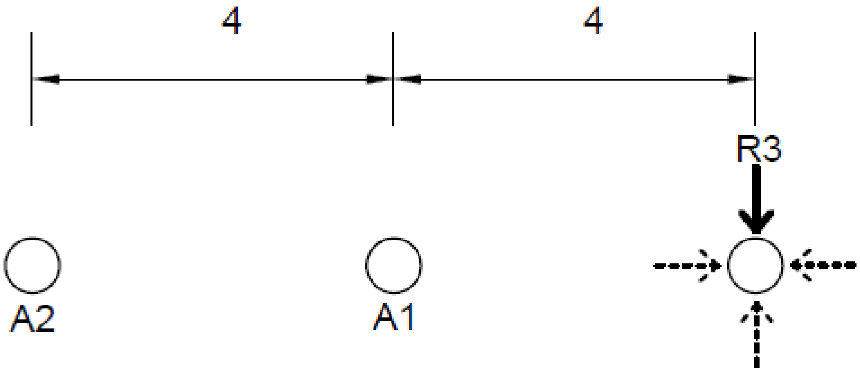

Figure C.17: Impact direction R3 seen from above. Length measurements in meters.

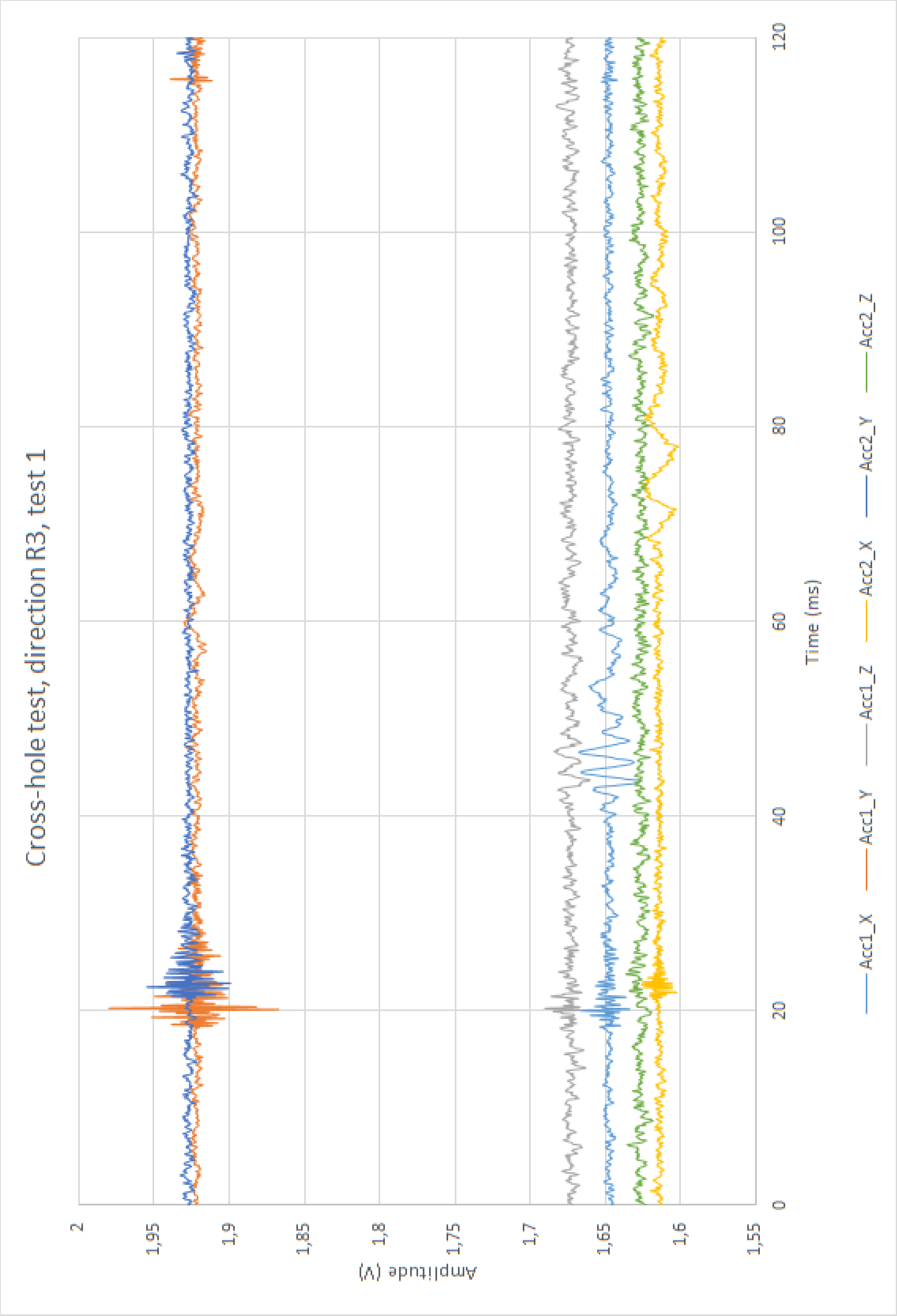

Figure C.18: Total response curve from cross-hole test with horizontal impact direction R3, test 7. The curves constitute response in x-, y-, and z-direction for accelerometers A1 and A2. Testing conducted with automatic trigger, signals recorded are 20ms before and 100 ms after first impact using a 30 mV trigger threshold.

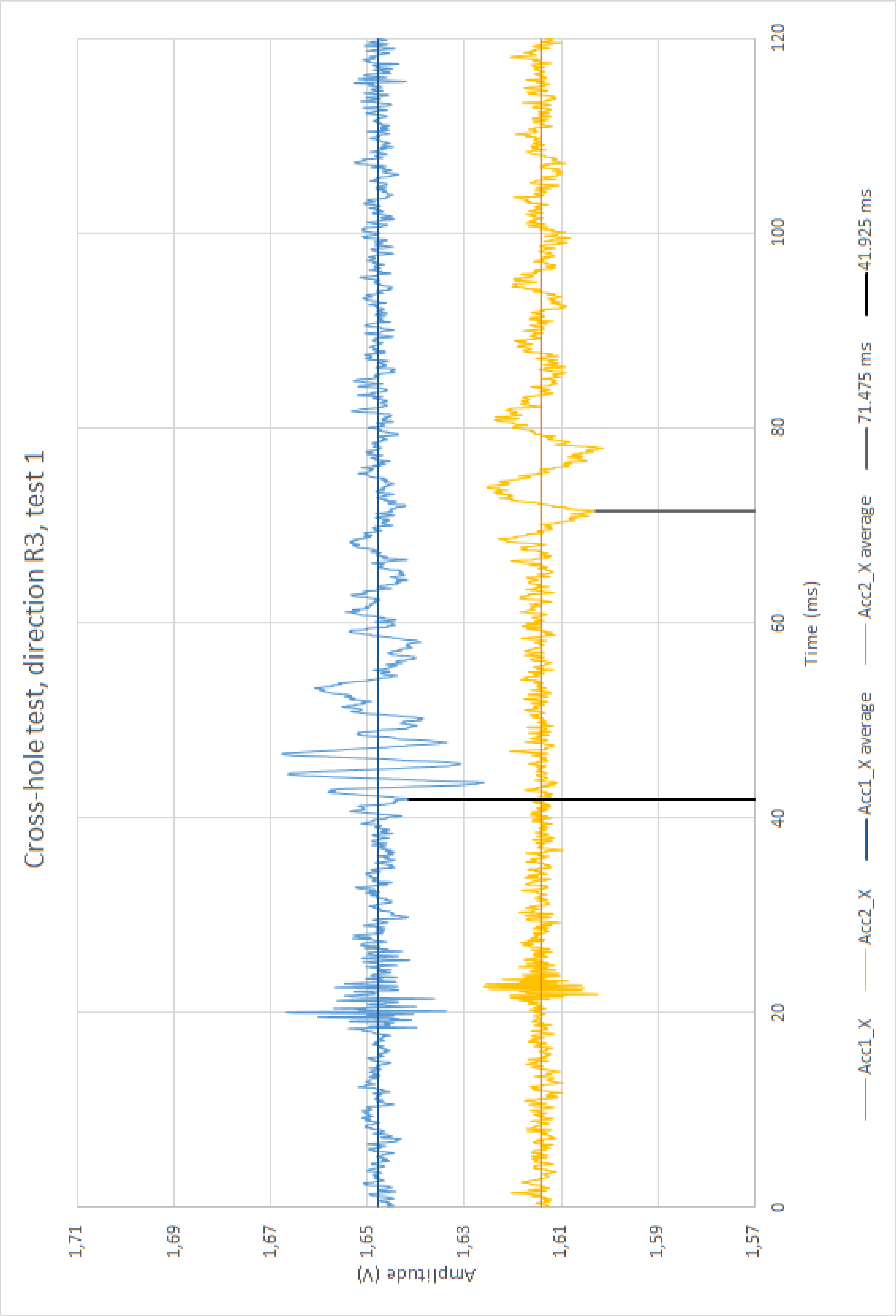

Figure C.19: Cross-hole test with horizontal impact direction R3, test 7. Close-up of response in x-direction for determination of shear wave velocity, v_s. Blue curve is for signals received by A1, while the yellow curve is by A2. Black lines mark equivalent points, used for determination of time difference between A1 and A2.

C.2.8 Cross-hole Test 8, Horizontal Impact R3

For test with direction R3, a blow from the sledgehammer was given to the drillrod in a direction normal to the direction of receiver setup, as seen from figure C.20. Figure C.21 gives the total response registered by both A1 and A2. A close-up of the response in x-direction for determination of G_{max} is presented in figure C.22.

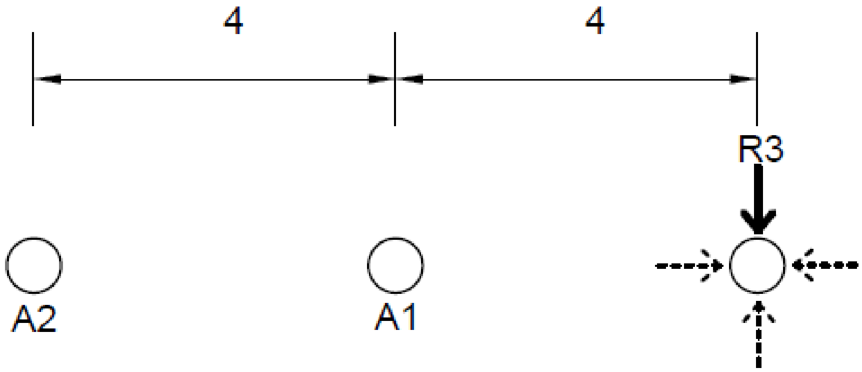

Figure C.20: Impact direction R3 seen from above. Length measurements in meters.

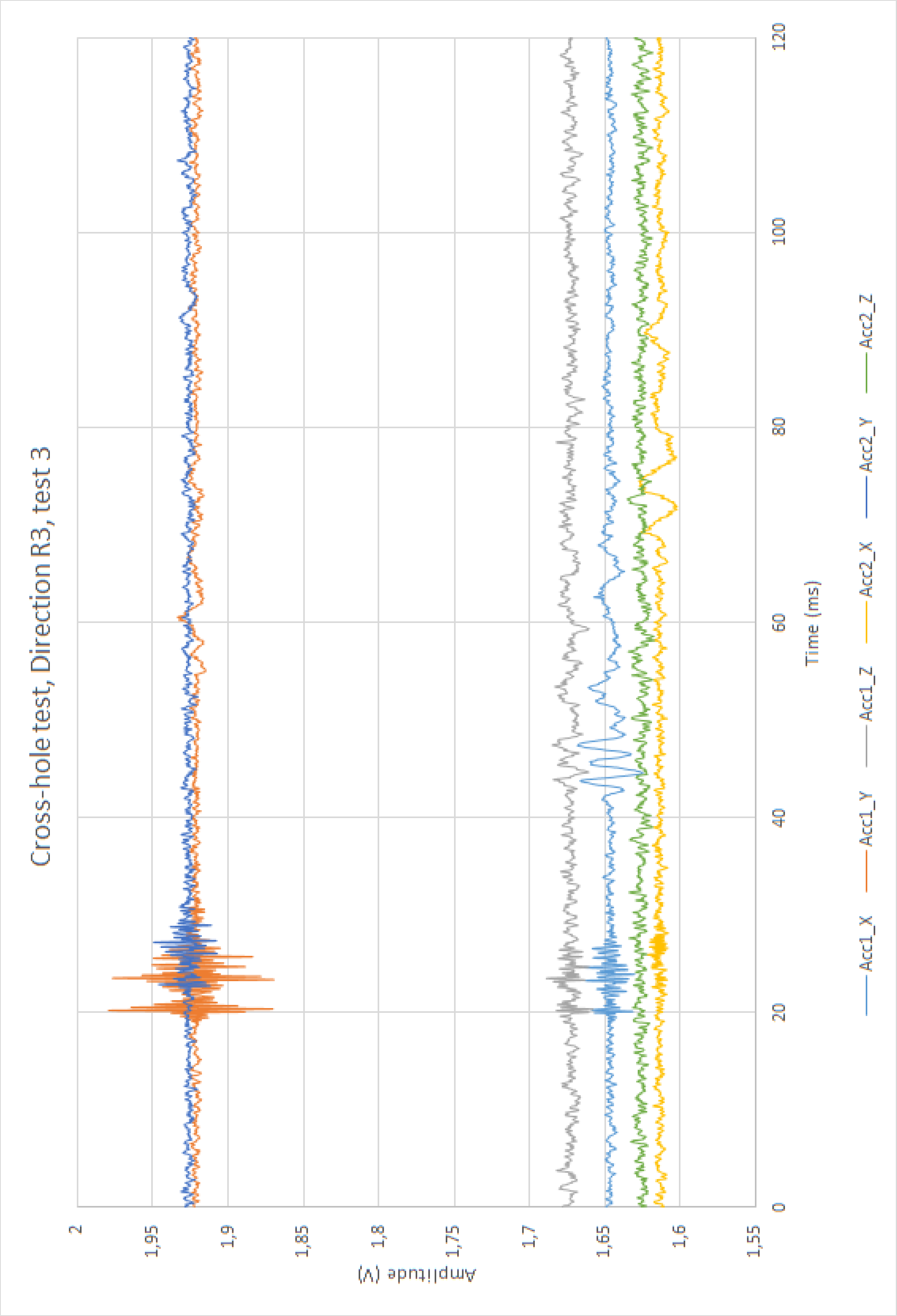

Figure C.21: Total response curve from cross-hole test with horizontal impact direction R3, test 8. The curves constitute response in x-, y-, and z-direction for accelerometers A1 and A2. Testing conducted with automatic trigger, signals recorded are 20ms before and 100 ms after first impact using a 30 mV trigger threshold.

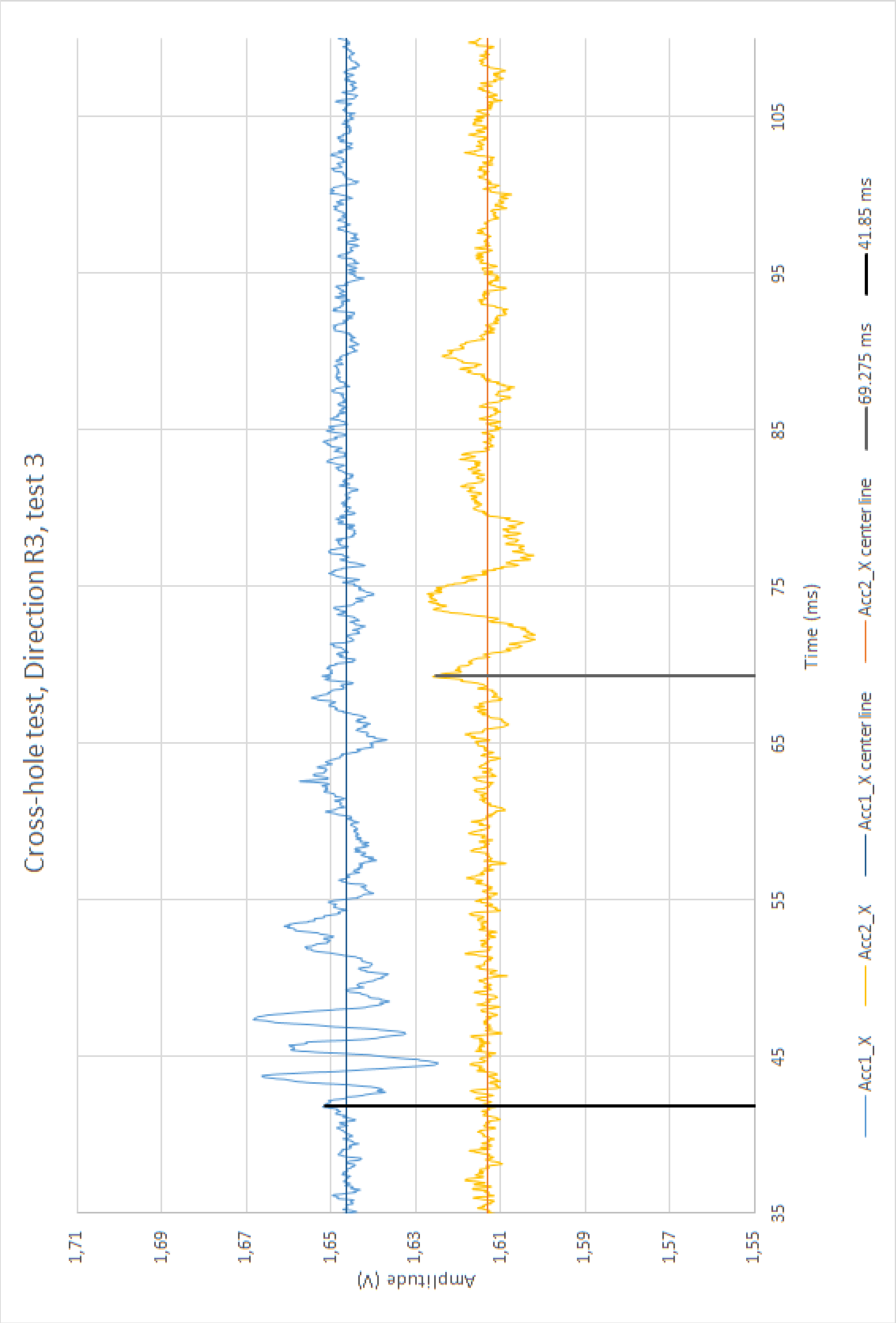

Figure C.22: Cross-hole test with horizontal impact direction R3, test 8. Close-up of response in x-direction for determination of shear wave velocity, v_s. Blue curve is for signals received by A1, while the yellow curve is by A2. Black lines mark equivalent points, used for determination of time difference between A1 and A2.

C.2.9 Cross-hole Test 9, Horizonal Impact R4

For test with direction R4, a blow from the sledgehammer was given to the drillrod in a direction normal to the direction of receiver setup, but opposite of direction R4. The strike direction is illustrated in figure C.23. Figure C.24 gives the total response registered by both A1 and A2. A close-up of the response in x-direction for determination of G_{max} is presented in figure C.25.

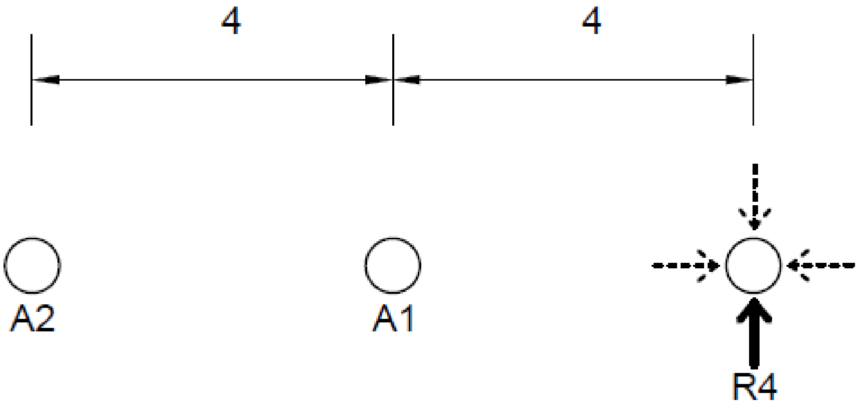

Figure C.23: Impact direction R4 seen from above. Length measurements in meters.

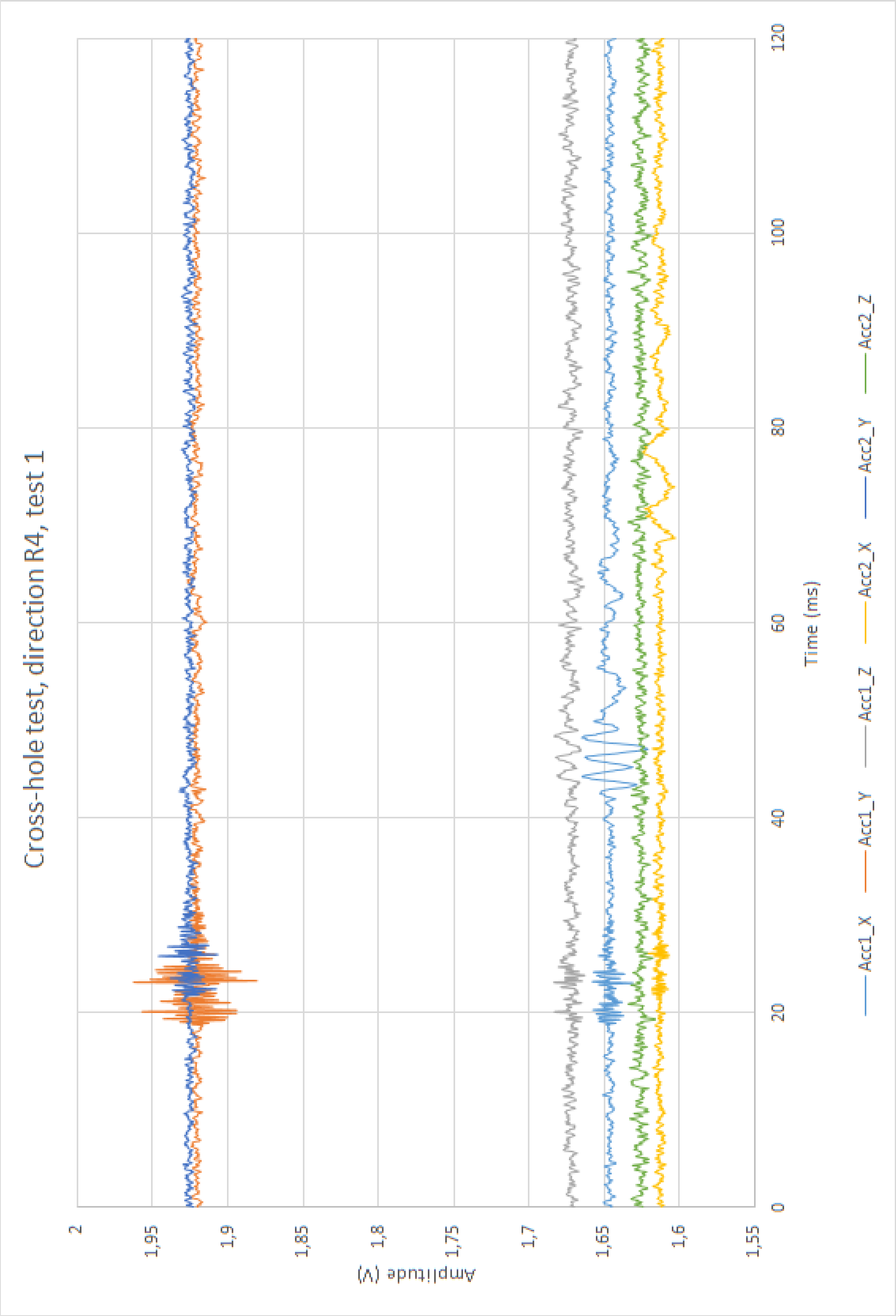

Figure C.24: Total response curve from cross-hole test with horizontal impact direction R4, test 9. The curves constitute response in x-, y-, and z-direction for accelerometers A1 and A2. Testing conducted with automatic trigger, signals recorded are 20ms before and 100 ms after first impact using a 30 mV trigger threshold.

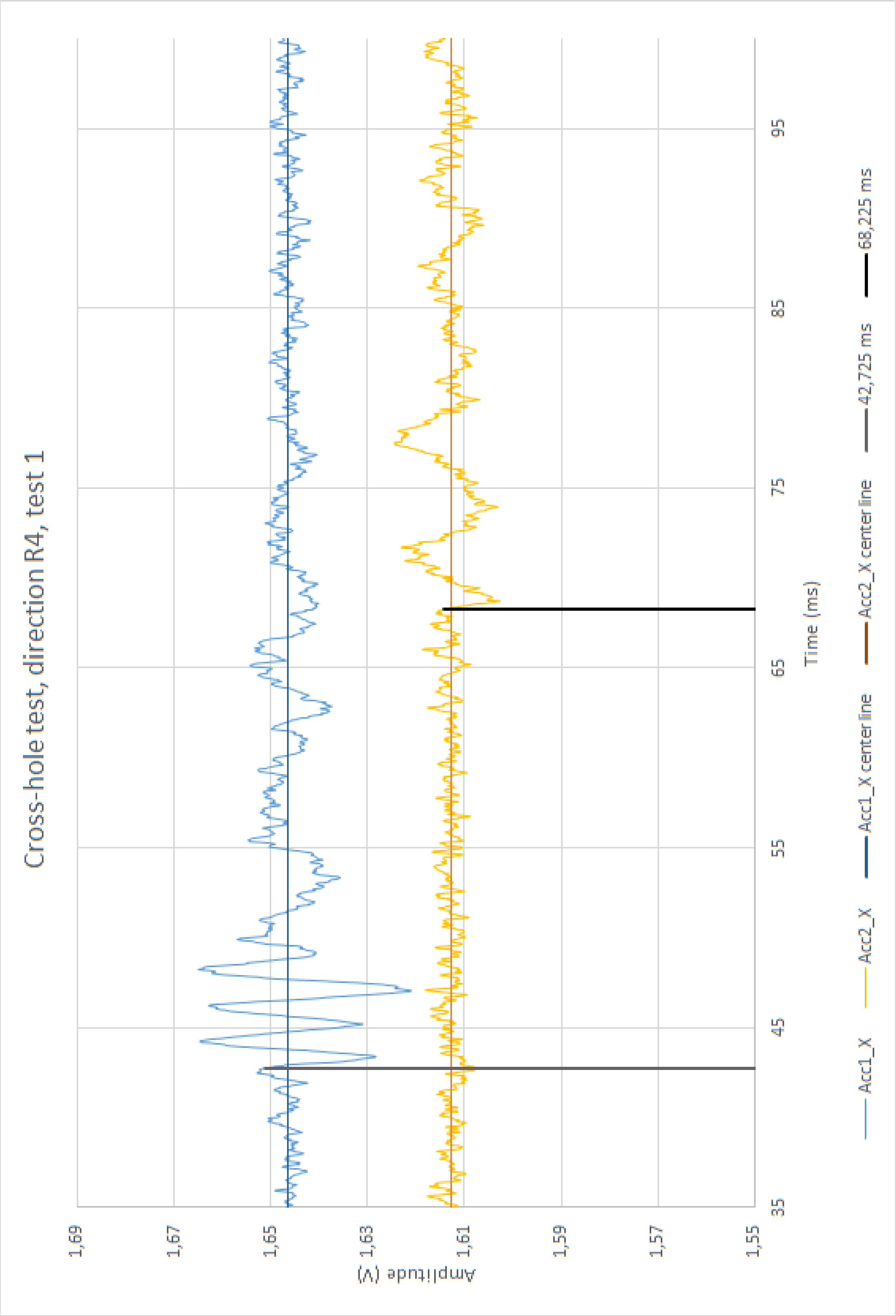

Figure C.25: Cross-hole test with horizontal impact direction R4, test 9. Close-up of response in x-direction for determination of shear wave velocity, v_s. Blue curve is for signals received by A1, while the yellow curve is by A2. Black lines mark equivalent points, used for determination of time difference between A1 and A2.

C.2.10 Cross-hole Test 10, Horizontal Impact R4

For test with direction R4, a blow from the sledgehammer was given to the drillrod in a direction normal to the direction of receiver setup, but opposite of direction R4. The strike direction is illustrated in figure C.26. Figure C.27 gives the total response registered by both A1 and A2. A close-up of the response in x-direction for determination of G_{max} is presented in figure C.28.

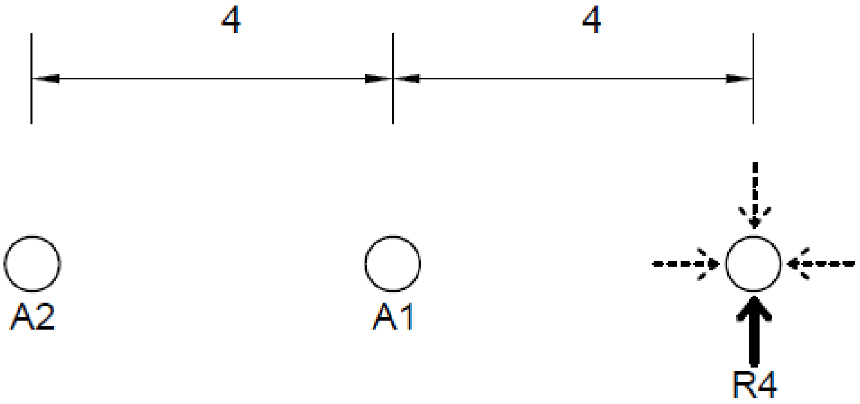

Figure C.26: Impact direction R4 seen from above. Length measurements in meters.

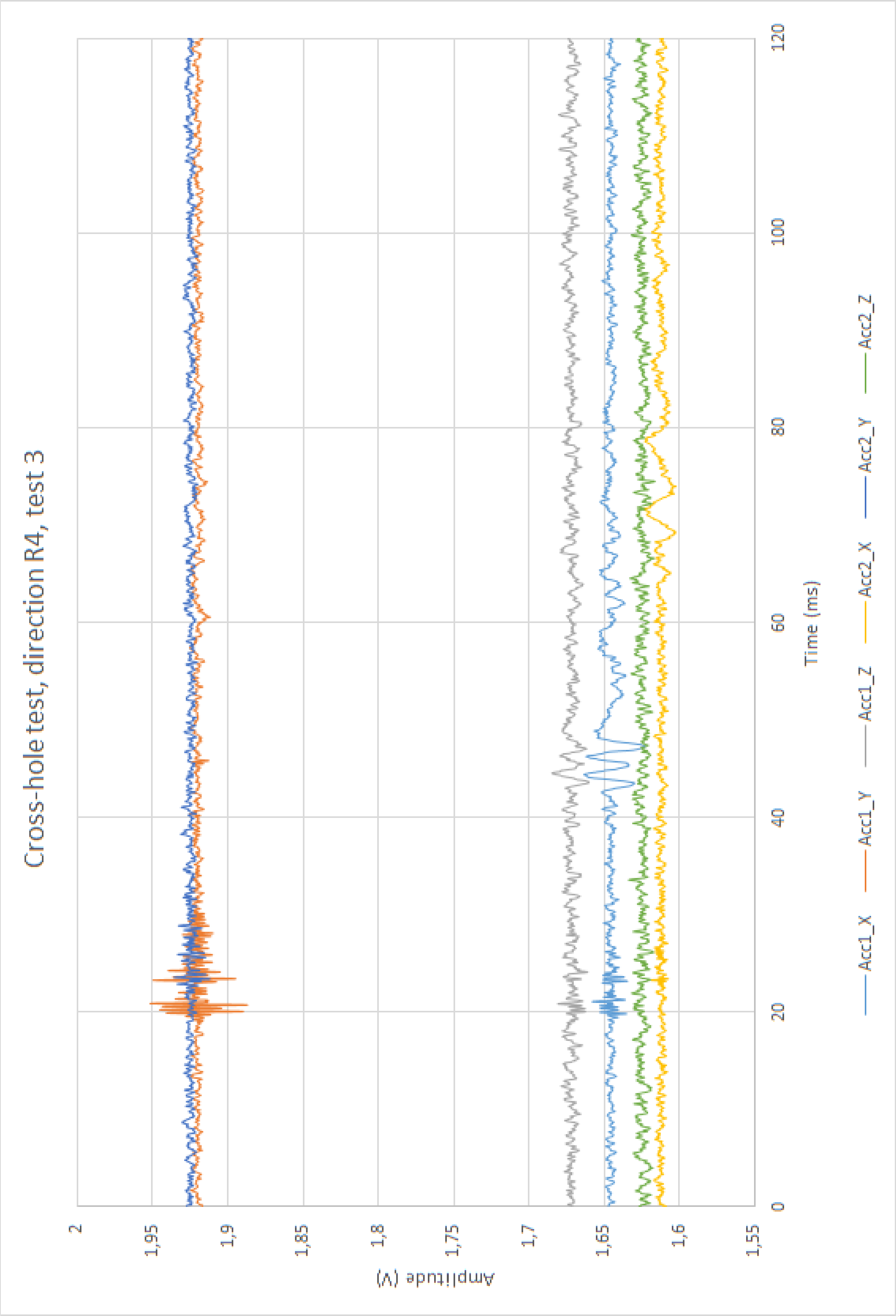

Figure C.27: Total response curve from cross-hole test with horizontal impact direction R4, test 10. The curves constitute response in x-, y-, and z-direction for accelerometers A1 and A2. Testing conducted with automatic trigger, signals recorded are 20ms before and 100 ms after first impact using a 30 mV trigger threshold.

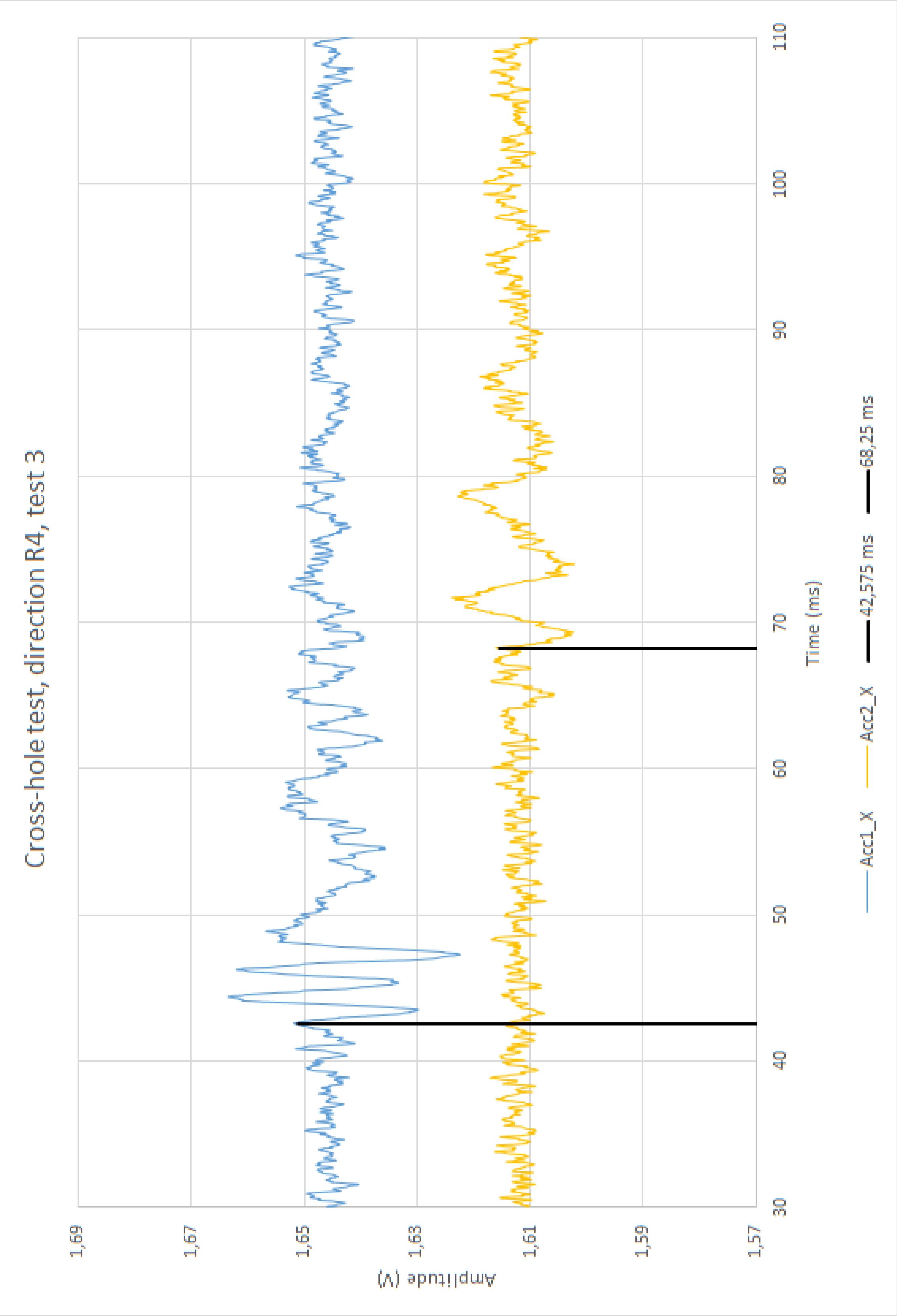

Figure C.28: Cross-hole test with horizontal impact direction R4, test 10. Close-up of response in x-direction for determination of shear wave velocity, v_s. Blue curve is for signals received by A1, while the yellow curve is by A2. Black lines mark equivalent points, used for determination of time difference between A1 and A2.

C.2.11 Overview of results from cross-hole test

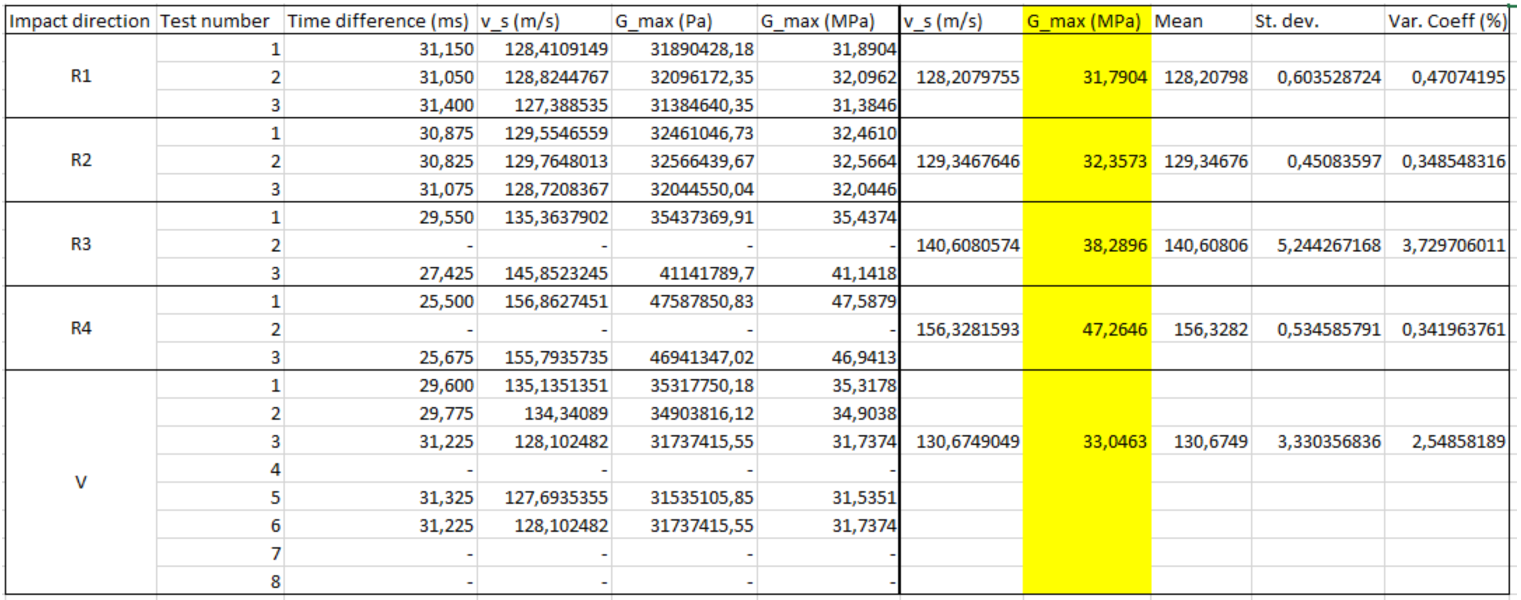

Impact direction	Test number	Time difference (ms)	v_s (m/s)	G_max (Pa)	G_max (MPa)	v_s (m/s)	G_max (MPa)	Mean	St. dev.	Var. Coeff (%)
R1	1	31,150	128,4109149	31890428,18	31,8904	128,2079755	31,7904	128,20798	0,603528724	0,47074195
	2	31,050	128,8244767	32096172,35	32,0962					
	3	31,400	127,388535	31384640,35	31,3846					
R2	1	30,875	129,5546559	32461046,73	32,4610	129,3467646	32,3573	129,34676	0,45083597	0,348548316
	2	30,825	129,7648013	32566439,67	32,5664					
	3	31,075	128,7208367	32044550,04	32,0446					
R3	1	29,550	135,3637902	35437369,91	35,4374	140,6080574	38,2896	140,60806	5,244267168	3,729706011
	2	-	-	-	-					
	3	27,425	145,8523245	41141789,7	41,1418					
R4	1	25,500	156,8627451	47587850,83	47,5879	156,3281593	47,2646	156,3282	0,534585791	0,341963761
	2	-	-	-	-					
	3	25,675	155,7935735	46941347,02	46,9413					
V	1	29,600	135,1351351	35317750,18	35,3178	130,6749049	33,0463	130,6749	3,330356836	2,54858189
	2	29,775	134,34089	34903816,12	34,9038					
	3	31,225	128,102482	31737415,55	31,7374					
	4	-	-	-	-					
	5	31,325	127,6935355	31535105,85	31,5351					
	6	31,225	128,102482	31737415,55	31,7374					
	7	-	-	-	-					
	8	-	-	-	-					

Figure C.29: Results from cross-hole test at 5 m depth.

Appendix D

Seismic Dilatometer Test

SDMT data (NGU, 2017) from the Flotten test site is included to visualize the small strain shear stiffness of the first 20 meters at the NGTS quick clay site on Flotten. Figure D.1 show the table used for calculating $G_{max} values$, while figure D.2 is a plot of the evaluated G_{max} with depth.

D.1 SDMT Results

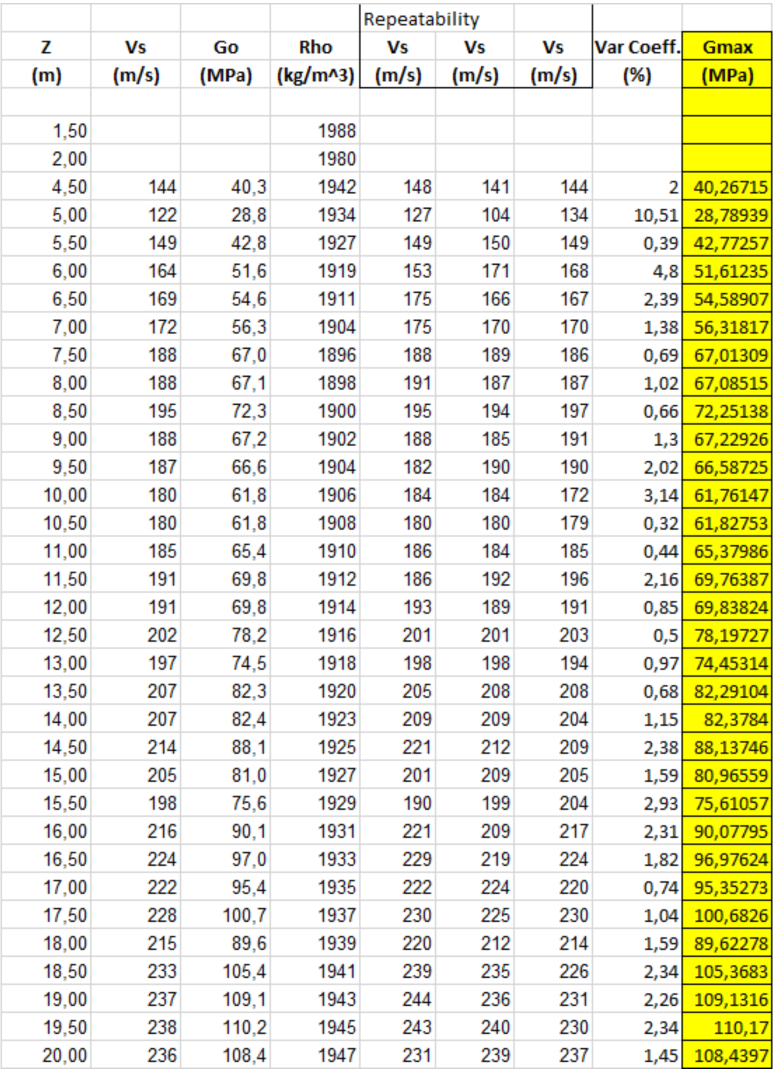

				Repeatability				
Z (m)	Vs (m/s)	Go (MPa)	Rho (kg/m^3)	Vs (m/s)	Vs (m/s)	Vs (m/s)	Var Coeff. (%)	Gmax (MPa)
1,50			1988					
2,00			1980					
4,50	144	40,3	1942	148	141	144	2	40,26715
5,00	122	28,8	1934	127	104	134	10,51	28,78939
5,50	149	42,8	1927	149	150	149	0,39	42,77257
6,00	164	51,6	1919	153	171	168	4,8	51,61235
6,50	169	54,6	1911	175	166	167	2,39	54,58907
7,00	172	56,3	1904	175	170	170	1,38	56,31817
7,50	188	67,0	1896	188	189	186	0,69	67,01309
8,00	188	67,1	1898	191	187	187	1,02	67,08515
8,50	195	72,3	1900	195	194	197	0,66	72,25138
9,00	188	67,2	1902	188	185	191	1,3	67,22926
9,50	187	66,6	1904	182	190	190	2,02	66,58725
10,00	180	61,8	1906	184	184	172	3,14	61,76147
10,50	180	61,8	1908	180	180	179	0,32	61,82753
11,00	185	65,4	1910	186	184	185	0,44	65,37986
11,50	191	69,8	1912	186	192	196	2,16	69,76387
12,00	191	69,8	1914	193	189	191	0,85	69,83824
12,50	202	78,2	1916	201	201	203	0,5	78,19727
13,00	197	74,5	1918	198	198	194	0,97	74,45314
13,50	207	82,3	1920	205	208	208	0,68	82,29104
14,00	207	82,4	1923	209	209	204	1,15	82,3784
14,50	214	88,1	1925	221	212	209	2,38	88,13746
15,00	205	81,0	1927	201	209	205	1,59	80,96559
15,50	198	75,6	1929	190	199	204	2,93	75,61057
16,00	216	90,1	1931	221	209	217	2,31	90,07795
16,50	224	97,0	1933	229	219	224	1,82	96,97624
17,00	222	95,4	1935	222	224	220	0,74	95,35273
17,50	228	100,7	1937	230	225	230	1,04	100,6826
18,00	215	89,6	1939	220	212	214	1,59	89,62278
18,50	233	105,4	1941	239	235	226	2,34	105,3683
19,00	237	109,1	1943	244	236	231	2,26	109,1316
19,50	238	110,2	1945	243	240	230	2,34	110,17
20,00	236	108,4	1947	231	239	237	1,45	108,4397

Figure D.1: Shear wave velocity data from seismic dilatometer testing from 4.5 m to 20 m at the Flotten test site (NGU, 2017)

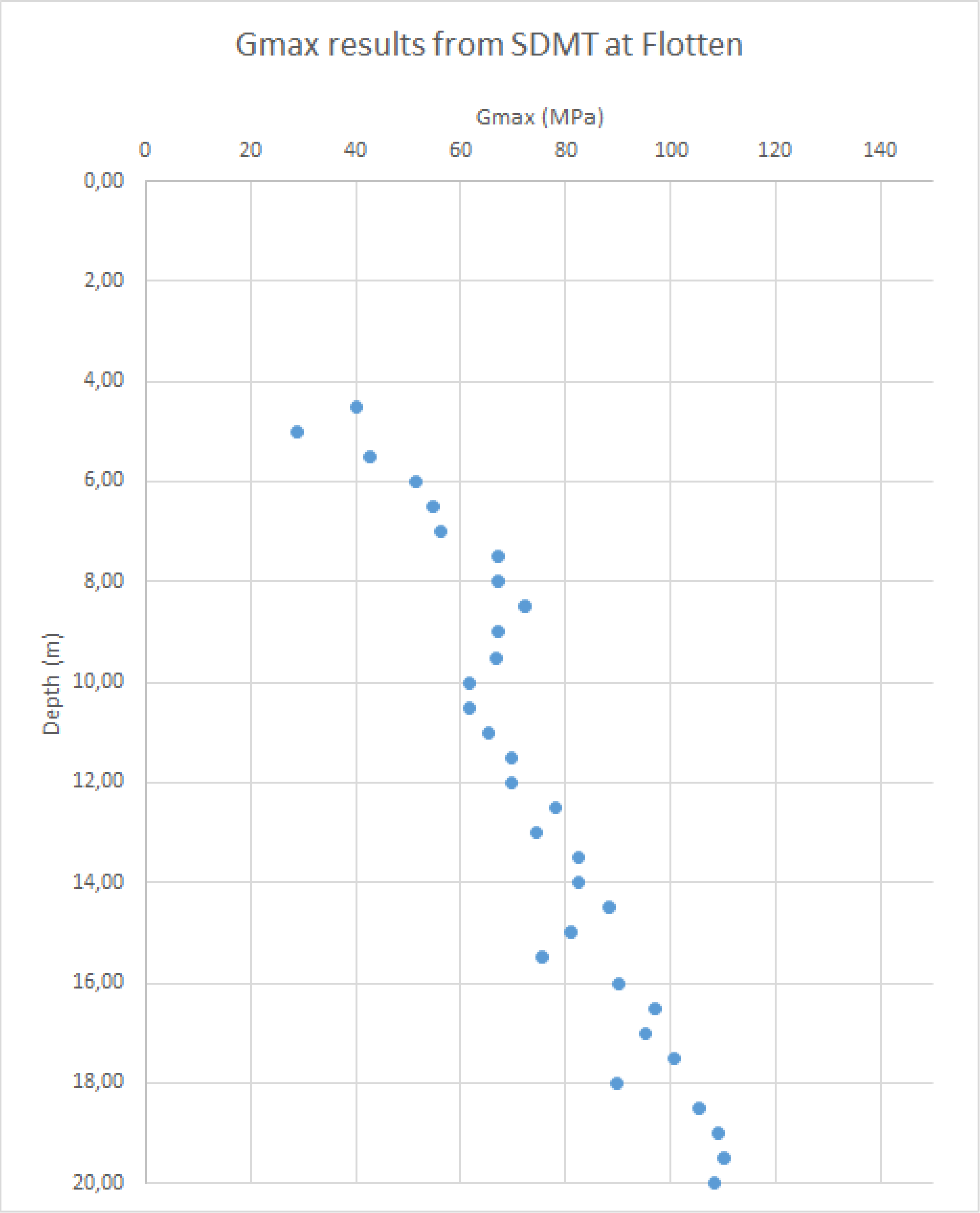

Figure D.2: G_{max} from SDMT plotted against depth for the Flotten test site. (NGU, 2017)